JOURNAL OF PETROLOGY | VOLUME 46 | NUMBER 6 | PAGES 1155–1201 | 2005 | doi:10.1093/petrology/egi013

Post-Collisional Transition from Subduction- to Intraplate-type Magmatism in the Westernmost Mediterranean: Evidence for Continental-Edge Delamination of Subcontinental Lithosphere

S. DUGGEN[1]*, K. HOERNLE[2], P. VAN DEN BOGAARD[2] AND D. GARBE-SCHÖNBERG[3]

[1]GEOMAR RESEARCH CENTRE FOR MARINE GEOSCIENCES, DEPARTMENT OF VOLCANOLOGY AND PETROLOGY, WISCHHOFSTR. 1–3, 24148 KIEL, GERMANY

[2]IFM–GEOMAR LEIBNIZ INSTITUTE FOR MARINE SCIENCES, DYNAMICS OF THE OCEAN FLOOR, WISCHHOFSTR. 1–3, 24148 KIEL, GERMANY

[3]INSTITUTE FOR GEOSCIENCES, UNIVERSITY OF KIEL, OLSHAUSENSTR. 40, 24118 KIEL, GERMANY

RECEIVED NOVEMBER 12, 2003; ACCEPTED JANUARY 14, 2005
ADVANCE ACCESS PUBLICATION FEBRUARY 25, 2005

Post-collisional magmatism in the southern Iberian and northwestern African continental margins contains important clues for the understanding of a possible causal connection between movements in the Earth's upper mantle, the uplift of continental lithosphere and the origin of circum-Mediterranean igneous activity. Systematic geochemical and geochronological studies (major and trace element, Sr–Nd–Pb-isotope analysis and laser $^{40}Ar/^{39}Ar$-age dating) on igneous rocks provide constraints for understanding the post-collisional history of the southern Iberian and northwestern African continental margins. Two groups of magmatic rocks can be distinguished: (1) an Upper Miocene to Lower Pliocene (8·2–4·8 Ma), Si–K-rich group including high-K (calc-alkaline) and shoshonitic series rocks; (2) an Upper Miocene to Pleistocene (6·3–0·65 Ma), Si-poor, Na-rich group including basanites and alkali basalts to hawaiites and tephrites. Mafic samples from the Si–K-rich group generally show geochemical affinities with volcanic rocks from active subduction zones (e.g. Izu–Bonin and Aeolian island arcs), whereas mafic samples from the Si-poor, Na-rich group are geochemically similar to lavas found in intraplate volcanic settings derived from sub-lithospheric mantle sources (e.g. Canary Islands). The transition from Si-rich (subduction-related) to Si-poor (intraplate-type) magmatism between 6·3 Ma (first alkali basalt) and 4·8 Ma (latest shoshonite) can be observed both on a regional scale and in individual volcanic systems. Si–K-rich and Si-poor igneous rocks from the continental margins of southern Iberia and northwestern Africa are, respectively, proposed to have been derived from metasomatized subcontinental lithosphere and sub-lithospheric mantle that was contaminated with plume material. A three-dimensional geodynamic model for the westernmost Mediterranean is presented in which subduction of oceanic lithosphere is inferred to have caused continental-edge delamination of subcontinental lithosphere associated with upwelling of plume-contaminated sub-lithospheric mantle and lithospheric uplift. This process may operate worldwide in areas where subduction-related and intraplate-type magmatism are spatially and temporally associated.

KEY WORDS: *post-collisional magmatism; Mediterranean-style back-arc basins; subduction; delamination; uplift of marine gateways*

INTRODUCTION

Subduction-related and intraplate-type igneous rocks occur together worldwide (e.g. Mediterranean area, Colorado Plateau and Andes) (Kay & Mahlburg Kay,

*Corresponding author. Present address: Geological Institute, University of Copenhagen, Øster Voldgade 10, 1350 Copenhagen K, Denmark. E-mail: sduggen@geol.ku.dk

1993; Arculus & Gust, 1995; Wilson & Bianchini, 1999). Kilometre-scale continental uplift may occur contemporaneously with the magmatic activity and is thought to reflect lithospheric response to rapid changes in upper mantle geometry (Bird, 1979; Turner *et al.*, 1993; Duggen *et al.*, 2003). Large-scale reorganization of the upper mantle may be related to: (1) roll-back and detachment of subducted oceanic lithosphere (Innocenti *et al.*, 1982; Keller, 1982; Davies & Blanckenburg, 1995; Wilson & Bianchini, 1999; Wortel & Spakman, 2000); (2) detachment or convective thinning of subcontinental lithosphere (Pearce *et al.*, 1990; Platt & England, 1993; Turner *et al.*, 1999; López-Ruiz *et al.*, 2002); or (3) delamination (peeling-off) of subcontinental lithosphere (Bird, 1979; Serri *et al.*, 1993; Docherty & Banda, 1995; Gîrbacea & Frisch, 1998; Duggen *et al.*, 2003). Formation of magmas having a subduction-related geochemical signature can result from: (1) subduction of oceanic lithosphere (Hawkesworth *et al.*, 1993; Pearce & Peate, 1995); (2) melting of metasomatically enriched subcontinental lithosphere with an inherited subduction signature (Turner *et al.*, 1996; Benito *et al.*, 1999); or (3) extensive crustal contamination of MORB-like (mid-ocean-ridge basalt) magmas (Turner *et al.*, 1999). Generation of intraplate-type lavas in continental settings is generally related to upwelling sub-lithospheric mantle material (e.g. Western and Central Europe) (Wilson & Downes, 1991; Granet *et al.*, 1995; Hoernle *et al.*, 1995). However, the processes responsible for uplift and the generation of volcanic areas with geochemically diverse rock types such as subduction-related and intraplate-type igneous rocks are still poorly understood.

Combination of systematic geochemical and geochronological data allows reconstruction of the temporal and spatial transition from post-collisional subduction-related to intraplate-type magmatism in the western Mediterranean. The transition occurs regionally in the westernmost Mediterranean realm and locally in individual volcanic systems such as the Gourougou and Guilliz stratovolcanic complexes in northwestern Africa. The new geochemical and geochronological data for igneous rocks from the continental margins of southern Spain and northern Morocco are integrated with published data for rocks from the westernmost Mediterranean sea floor (Duggen *et al.*, 2004) and northwestern Algeria (Louni-Hacini *et al.*, 1995; Coulon *et al.*, 2002) providing the basis for a case study of this transition.

REGIONAL GEOLOGY

Neogene post-collisional igneous rocks occur along the European and African margins of the western Mediterranean (Wilson & Bianchini, 1999). In the Alboran region in the westernmost Mediterranean, Middle Miocene to Pleistocene volcanic rocks can be found in two lithospheric domains: (1) the Alboran Basin (hosting the Alboran Sea), which consists of strongly thinned continental crust progressing into Miocene oceanic crust to the east (Lonergan & White, 1997); (2) the southern Iberian and northwestern African continental margins (Fig. 1).

The Alboran Basin area includes Middle to Late Miocene igneous rocks from the Alboran Sea floor (ridges and seamounts), the Alboran Island and coastal stratovolcanic complexes bordered by major strike-slip faults in southern Spain (the Cabo de Gata and Aguilas block) and northern Morocco (Ras Tarf and Trois Furches) (Duggen *et al.*, 2004) (Fig. 1). The magmatic evolution of the Alboran Basin area is marked by the eruption of magmas of both the low-K (tholeiitic) series and the medium- to high-K (calc-alkaline) series in the Middle to Late Miocene (Figs 1 and 2). The mafic Alboran Basin lavas have major and trace element and O–Sr–Nd–Pb-isotope compositions characteristic of tholeiitic volcanic front and calc-alkaline rear-arc lavas in active subduction zones such as the Izu–Bonin island arc (Benito *et al.*, 1999; Hoernle *et al.*, 1999; Duggen *et al.*, 2004).

The Iberian and African continental areas surrounding the Alboran Basin are marked by igneous activity with a different geochemical composition. Upper Miocene to Pleistocene post-collisional magmatism along the southern Iberian and northwestern African continental margins is characterized by Si-rich, K-rich igneous rocks and Si-poor, Na-rich lavas (Fig. 1). Upper Miocene to Lower Pliocene Si–K-rich igneous rocks include latites, shoshonites and ultrapotassic rocks such as lamproites (Fig. 2) (Bellon & Brousse, 1977; López Ruiz & Rodríguez Badiola, 1980; Venturelli *et al.*, 1984; Hernandez, 1986; Louni-Hacini *et al.*, 1995; El Bakkali *et al.*, 1998; Benito *et al.*, 1999; Coulon *et al.*, 2002). These Si–K-rich igneous rocks are often spatially associated with Si-poor, Na-rich lavas such as alkali basalts and basanites to hawaiites and tephrites. The first Si-poor, Na-rich alkali basalts appeared in the Upper Miocene and continued to erupt into the Quaternary (Figs 1 and 2) (Duggen *et al.*, 2003). The post-collisional transition from Si–K-rich to Si-poor, Na-rich magmatism occurred close to the Miocene–Pliocene boundary that is defined by the Messinian Salinity Crisis and can clearly be seen in the field in the Guilliz volcanic area, where dark alkali basalt lava flows were erupted on top of light-coloured, Si–K-rich, pyroclastic deposits of an eroded stratovolcanic complex.

A large number of models have been proposed to explain the geodynamic evolution of the Alboran region in the westernmost Mediterranean since the Eocene and can be divided into three groups: (1) mantle diapirism (Weijermars, 1985); (2) subduction of oceanic lithosphere involving slab roll-back and slab detachment (Royden, 1993; Zeck, 1996; Lonergan & White, 1997; Hoernle *et al.*, 1999; Coulon *et al.*, 2002; Gutscher *et al.*, 2002; Duggen *et al.*, 2003, 2004); (3) convective removal

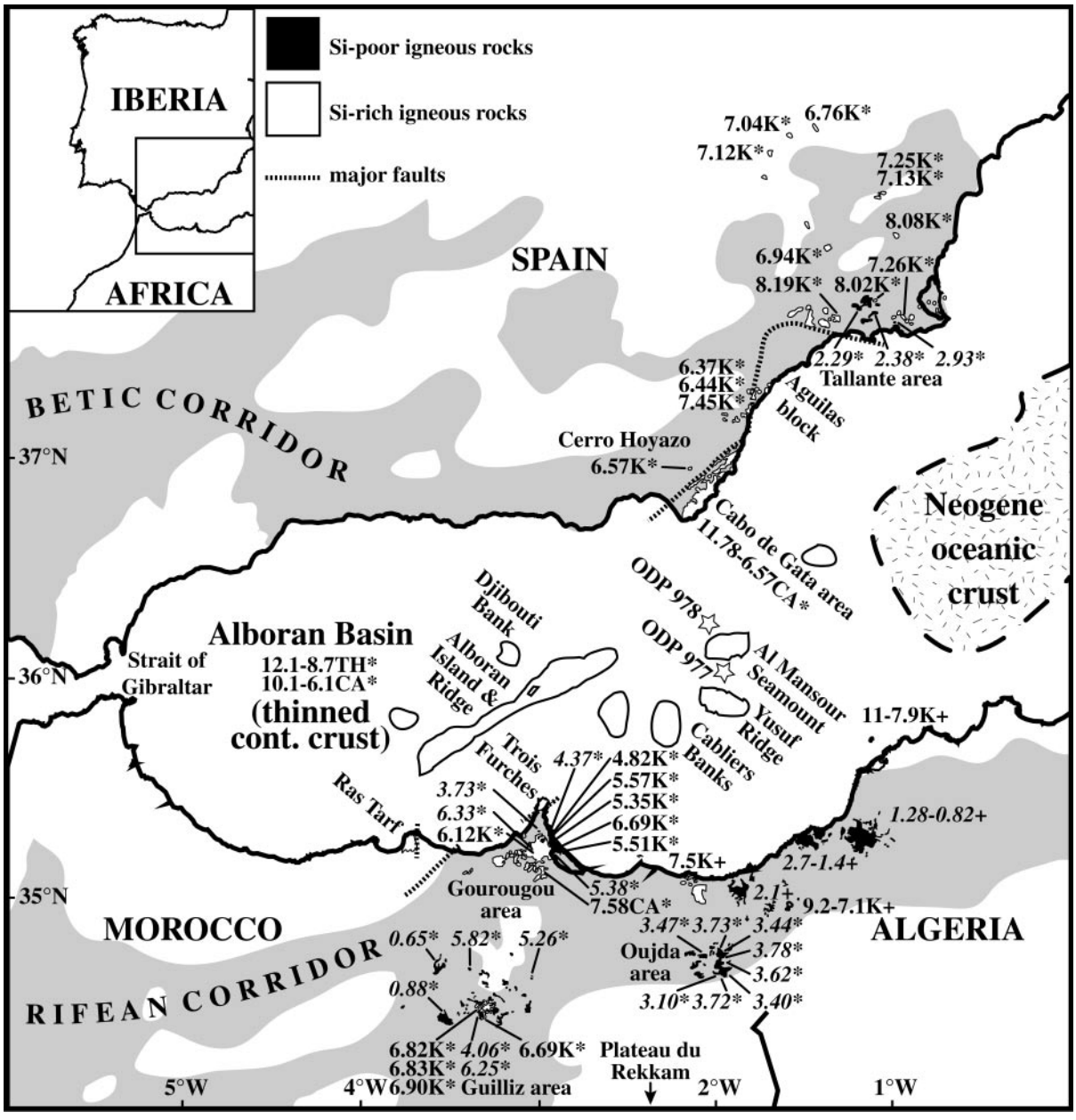

Fig. 1. Map of the westernmost Mediterranean showing the location of Middle Miocene to Pleistocene post-collisional igneous rocks in the Alboran Basin and the continental margins of southern Iberia and northwestern Africa. Grey areas in southern Iberia and northwestern Africa show the location of Late Miocene marine gateways (Betic and Rif Corridors) (Esteban *et al.*, 1996). $^{40}Ar/^{39}Ar$ ages (Spain and Morocco, marked with *) and K/Ar ages (Algeria, marked with +) are in million years (Ma). Si-rich and Si-poor igneous rocks are as defined in Fig. 3. TH, tholeiitic series; CA, calc-alkaline series; K, K-rich series igneous rocks (Si-rich). Si-poor volcanic rocks are shown in italics. Data sources: volcanic rocks in the Alboran Basin area including Ocean Drilling Program (ODP) Holes 977 and 978 (stars) from Hoernle *et al.* (1999, 2003), Duggen *et al.* (2004) and Gill *et al.* (2004); $^{40}Ar/^{39}Ar$ ages from Hoernle *et al.* (1999) and Duggen *et al.* (2004); K/Ar ages for Algerian igneous rocks from Louni-Hacini *et al.* (1995) and Coulon *et al.* (2002); major faults from Coppier *et al.* (1989), Ait-Brahim & Chotin (1990) and Montenat & Ott D'Estevou (1995).

(detachment) and peeling-off (delamination) of subcontinental lithosphere (Platt & Vissers, 1989; Docherty & Banda, 1995; Houseman, 1996; Seber *et al.*, 1996*a*; Comas *et al.*, 1999; Turner *et al.*, 1999; López-Ruiz *et al.*, 2002; Platt *et al.*, 2003). In this study, the temporal and spatial geochemical evolution of the magmatism in the westernmost Mediterranean is integrated with geophysical and geological data from the literature to distinguish between these models. We developed a three-dimensional model that describes the mantle geodynamic setting in the westernmost Mediterranean area near the Miocene–Pliocene boundary.

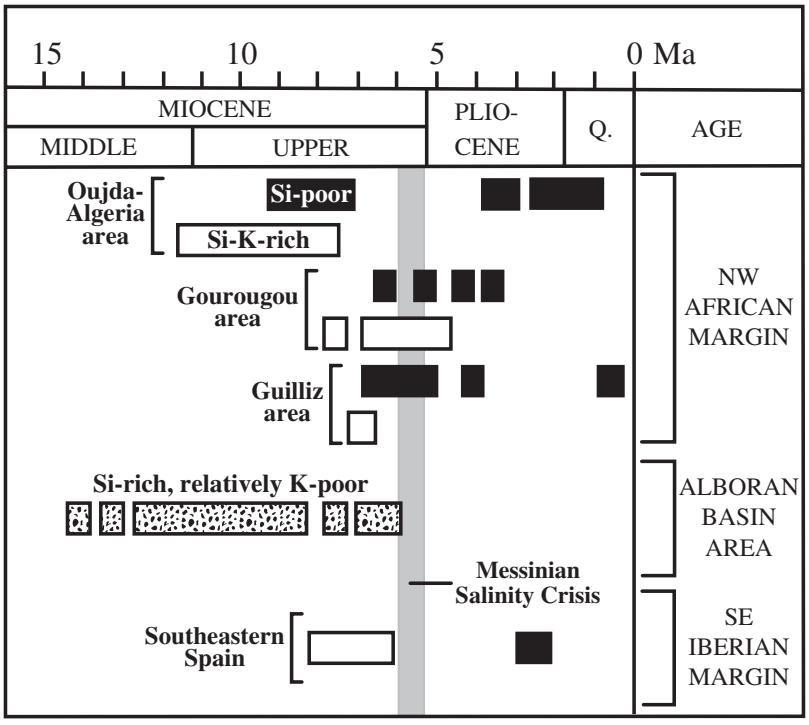

Fig. 2. Chronological evolution of the westernmost Mediterranean post-collisional igneous activity based on laser probe $^{40}Ar/^{39}Ar$ age data for amphibole, biotite and feldspar phenocrysts as well as matrix and glass particles from about 80 samples from the Alboran Sea and the southeastern Iberian (Spain) and northwestern African (Morocco) continental margins (Hoernle *et al.*, 1999; Turner *et al.*, 1999; Duggen *et al.*, 2004). K/Ar geochronological data for post-collisional igneous rocks from northwestern Algeria are also included (Louni-Hacini *et al.*, 1995; Coulon *et al.*, 2002). Si–K-rich and Si-poor igneous rocks from the southeastern Iberian and northwestern African continental margins and Si-rich but relatively K-poor Alboran Sea volcanic rocks (dotted) as defined in Fig. 3. Alboran Basin volcanic rocks include tholeiitic and calc-alkaline submarine lavas from the present Alboran Sea (e.g. Alboran Ridge, Al Mansour Seamount, Yusuf Ridge and volcanic pebbles from ODP holes 977 and 978), the Alboran Island and several coastal areas such as the Aguilas block and Cabo de Gata in Spain and Ras Tarf and Trois Furches in Morocco. The Messinian Salinity Crisis ranges from 5·96 to 5·33 Ma (Krijgsman *et al.*, 1999) and defines the Miocene–Pliocene boundary.

ANALYTICAL METHODS

$^{40}Ar/^{39}Ar$ isotope ratios were measured on K-bearing phases such as amphibole, biotite and feldspar phenocrysts and glass and matrix chips, at the GEOMAR Tephrochronology Laboratory. The freshest possible glass and matrix chips and phenocrysts were hand-picked from crushed and sieved splits and cleaned using an ultrasonic disintegrator. Plagioclase phenocrysts were additionally etched in hydrofluoric acid (15%). For several samples, fresh matrix chips were separated and analysed together with phenocrysts to examine the reliability of age data measured for matrix chips from aphyric igneous rocks. The samples were neutron-irradiated at the 5 MW reactor of the GKSS Reactor Centre in Geesthacht (Federal Republic of Germany), with crystals and glass and matrix chips in aluminium trays and irradiation cans wrapped in 0·7 mm cadmium foil. Age determinations by laser $^{40}Ar/^{39}Ar$ analysis were performed by fusing single crystals and glass and matrix chips in a single step or by laser-step heating analysis when necessary. Purified gas samples were then analysed using a MAP 216 series noble gas mass spectrometer. Raw mass spectrometer peaks were corrected for mass discriminations background, and blank values determined every fifth analysis. Neutron flux during irradiation was monitored using TCR sanidine (Taylor Creek Rhyolite, 27·92 Ma) (Dalrymple & Duffield, 1988; Duffield & Dalrymple, 1990) and an internal standard SAN6165 (0·470 Ma) (van den Bogaard, 1995). Vertical variations in J values were quantified by a cosine function fit. Lateral variations in J were not detected. Optical grade CaF_2 and high-purity K_2SO_4 salt crystals that were irradiated and analysed together with the samples were used for corrections of interfering neutron reactions on Ca and K. For statistical reasons, 3–19 particles of each phase were separately dated to calculate mean apparent ages and isochron ages. For samples that did not produce statistically valid isochron or mean apparent ages, step heating ages on single matrix chips were additionally determined. The age with the highest confidence level was chosen for each sample (Table 1), taking into account mean square weighted deviates (MSWD), plateau portions for step heating analysis, deviation of the

Table 1: Radiometric ages for igneous rocks calculated from $^{40}Ar/^{39}Ar$ compositions of amphibole, biotite, feldspar phenocrysts and matrix chips

Sample	Rock type	Locality	Particle type	No. of particles	MAA (Ma)	MSWD	SHA (Ma)	MSWD	Plateau portion (%)	ICA (Ma)	MSWD	Initial $^{40}Ar/^{36}Ar$
Southern Iberian continental margin												
Southeastern Spanish volcanic field—Si–K-rich group												
LC100599-4	lamproite	La Celia (Jumilla)	mx	7	**6·76 ± 0·04**	1·84				6·77 ± 1·21	2·23	295·3 ± 61·2
CX110599-3	lamproite	Cancarix	fsp	6	7·06 ± 0·02	0·55				7·05 ± 0·05	0·31	424·8 ± 152·6
			amph	12	7·01 ± 0·02	0·89				7·03 ± 0·06	0·94	291·9 ± 5·1
			fsp + amph	18	**7·04 ± 0·01**	0·99				7·06 ± 0·04	0·81	289·3 ± 3·0
LM100599-1a	lamproite	Las Minas	phl	2	**7·12 ± 0·07**							
FT120599-5	lamproite	Fortuna	mx	10	**7·13 ± 0·04**	0·80				6·99 ± 0·20	0·84	297·1 ± 2·2
			phl	14	8·30 ± 0·21	301·20				6·26 ± 1·74	293·60	475·6 ± 145·2
			at cutoff	6	7·25 ± 0·07	3·58						
			mx + phl	24	8·21 ± 0·17	203·10				8·50 ± 0·22	234·80	283·3 ± 8·4
			at cutoff	16	7·20 ± 0·04	2·01						
CT270300-2c	lamproite	Cartagena	phl	11	7·42 ± 0·03	1·44				7·32 ± 0·07	1·29	297·9 ± 1·6
			fsp	13	7·28 ± 0·02	0·72				7·27 ± 0·04	0·77	296·3 ± 2·4
			fsp + phl	24	7·35 ± 0·02	1·77				**7·26 ± 0·03**	1·30	298·5 ± 0·9
FT120599-16A	lamproite	Fortuna	phl	11	7·63 ± 0·09	22·20				7·77 ± 0·11	16·80	283·8 ± 5·2
			at cutoff	5	**7·25 ± 0·06**	3·10						
AL140599-1	lamproite	Aljorra	mx	12	**8·02 ± 0·04**	0·80				7·93 ± 0·17	0·85	296·8 ± 2·4
ZN130599-1	lamproite derivative	Zeneta	phl	11	**8·08 ± 0·03**	1·45				8·09 ± 0·03	1·62	295·3 ± 1·3
MA180599-1	lamproite derivative	Mazarron 3 km NW	phl	12	8·33 ± 0·06	8·90				8·39 ± 0·22	9·79	293·8 ± 6·8
			fsp	10	**8·19 ± 0·02**	1·72				8·19 ± 0·03	1·94	296·1 ± 1·9
			phl + fsp	22	8·25 ± 0·03	6·82				8·19 ± 0·06	6·98	298·3 ± 2·2
BQ170599-9	lamproite	Barqueros	mx	11	**6·94 ± 0·05**	1·07				7·19 ± 0·18	0·96	292·9 ± 1·7
			phl	9	8·55 ± 0·10	27·20				8·77 ± 0·19	26·40	272·1 ± 17·5
			mx + phl	20	8·31 ± 0·15	68·60				8·69 ± 0·09	15·50	278·5 ± 0·5
VE290699-2	lamproite	due W Rio Antas	glass	11	8·42 ± 0·42	14·40				7·04 ± 0·91	12·10	300·1 ± 2·7
			at cutoff	7	**6·44 ± 0·28**	1·70						
VE290699-10A	lamproite derivative	near Cortijo Duarte	phl	12	**7·45 ± 0·08**	2·05				7·25 ± 0·22	2·07	297·2 ± 1·7
VE290699-1	lamproite	due N of Rio Antas	glass	12	**6·37 ± 0·18**	4·32				5·36 ± 0·38	2·58	301·0 ± 1·9

Table 1: continued

Sample	Rock type	Locality	Particle type	No. of particles	MAA (Ma)	MSWD	SHA (Ma)	MSWD	Plateau portion (%)	ICA (Ma)	MSWD	Initial $^{40}Ar/^{36}Ar$
Southeastern Spanish volcanic field (Tallante)—Si-poor group												
TA200400-1	hawaiite	road C. Negro	biot	11	2·28 ± 0·04	5·47				2·43 ± 0·03	1·25	290·7 ± 0·8
			amph	11	2·35 ± 0·05	1·19				2·3 ± 0·2	1·29	305·3 ± 23·5
			biot + amph	22	**2·29 ± 0·03**	3·25				2·37 ± 0·04	2·04	291·6 ± 1·0
LP140599-5	trachybasalt	Los Puertos	gl	11	**2·38 ± 0·06**	1·03				2·3 ± 0·1	1·08	296·3 ± 1·2
CT270300-1a	hawaiite	Cartagena	mx	13	3·08 ± 0·09	1·39				2·2 ± 0·3	0·53	300·0 ± 1·4
			mx				**2·93 ± 0·08**	0·86	95·7			
Northwestern African continental margin (Morocco)												
Gourougou volcanic field—Si-rich, K-rich group												
GG140699-12	trachyandesite	Farkhana	mx	12	5·57 ± 0·05	3·57				**4·8 ± 0·4**	2·51	327·6 ± 14·9
GG280599-9	trachyandesite	Bou Hamza	fsp	11	**6·12 ± 0·01**	0·81				6·13 ± 0·04	0·94	293·8 ± 6·1
GG140699-6	trachyandesite	Izarounalene	biot	14	5·35 ± 0·03	3·19				5·4 ± 0·1	3·46	294·0 ± 4·5
			fsp	10	5·3 ± 0·2	0·64				5·1 ± 0·3	0·53	302·6 ± 5·9
			biot + fsp	24	**5·35 ± 0·02**	2·05				5·4 ± 0·1	2·17	295·3 ± 3·3
GG290599-1	bas. trachyandesite	Tiraka	mx	13	**5·51 ± 0·03**	0·64				5·6 ± 0·2	0·66	290·4 ± 7·5
GG140699-8	trachyandesite	Izmâniyine	fsp	3	5·3 ± 0·2	0·80				6·0 ± 0·6	0·42	274·2 ± 15·9
			mx	8	5·58 ± 0·03	1·03				6·0 ± 0·3	0·94	280·6 ± 11·0
			fsp + mx	11	**5·57 ± 0·03**	1·15				6·1 ± 0·2	0·75	275·7 ± 8·4
GG140699-4	andesite	Atalayoum	mx	12	**6·69 ± 0·05**	1·25				6·7 ± 0·1	1·38	295·6 ± 1·8
GG030699-1a	diorite	Ouixsane mine	biot	12	**7·58 ± 0·03**	1·66				7·68 ± 0·06	1·00	292·3 ± 1·1
Gourougou volcanic field—Si-poor group												
GG070699-1c	alkali basalt	Haidoun	fsp	10	**3·73 ± 0·09**	1·20				3·7 ± 0·2	1·34	296·6 ± 12·0
GG290599-5	alkali basalt	Izarounalene	mx	11	4·8 ± 0·1	2·35				**4·4 ± 0·1**	0·75	299·4 ± 1·0
			mx	20 steps			5·2 ± 0·2	1·14	91·7			
GG080400-3	alkali basalt	Trara	mx	7	**6·3 ± 0·3**	2·05				6·5 ± 0·6	2·42	294·9 ± 2·1
GG090400-1b	trachybasalt	Beni Enzar	fsp + mx	23	**5·4 ± 0·2**	1·70				5·9 ± 0·6	2·47	293·1 ± 1·9
			mx	20 steps			5·4 ± 0·1	0·87	63·2			
Oujda volcanic field—Si-poor group												
OD260599-12	basanite	Oued Isli	mx	16	**3·10 ± 0·09**	1·78				3·5 ± 0·5	1·79	293·1 ± 2·6
OD260599-1	basalt	Oued Isli	mx	19	**3·40 ± 0·07**	1·30				3·7 ± 0·2	1·05	290·7 ± 2·0
OD020699-2b	alkali basalt	Oued Lakram	mx	15	**3·44 ± 0·05**	1·92				3·3 ± 0·1	1·96	302·4 ± 8·3
OD300599-4	basanite	Koudiat Toulia	mx	16	**3·47 ± 0·06**	2·30				3·7 ± 0·2	2·25	292·3 ± 2·7
OD260599-13	basanite	Semmara	mx	14	**3·62 ± 0·09**	1·04				3·4 ± 0·2	0·85	298·3 ± 1·6

Sample	Rock type	Locality	Particle type	No. of particles	MAA (Ma)	MSWD	SHA (Ma)	MSWD	Plateau portion (%)	ICA (Ma)	MSWD	Initial $^{40}Ar/^{36}Ar$
OD260599-10	basanite	Oued Isli	mx	13	**3·72 ± 0·04**	2·01				3·6 ± 0·1	1·71	300·6 ± 2·9
OD020699-1b	trachyandesite	Jorf Lakhdar	mx	12	**3·73 ± 0·03**	1·51				3·65 ± 0·07	1·41	304·4 ± 6·8
OD190699-1a	basanite	Oujda	mx	16	3·76 ± 0·05	2·61				3·4 ± 0·2	2·33	301·9 ± 3·8
			biot	13	**3·78 ± 0·02**	1·20				3·87 ± 0·05	0·95	291·2 ± 2·1
			mx + biot	29	3·78 ± 0·02	1·93				3·79 ± 0·05	2·00	295·2 ± 1·3
Guilliz volcanic field—Si-rich, K-rich group												
GZ280300-4	trachyte	Jebel Guilliz	biot	13	6·83 ± 0·03	1·05				6·78 ± 0·08	1·10	297·0 ± 2·3
			fsp	4	6·4 ± 0·3	2·65				6·8 ± 0·7	3·53	281·3 ± 27·4
			biot + fsp	17	**6·82 ± 0·03**	1·69				6·7 ± 0·1	2·96	297·8 ± 3·7
GZ280300-1	trachyte	Jebel Guilliz	biot	13	6·77 ± 0·03	1·83				6·7 ± 0·1	1·89	299·2 ± 4·7
			fsp	12	6·88 ± 0·02	0·56				6·88 ± 0·03	0·61	295·0 ± 4·1
			biot + fsp	25	**6·83 ± 0·02**	1·87				6·88 ± 0·03	1·52	291·2 ± 1·6
GZ170699-1a	ash flow tuff	Jebel Guilliz	fsp	11	**6·96 ± 0·01**	1·15				6·95 ± 0·05	1·34	303·7 ± 37·8
GZ280300-3b	trachyte	Jebel Guilliz	biot	13	6·92 ± 0·01	1·10				6·89 ± 0·04	1·07	298·7 ± 2·8
			fsp	8	**6·90 ± 0·09**	0·36				7·0 ± 0·1	0·28	279·5 ± 2·8
			mx	11	6·68 ± 0·03	1·09				6·67 ± 0·07	1·21	295·7 ± 1·3
			biot + fsp + mx	32	6·87 ± 0·02	2·68				6·92 ± 0·03	2·15	291·8 ± 1·0
			mx	20 steps			6·92 ± 0·09	0·73	79·2			
Guilliz volcanic field—Si-poor group												
GZ160699-1	hawaiite	Ain Zora	mx	19	**0·65 ± 0·04**	2·99				0·3 ± 0·1	1·89	310·9 ± 4·8
GZ160699-5	alkali basalt	Jebel El Kehal	mx	8	**0·88 ± 0·04**	2·74				0·9 ± 0·4	3·18	294·7 ± 28·0
GZ170699-4	alkali basalt	Jebel Guilliz	mx	8	**4·06 ± 0·06**	0·90				3·6 ± 0·6	0·88	318·5 ± 24·6
GZ170699-3	alkali basalt	Jebel Guilliz	mx	24	**6·3 ± 0·1**	2·61				7·2 ± 0·3	1·81	289·9 ± 1·6
GZ180699-4	alkali basalt	M. el Rhassoul	fsp	5	5·2 ± 0·3	1·66				6·5 ± 1·2	1·51	263·2 ± 28·2
			mx	5	5·4 ± 0·6	4·26				7·7 ± 0·7	1·10	290·9 ± 1·2
			fsp+mx	10	**5·3 ± 0·3**	2·67				5·6 ± 0·4	2·68	294·4 ± 1·1
GZ150699-1	alkali basalt	J. Tassatfacht	mx	13	**5·8 ± 0·2**	3·95				5·3 ± 0·6	4·04	298·3 ± 3·3

Accepted ages are shown with bold letters. Errors are quoted at the 1σ confidence level. MAA, mean apparent age; SHA, step heating age; ICA, isochron age; MSWD, mean square weighted deviates; amph, amphibole; biot, biotite phenocrysts; fsp, feldspar; phl, phlogopite phenocrysts; gl, glass; mx, matrix chips. Sample locations are given in Table 2 with the exception of VE290699-1 and GZ170699-1a: sample VE290699-1 is a lava flow with pillows that intruded into soft calcareous mud and crops out near the Rio Antas (37°12·85′N, 001°50·35′W). Sample GZ170699-1a is an ash flow tuff from Jebel Guilliz cropping out immediately below the oldest dated alkali basalt lava flow GZ040400-8 and separated by an erosional unconformity.

data in the isochron plots (see Electronic Appendix 1, which may be downloaded from http://www.petrology.oupjournals.org) and the initial $^{40}Ar/^{39}Ar$ ratio. Errors on the age data are reported at the 1σ confidence level.

For bulk-rock geochemical analyses, whole-rock sample chips (0·1–1 cm in diameter) were hand-picked using a binocular to minimize the effects of alteration; these were then cleaned ultrasonically with de-ionized water to extract salts, and then dried and pulverized in an agate mill. Bulk-rock analyses of major and selected trace elements (Ba, Co, Cr, Cu, Ga, Rb, Sr, V and Zr) were performed on fused tablets with a Philips X'unique PW 1480 X-ray fluorescence spectrometer (XRF) at the GEOMAR Research Centre. International reference standards JB-2, JB-3 (basalts), JA-2, JA-3 (andesites), JR-2, JR-3 (rhyolites), JG-2, GM (granites) and JF-1 (feldspar) were used to evaluate the precision and accuracy of the measurements. Na contents were normalized to the standard values to account for X-ray tube drift for this element. H_2O and CO_2 were determined using a Rosemont Infrared Photometer CSA 5003. The new data are presented in Table 2 and Electronic Appendix 2. Values of major elements given in the text and used for plotting and rock classification were calculated on a volatile-free basis following a correction of Ca contents assuming that CO_2 comes from $CaCO_3$.

Additional trace elements (Li, Y, Nb, Mo, Sn, Sb, Cs, REE, Hf, Ta, W, Tl, Pb, Th and U) were determined from mixed acid (HF–aqua regia–$HClO_4$) pressure digests by inductively coupled plasma-mass spectrometry (ICP-MS) at the Institute for Geoscience, University of Kiel, using an upgraded (High-Performance Interface, torch box) VG Plasmaquad PQ1. The precision of analytical results as estimated from duplicate measurements was better than 3% RSD. Details of the analytical procedure have been described in the literature (Garbe-Schönberg, 1993). Blanks and international standards, BE-N and BHVO-1, were analysed with the samples, to evaluate the precision and accuracy of the measurements (Duggen, 2002). The ICP-MS trace element data are presented in Table 2 and Electronic Appendix 2.

Sr, Nd and Pb isotopic analyses were carried out on whole-rock powders. To minimize the effects of seawater alteration, the powders were leached with hot distilled 6 M HCl for 1 h (except the highly evolved samples). After dissolution with Merck Ultrapur HF, HNO_3 and HCl, Sr, Nd and Pb were extracted by conventional ion exchange chromatographic techniques. Isotope ratios of all samples were measured by thermal ionization mass spectrometry (TIMS) in static (Sr, Nd, Pb) and dynamic (Sr, Nd) mode on a Finnigan MAT262 system at GEOMAR. Measured $^{87}Sr/^{86}Sr$ and $^{143}Nd/^{144}Nd$ ratios were normalized within-run to $^{86}Sr/^{88}Sr = 0{\cdot}1194$ and $^{146}Nd/^{144}Nd = 0{\cdot}7219$. The Sr and Nd isotope ratios were further normalized to $^{87}Sr/^{86}Sr = 0{\cdot}71025$ (NBS 987 standard) and $^{143}Nd/^{144}Nd = 0{\cdot}51185$ (La Jolla standard) or $^{143}Nd/^{144}Nd = 0{\cdot}51171$ (internal Nd-Spex standard calibrated to La Jolla) to correct for mass spectrometer drift. Replicate analyses of standards NBS 987 (Sr), La Jolla and Nd-Spex (Nd) used for the evaluation of the external precision gave mean values of $^{87}Sr/^{86}Sr = 0{\cdot}710242 \pm 0{\cdot}000017$ (2 SD) ($n = 39$), $^{143}Nd/^{144}Nd = 0{\cdot}511841 \pm 0{\cdot}0000010$ (2 SD) ($n = 13$) and $^{143}Nd/^{144}Nd = 0{\cdot}511706 \pm 0{\cdot}000008$ (2 SD) ($n = 12$). Replicate analyses of the NBS 981 (Pb) standard yielded a mean value of $^{206}Pb/^{204}Pb = 16{\cdot}894 \pm 0{\cdot}004$ (2 SD), $^{207}Pb/^{204}Pb = 15{\cdot}433 \pm 0{\cdot}005$ (2 SD) and $^{208}Pb/^{204}Pb = 36{\cdot}515 \pm 0{\cdot}017$ (2 SD.) ($n = 23$). Pb-isotope data were corrected for 0·1238‰ mass discrimination per atomic mass unit (a.m.u.). Total analytical blanks were on average $<0{\cdot}100$ ng and are thus negligible given the generally high Pb content of the samples.

RESULTS

$^{40}Ar/^{39}Ar$ geochronological data

Laser probe $^{40}Ar/^{39}Ar$ age data for 45 volcanic rocks from the Iberian and African continental margins in southeastern Spain and northern Morocco are reported in Table 1. Phenocryst ages are identical within error, or in very good agreement with each other, in all samples (e.g. feldspar and amphibole in sample CX110599-3, biotite and amphibole in sample TA200400-1, biotite and feldspar in GZ280300-1). Matrix chip ages are also identical within error and in accordance with the phenocryst ages (e.g. matrix and feldspar in GG140699-8, matrix and feldspar and biotite in GZ280300-3b, matrix and feldspar in GZ180699-4, matrix and biotite in OD190699-1a), showing that analyses of carefully prepared matrix chips can provide reliable age data. Two Si–K-rich samples (lamproites) from southeastern Spain yielded phlogopite ages (FT120599-5, BQ170599-9) with high MSWD values as a result of a large variation in single phenocryst ages. These phlogopite ages are significantly older than the matrix ages and are unlikely to reflect eruption ages. Three other Si–K-rich (lamproite) samples (CT270300-2c, ZN130599-1, VE290699-10A) provided phlogopite ages having low MSWD and initial $^{40}Ar/^{36}Ar$ ratios close to the atmospheric value and are thus considered to represent eruption ages. Below we systematically discuss the laser probe $^{40}Ar/^{39}Ar$ age data for the Si–K-rich igneous rocks followed by the Si-poor lavas from four areas on the Iberian and African continental margins: southeastern Spain and the Gourougou, Guilliz and Oujda volcanic areas in northwestern Africa (Fig. 1).

The southern Iberian continental margin

Laser probe $^{40}Ar/^{39}Ar$ age data for 13 Si–K-rich rocks (lamproites and their derivatives) from southeastern Spain

Table 2: Major, minor and trace element analyses of igneous rocks from the southern Iberian and northwestern African continental margins

	Southeastern Spain—Si–K-rich group							
Locality:	Murcia area Calasparra	Murcia area Cancarix	Murcia area La Celia	Murcia area Las Minas	Vera basin W of Rio Antas near highway	Murcia area Barqueros	Murcia area Fortuna	Murcia area Aljorra
Latitude N:	38°14·62′		38°28·00′	38°19·89′	37°12·08′	37°57·51′	38°09·51′	37°41·59′
Longitude W:	1°43·00′		1°28·17′	1°42·00′	1°54·00′	1°21·96′	1°05·61′	1°05·87′
Sample:	CAL090599-1 column from plug	CX110599-3 massive rock	LC100599-4 column from flow	LM160300-1 peripheral intrusion	VE290699-2 lava flow	BQ170599-9 dyke chilled margin	FT120599-5 intrusion	AL260300-1 lava flow
Rock type:	lamproite	lamproite	lamproite	lamproite	lamproite	lamproite	lamproite	lamproite
Major elements (wt %)								
SiO_2	55·1	55·7	49·9	56·5	54·9	57·6	55·7	55·6
TiO_2	1·66	1·54	1·48	1·64	1·41	1·46	1·41	1·02
Al_2O_3	9·37	9·23	9·77	9·63	11·1	11·1	11·6	12·2
FeO^T	4·69	4·80	5·43	4·63	4·66	5·27	4·94	5·14
MnO	0·07	0·08	0·10	0·08	0·07	0·08	0·06	0·09
MgO	12·4	12·1	11·9	10·1	10·1	9·54	9·13	8·30
CaO	2·64	3·42	6·16	2·75	2·87	3·24	2·94	6·32
Na_2O	0·42	0·78	0·92	1·51	2·80	1·01	0·93	1·15
K_2O	9·86	9·11	5·33	9·14	3·69	7·75	7·88	6·48
P_2O_5	1·09	1·14	1·60	1·07	0·73	0·89	0·90	0·85
H_2O	1·14	0·25	3·96	0·58	4·21	1·19	2·29	0·63
CO_2	0·03	0·01	0·85	0·03	1·88	0·11	0·09	0·82
Total	98·5	98·1	97·4	97·7	98·3	99·2	97·9	98·6
Trace elements (ppm)								
Li*	20·5	19·9	27·2	38·9	36·9	18·0	22·1	18·4
V	91·0	77·0	108	83·0	97·0	96·0	102	118
Cr	1225	1039	1170	1021	987	743	778	793
Co	6·00	7·00	22·0	6·00	19·0	8·00	9·00	13·0
Ni	102	151	340	218	210	103	145	151
Zn	85·0	83·0	98·0	71·0	79·0	87·0	125	56·0
Ga	19·0	16·0	14·0	20·0	21·0	22·0	19·0	17·0
Rb	785	676	253	651	535	667	698	360
Sr	549	864	1375	712	443	540	506	590
Y*†	19·3	22·9	25·8	28·8	18·7	22·2	22·7	19·4
Zr	814	768	628	943	575	718	647	428
Nb*†	38·0	40·8	36·4	35·3	33·6	40·8	34·0	28·5
Mo*				0·10				
Sn*	16·9	15·7	15·1	13·7	15·3	13·0	10·9	8·83
Sb*				0·08				
Cs*	48·8	20·1	49·6	10·5	46·8	29·7	13·2	21·6
Ba	1865	1694	3216	1893	1516	1647	1843	2101
La*†	90·6	109	101	128	93·6	100	72·2	77·7
Ce*†	258	293	263	285	250	265	192	195
Pr*	38·0	42·4	37·3	38·1	35·2	36·9	27·3	27·3
Nd*	168	186	163	164	149	157	120	120

Table 2: continued

	Southeastern Spain—Si–K-rich group							
Locality:	Murcia area Calasparra	Murcia area Cancarix	Murcia area La Celia	Murcia area Las Minas	Vera basin W of Rio Antas near highway	Murcia area Barqueros	Murcia area Fortuna	Murcia area Aljorra
Latitude N:	38°14·62′		38°28·00′	38°19·89′	37°12·08′	37°57·51′	38°09·51′	37°41·59′
Longitude W:	1°43·00′		1°28·17′	1°42·00′	1°54·00′	1°21·96′	1°05·61′	1°05·87′
Sample:	CAL090599-1 column from plug	CX110599-3 massive rock	LC100599-4 column from flow	LM160300-1 peripheral intrusion	VE290699-2 lava flow	BQ170599-9 dyke chilled margin	FT120599-5 intrusion	AL260300-1 lava flow
Rock type:	lamproite	lamproite	lamproite	lamproite	lamproite	lamproite	lamproite	lamproite
Sm*	32·0	34·5	31·1	32·0	27·0	28·9	23·7	22·4
Eu*	4·89	5·29	4·98	4·92	4·12	4·25	3·73	3·49
Gd*	16·9	18·1	17·9	16·48	14·3	15·5	13·6	12·43
Tb*	1·64	1·79	1·86	1·71	1·41	1·60	1·49	1·34
Dy*	5·92	6·73	7·37	6·48	5·32	6·17	6·22	5·40
Ho*	0·87	1·04	1·14	0·97	0·82	0·98	1·01	0·85
Er*	2·10	2·56	2·74	2·41	2·02	2·49	2·50	2·06
Tm*	0·25	0·31	0·34	0·29	0·25	0·32	0·33	0·26
Yb*	1·57	2·03	2·10	1·79	1·65	2·06	2·11	1·68
Lu*	0·21	0·28	0·29	0·25	0·23	0·29	0·30	0·23
Hf*	24·7	23·8	20·6	19·9	19·2	22·0	18·2	12·9
Ta*	2·82	2·95	2·60	2·09	2·52	2·92	2·40	2·15
W*	12·2	6·70	1·99		11·0	13·2	9·47	14·5
Tl*	1·24	0·95	2·38	2·06	4·35	2·66	4·53	2·41
Pb*†	67·4	117	116	117	58·5	67·6	105	84·0
Th*†	110	128	114	120	90·3	108	81·1	106
U*	27·5	24·0	15·3	32·2	20·7	28·2	21·9	20·7

	Southeastern Spain—Si–K-rich group			Southeastern Spain—Si-poor group			
Locality:	Murcia area Fortuna	Murcia area Zeneta	Vera basin road cutting hill at Cortijo Duarte	Cartagena & Tallante area Cabezo Negro	Cartagena & Tallante area Pico Cebolla	Cartagena & Tallante area Los Pérez	Cartagena & Tallante area Los Puertos
Latitude N:	38°10·81′	37°59·70′	37°18·25′	37°39·54′	37°39·73′	37°39·59′	37°39·15′
Longitude W:	1°05·08′	0°57·82′	1°47·80′	01°09·00′	01°10·13′	01°07·54′	01°07·61′
Sample:	FT120599-16A dyke chilled margin	ZN130599-1 intrusion in pyrocl. breccia	VE290699-10A deformed dyke	TA 260300-6a lava flow	TA 260300-7 scoria cone	LP170300-1 massif centre central vent?	LP140599-5 lava flow base breccia
Rock type:	lamproite	lamproite derivative	lamproite derivative	trachybasalt	hawaiite	hawaiite	trachybasalt
Major elements (wt %)							
SiO_2	57·0	62·7	63·7	46·5	45·3	44·5	48·6
TiO_2	1·53	0·81	0·75	2·67	2·82	2·65	2·12
Al_2O_3	12·6	13·7	13·6	15·0	14·8	15·1	17·5
FeO^T	4·54	3·13	5·04	9·39	9·53	9·84	8·03
MnO	0·07	0·04	0·09	0·15	0·15	0·17	0·14

	Southeastern Spain—Si–K-rich group			Southeastern Spain—Si-poor group			
Locality:	Murcia area Fortuna	Murcia area Zeneta	Vera basin road cutting hill at Cortijo Duarte	Cartagena & Tallante area Cabezo Negro	Cartagena & Tallante area Pico Cebolla	Cartagena & Tallante area Los Pérez	Cartagena & Tallante area Los Puertos
Latitude N:	38°10·81′	37°59·70′	37°18·25′	37°39·54′	37°39·73′	37°39·59′	37°39·15′
Longitude W:	1°05·08′	0°57·82′	1°47·80′	01°09·00′	01°10·13′	01°07·54′	01°07·61′
Sample:	FT120599-16A dyke chilled margin	ZN130599-1 intrusion in pyrocl. breccia	VE290699-10A deformed dyke	TA 260300-6a lava flow	TA 260300-7 scoria cone	LP170300-1 massif centre central vent?	LP140599-5 lava flow base breccia
Rock type:	lamproite	lamproite derivative	lamproite derivative	trachybasalt	hawaiite	hawaiite	trachybasalt
MgO	5·43	2·51	1·47	8·22	7·50	7·32	5·37
CaO	3·34	3·01	2·99	9·06	10·2	10·3	8·01
Na_2O	2·26	1·74	1·61	3·25	4·14	4·27	3·46
K_2O	6·01	7·25	5·77	2·25	1·33	1·04	2·94
P_2O_5	1·07	0·86	0·76	0·80	0·88	0·78	0·82
H_2O	3·82	0·87	1·01	1·40	2·36	2·53	1·43
CO_2	0·25	1·28	0·02	0·26	0·20	0·14	0·12
Total	98·0	97·9	96·8	98·9	99·3	98·7	98·5
Trace elements (ppm)							
Li*	28·0	39·9	22·9				
V	110	86·0	114	218	256	253	190
Cr	762	395	179	303	245	235	165
Co	10·0	4·00	8·00	37·0	40·0	44·0	28·0
Ni	46·0	48·0	44·0	139	106	115	82·0
Zn	96·0	64·0	413	91·0	93·0	98·0	88·0
Ga	25·0	26·0	18·0	18·0	19·0	18·0	21·0
Rb	540	388	271	68·0	52·0	68·0	120
Sr	483	523	567	817	977	862	887
Y*†	21·6	17·6	21·8	19·6*	18·0*	20·5*	18·7*
Zr	695	356	265	252	274	274	331
Nb*†	30·8	17·4	22·2	63·8	77·4	75·7	88·6
Mo*							
Sn*	10·9	6·1	7·48				
Sb*							
Cs*	31·2	17·3	37·0	2·13	1·51	2·42	2·99
Ba	1527	1966	1969	739	897	899	996
La*†	75·1	59·4	118	50·5	54·4	52·7	67·3
Ce*†	212	143	245	98·4	106	100	124
Pr*	31·3	19·3	28·4	11·2	12·0	11·3	13·2
Nd*	141	84·2	108	42·7	46·3	43·2	47·4
Sm*	27·6	17·3	19·0	8·23	8·74	8·38	8·07
Eu*	4·19	2·97	2·54	2·47	2·55	2·55	2·35
Gd*	14·9	10·5	11·9	7·27	7·54	7·40	6·91
Tb*	1·54	1·17	1·33	0·93	0·95	0·96	0·86
Dy*	6·13	4·86	5·69	4·80	4·86	4·99	4·48
Ho*	0·97	0·76	0·93	0·83	0·82	0·87	0·80
Er*	2·41	1·79	2·26	2·10	2·06	2·18	2·09
Tm*	0·31	0·23	0·29	0·27	0·26	0·28	0·28

Table 2: continued

	Southeastern Spain—Si–K-rich group			Southeastern Spain—Si-poor group			
Locality:	Murcia area Fortuna	Murcia area Zeneta	Vera basin road cutting hill at Cortijo Duarte	Cartagena & Tallante area Cabezo Negro	Cartagena & Tallante area Pico Cebolla	Cartagena & Tallante area Los Pérez	Cartagena & Tallante area Los Puertos
Latitude N:	38°10·81′	37°59·70′	37°18·25′	37°39·54′	37°39·73′	37°39·59′	37°39·15′
Longitude W:	1°05·08′	0°57·82′	1°47·80′	01°09·00′	01°10·13′	01°07·54′	01°07·61′
Sample:	FT120599-16A dyke chilled margin	ZN130599-1 intrusion in pyrocl. breccia	VE290699-10A deformed dyke	TA 260300-6a lava flow	TA 260300-7 scoria cone	LP170300-1 massif centre central vent?	LP140599-5 lava flow base breccia
Rock type:	lamproite	lamproite derivative	lamproite derivative	trachybasalt	hawaiite	hawaiite	trachybasalt
Yb*	2·00	1·48	1·82	1·62	1·56	1·72	1·76
Lu*	0·28	0·20	0·24	0·22	0·21	0·23	0·24
Hf*	20·6	8·95	6·11	5·47	5·73	5·66	6·47
Ta*	2·12	1·08	1·82	3·73	4·52	4·47	5·31
W*	5·76	10·0	12·9				
Tl*	3·30	3·98	7·41				
Pb*†	50·2	96·7	118	8·61	9·43	7·13	12·8
Th*†	109	68·4	90·0	15·3	13·5	13·1	24·7
U*	25·5	16·5	21·8	3·37	3·82	2·83	5·68

	Southeastern Spain—Si-poor group				Gourougou volcanic field—Si–K-rich group		
Locality:	Cartagena & Tallante area Los Puertos	Cartagena & Tallante area Cartagena	Cartagena & Tallante area road C. Negro	Cartagena & Tallante area Los Pérez	Tiraka	Farkhana	Atalayoum
Latitude N:	37°39·15′	37°36·76′	37°36·27′	37°40·31′	35°12·22′	35°16·92′	35°12·89′
Longitude W:	01°07·61′	00°57·40′	01°07·80′	01°08·22′	02°55·53′	02°58·39′	02°55·53′
Sample:	LP140599-5 lava flow base breccia	CT270300-1a dyke in phreato-magm. deposit	TA 200400-1 lava flow in scoria cone	TA 260300-4 lava flow	GG290599-1 upper lava flow in little quarry	GG140699-12 lava flow	GG140699-4 huge columnar boulder
Rock type:	trachybasalt	trachybasalt	hawaiite	phonotephrite	basaltic trachyandesite	basaltic trachyandesite	basaltic andesite
Major elements (wt %)							
SiO_2	48·5	47·0	47·3	48·6	51·8	53·8	55·4
TiO_2	2·11	2·41	2·34	2·06	1·15	1·04	0·95
Al_2O_3	17·5	16·7	17·2	17·8	16·4	17·4	16·7
FeO^T	7·92	8·96	8·53	7·99	7·23	7·32	7·38
MnO	0·14	0·16	0·15	0·16	0·14	0·13	0·13
MgO	5·35	5·25	4·78	4·17	5·23	4·43	3·92
CaO	8·00	8·80	8·60	7·56	9·47	8·67	8·06
Na_2O	3·49	3·86	5·24	6·46	2·66	2·89	2·39
K_2O	2·94	2·84	1·93	1·65	2·69	2·91	2·79
P_2O_5	0·85	0·84	0·88	0·96	0·39	0·39	0·39
H_2O	1·43	2·16	1·92	1·59	1·38	0·49	0·56
CO_2	0·12	0·12	0·02	0·03	0·26	0·02	0·09
Total	98·4	99·1	98·9	98·9	98·8	99·6	98·8

	Southeastern Spain—Si-poor group				Gourougou volcanic field—Si–K-rich group		
Locality:	Cartagena & Tallante area Los Puertos	Cartagena & Tallante area Cartagena	Cartagena & Tallante area road C. Negro	Cartagena & Tallante area Los Pérez	Tiraka	Farkhana	Atalayoum
Latitude N:	37°39·15′	37°36·76′	37°36·27′	37°40·31′	35°12·22′	35°16·92′	35°12·89′
Longitude W:	01°07·61′	00°57·40′	01°07·80′	01°08·22′	02°55·53′	02°58·39′	02°55·53′
Sample:	LP140599-5 lava flow base breccia	CT270300-1a dyke in phreato-magm. deposit	TA 200400-1 lava flow in scoria cone	TA 260300-4 lava flow	GG290599-1 upper lava flow in little quarry	GG140699-12 lava flow	GG140699-4 huge columnar boulder
Rock type:	trachybasalt	trachybasalt	hawaiite	phonotephrite	basaltic trachyandesite	basaltic trachyandesite	basaltic andesite
Trace elements (ppm)							
Li*							
V	187	209	212	176	219	210	216
Cr	160	147	187	77·0	144	83·0	28·0
Co	28·0	31·0	32·0	31·0	26·0	23·0	23·0
Ni	85·0	69·0	89·0	59·0	41·0	29·0	12·0
Zn	89·0	99·0	101	98·0	51·0	59·0	64·0
Ga	20·0	22·0	23·0	19·0	12·0	17·0	17·0
Rb	119	101	45·0	42·0	114	120	100
Sr	889	954	1086	1031	646	592	448
Y*†	18·4*	20·7*	18·1*	19·7*	21·1*	20·7*	22·3*
Zr	337	327	319	345	127	139	146
Nb*†	90·8	87·8	93·3	104·5	36·5	33·8	11·8
Mo*							
Sn*							
Sb*							
Cs*	1·86	2·04	1·79	4·34	0·99	2·93	1·82
Ba	966	904	1127	1142	725	809	1561
La*†	68·5	63·1	65·0	82·3	30·8	33·1	26·6
Ce*†	126	118	121	150	58·1	62·4	53·5
Pr*	13·4	12·9	13·1	15·8	6·94	7·42	6·59
Nd*	48·2	47·6	47·9	55·7	26·7	28·1	25·9
Sm*	8·28	8·68	8·42	9·21	5·14	5·43	5·36
Eu*	2·39	2·57	2·56	2·57	1·38	1·42	1·27
Gd*	7·02	7·48	7·23	7·51	4·53	4·48	4·71
Tb*	0·87	0·96	0·90	0·93	0·65	0·65	0·68
Dy*	4·53	5·02	4·62	4·72	3·77	3·67	4·01
Ho*	0·80	0·89	0·80	0·83	0·76	0·73	0·80
Er*	2·10	2·31	2·08	2·18	2·09	2·07	2·25
Tm*	0·28	0·31	0·27	0·29	0·30	0·30	0·33
Yb*	1·77	1·89	1·66	1·81	1·96	1·96	2·16
Lu*	0·24	0·26	0·23	0·25	0·29	0·30	0·32
Hf*	6·70	6·36	6·09	6·88	3·20	3·67	4·01
Ta*	5·47	5·22	5·47	6·45	2·07	1·91	0·70
W*							
Tl*					0·15	0·27	0·12
Pb*†	13·1	10·8	9·60	16·0	3·31	4·32	9·58
Th*†	24·8	19·7	14·3	33·2	9·37	13·6	9·98
U*	5·84	4·56	3·42	7·47	3·25	4·41	3·65

Table 2: continued

	Gourougou volcanic field—Si–K-rich group				Gourougou volcanic field—Si-poor group			
Locality:	Izmâniyine	Izarounalene	Ouixsane mine	Bou Hamza	Haidoun	Izarounalene	Trara	Beni Enzar
Latitude N:	35°16·30′	35°15·70′	35°07·57′	35°12·85′	35°17·89′	35°15·73′	35°13·17′	35°12·50′
Longitude W:	02°58·00′	02°57·10′	03°01·51′	03°06·21′	03°00·63′	02°57·04′	03°02·55′	02°55·47′
Sample:	GG140699-8 lava flow above trachyte	GG140699-6 lava flow	GG030699-1a intrusion	GG 280599-9 lava flow	GG070699-1c lava flow	GG290599-5 huge boulder in quarry	GG080400-3 lava flow	GG090400-1b lava flow coarser centre
Rock type:	basaltic trachyandesite	trachyandesite	diorite	trachyandesite	alkali basalt	alkali basalt	alkali basalt	trachybasalt
Major elements (wt %)								
SiO_2	53·7	58·6	60·4	57·4	46·3	49·1	48·9	48·6
TiO_2	1·06	0·77	0·56	0·79	1·97	1·36	1·25	1·43
Al_2O_3	18·2	16·7	15·4	16·8	16·1	17·0	17·0	18·8
FeO^T	7·17	6·21	4·30	6·33	9·08	7·06	7·93	7·32
MnO	0·13	0·12	0·06	0·09	0·16	0·14	0·15	0·15
MgO	3·53	2·69	2·51	2·35	8·22	8·18	7·17	5·18
CaO	7·97	6·73	4·74	6·04	11·0	9·35	10·6	8·17
Na_2O	3·14	3·03	2·32	2·88	3·23	3·53	3·02	3·66
K_2O	3·06	3·33	4·04	4·67	0·96	1·40	1·54	2·83
P_2O_5	0·45	0·32	0·24	0·38	0·47	0·44	0·35	0·67
H_2O	0·57	0·74	2·28	1·05	1·68	1·02	1·08	2·23
CO_2	0·02	0·03	2·22	0·02	0·06	0·11	0·04	0·10
Total	99·0	99·2	99·1	98·9	99·3	98·8	99·0	99·1
Trace elements (ppm)								
Li*								
V	209	159	114	166	256	206	251	175
Cr	41·0	57·0	35·0	40·0	188	222	188	69·0
Co	22·0	17·0	11·0	15·0	42·0	33·0	36·0	28·0
Ni	27·0	18·0	<2	11·0	125	114	67·0	48·0
Zn	56·0	57·0	51·0	70·0	72·0	59·0	58·0	52·0
Ga	15·0	17·0	18·0	20·0	15·0	15·0	14·0	13·0
Rb	134	164	128	217	92·0	27·0	46·0	96·0
Sr	654	539	299	559	667	598	567	800
Y*†	20·0*	18·1*	18·6*	23·1*	25·0*	13·0*	14·3*	15·2*
Zr	144	160	183	212	146	121	107	158
Nb*†	39·5	27·1	13·0	24·8	57·4	53·3	33·4	86·1
Mo*								
Sn*								
Sb*								
Cs*	3·83		4·60	6·04	1·00	0·31	1·02	0·58
Ba	1047	708	912	1062	813	719	799	1089
La*†	35·3	36·2	32·2	42·0	34·7	35·6	29·6	51·9
Ce*†	65·5	67·0	63·8	79·5	64·9	62·9	56·8	89·7
Pr*	7·70	7·55	7·51	9·54	7·81	6·69	6·42	9·12
Nd*	28·7	27·4	27·9	35·1	30·6	24·5	24·5	32·0
Sm*	5·32	5·09	5·24	6·50	6·08	4·57	4·83	5·52
Eu*	1·41	1·21	1·07	1·37	1·83	1·41	1·36	1·67

	Gourougou volcanic field—Si–K-rich group				Gourougou volcanic field—Si-poor group			
Locality:	Izmâniyine	Izarounalene	Ouixsane mine	Bou Hamza	Haidoun	Izarounalene	Trara	Beni Enzar
Latitude N:	35°16·30′	35°15·70′	35°07·57′	35°12·85′	35°17·89′	35°15·73′	35°13·17′	35°12·50′
Longitude W:	02°58·00′	02°57·10′	03°01·51′	03°06·21′	03°00·63′	02°57·04′	03°02·55′	02°55·47′
Sample:	GG140699-8 lava flow above trachyte	GG140699-6 lava flow	GG030699-1a intrusion	GG 280599-9 lava flow	GG070699-1c lava flow	GG290599-5 huge boulder in quarry	GG080400-3 lava flow	GG090400-1b lava flow coarser centre
Rock type:	basaltic trachyandesite	trachyandesite	diorite	trachyandesite	alkali basalt	alkali basalt	alkali basalt	trachybasalt
Gd*	4·47	4·55	4·10	5·19	5·30	4·38	4·45	5·01
Tb*	0·62	0·62	0·60	0·72	0·76	0·59	0·59	0·64
Dy*	3·53	3·61	3·37	4·09	4·33	3·33	3·36	3·55
Ho*	0·70	0·71	0·66	0·81	0·83	0·63	0·64	0·68
Er*	2·00	2·07	1·84	2·29	2·27	1·73	1·76	1·85
Tm*	0·28	0·31	0·26	0·33	0·31	0·24	0·25	0·26
Yb*	1·92	2·12	1·71	2·23	1·98	1·54	1·59	1·71
Lu*	0·29	0·32	0·24	0·34	0·29	0·22	0·23	0·24
Hf*	3·55	3·61	1·34	5·50	3·45	2·69	2·46	3·03
Ta*	2·21	1·72	0·94	1·47	3·17	2·85	1·81	4·68
W*								
Tl*	0·25		0·84	0·19	0·01			
Pb*†	5·56	3·39	9·16	4·19	2·19	3·57	3·48	4·04
Th*†	12·8	18·8	13·8	22·5	4·36	5·63	6·99	7·58
U*	4·23	5·67	3·98	8·28	1·21	1·51	2·02	1·94

	Guilliz volcanic field—Si–K-rich group				Guilliz volcanic field—Si-poor group			
Locality:	Jebel Guilliz	Jebel Guilliz	Jebel Guilliz	Jebel Guilliz	Jebel El Kehal	Jebel Guilliz	Jebel Guilliz	Ain Zora
Latitude N:	34°26·30′	34°27·70′	34°27·70′	34°27·70′	34°26·50′	34°25·99′	34°25·99′	34°39·43′
Longitude W:	03°19·30′	03°18·30′	03°18·30′	03°18·30′	03°31·60′	03°19·28′	03°19·28′	03°33·20′
Sample:	GZ040400-4 ash flow tuff mafic inclusion	GZ280300-3b pyrocl. deposit essential clast	GZ280300-4 intrusion	GZ280300-1 ash flow tuff	GZ 160699-5 lava flow	GZ040400-8 lava flow lowermost	GZ170699-4 lava flow uppermost	GZ160699-1 lava flow
Rock type:	trachyandesite	trachyte	trachyte	trachyte	alkali basalt	alkali basalt	alkali basalt	hawaiite
Major elements (wt %)								
SiO_2	56·9	62·8	62·2	65·9	45·1	46·1	47·5	48·3
TiO_2	1·19	0·79	0·97	0·51	2·30	1·66	1·65	1·98
Al_2O_3	16·8	15·7	16·2	16·1	13·2	15·7	16·6	16·5
FeO^T	5·70	4·25	4·95	3·06	10·4	9·31	9·48	8·96
MnO	0·15	0·12	0·11	0·03	0·17	0·16	0·17	0·15
MgO	1·57	1·17	0·88	0·55	10·9	9·88	8·34	7·42
CaO	4·48	2·66	2·91	1·41	10·8	9·52	10·6	8·64
Na_2O	5·72	4·49	4·48	5·36	3·21	2·85	2·83	4·00
K_2O	3·80	4·37	4·43	4·92	1·40	1·14	0·90	1·86
P_2O_5	0·46	0·29	0·35	0·14	0·62	0·36	0·32	0·45
H_2O	0·71	2·38	0·90	0·79	0·44	1·51	0·71	0·44
CO_2	0·87	0·11	0·16	0·27	0·61	0·08	0·31	0·03
Total	98·4	99·1	98·6	99·0	99·0	98·3	99·4	98·7

Table 2: continued

	Guilliz volcanic field—Si–K-rich group				Guilliz volcanic field—Si-poor group			
Locality:	Jebel Guilliz	Jebel Guilliz	Jebel Guilliz	Jebel Guilliz	Jebel El Kehal	Jebel Guilliz	Jebel Guilliz	Ain Zora
Latitude N:	34°26·30′	34°27·70′	34°27·70′	34°27·70′	34°26·50′	34°25·99′	34°25·99′	34°39·43′
Longitude W:	03°19·30′	03°18·30′	03°18·30′	03°18·30′	03°31·60′	03°19·28′	03°19·28′	03°33·20′
Sample:	GZ040400-4	GZ280300-3b	GZ280300-4	GZ280300-1	GZ 160699-5	GZ040400-8	GZ170699-4	GZ160699-1
	ash flow tuff	pyrocl. deposit	intrusion	ash flow tuff	lava flow	lava flow	lava flow	lava flow
	mafic inclusion	essential clast				lowermost	uppermost	
Rock type:	trachyandesite	trachyte	trachyte	trachyte	alkali basalt	alkali basalt	alkali basalt	hawaiite
Trace elements (ppm)								
Li*			19·2	26·0				
V	84·0	59·0	60·0	23·0	214	187	209	193
Cr	<18	<18	<18	<18	485	326	289	167
Co	14·0	9·00	9·00	5·00	48·0	47·0	43·0	36·0
Ni	7·00	2·00	2·00	<2	275	199	127	104
Zn	137	68·00	71·0	73·0	102	67·0	74·0	84·0
Ga	17·0	18·00	22·0	20·0	18·0	13·0	15·0	17·0
Rb	131	163	151	190	39·0	32·0	20·0	56·0
Sr	368	261	292	147	799	587	536	688
Y*†	38·9*	33·1*	37·9*	39·1*	23·1*	14·0*	22·7*	23·0*
Zr	379	429	428	467	176	105	128	167
Nb*†	74·9	66·3	75·6	109	69·0	37·7	30·0	54·0
Mo*			2·61	5·29				
Sn*			2·14	3·51				
Sb*								
Cs*	3·19	4·84	2·36	1·74	0·70	0·21	0·28	0·93
Ba	1227	707	782	509	557	424	323	628
La*†	71·8	67·4	65·1	70·7	47·8	23·9	20·3	34·3
Ce*†	125	126	125	133	85·0	45·3	40·8	62·6
Pr*	13·6	13·3	13·5	14·1	9·80	5·19	5·12	7·38
Nd*	48·4	46·3	47·6	47·5	37·2	20·3	21·2	28·4
Sm*	8·99	8·36	8·78	8·51	7·15	4·16	4·64	5·79
Eu*	2·51	1·75	1·88	1·21	2·22	1·44	1·55	1·81
Gd*	8·64	7·66	7·38	7·07	6·35	4·09	4·66	5·39
Tb*	1·26	1·11	1·14	1·14	0·89	0·58	0·71	0·79
Dy*	7·51	6·61	6·46	6·57	4·75	3·30	4·22	4·50
Ho*	1·48	1·30	1·25	1·31	0·86	0·62	0·84	0·85
Er*	4·19	3·81	3·44	3·72	2·18	1·66	2·30	2·27
Tm*	0·62	0·58	0·49	0·55	0·28	0·23	0·32	0·30
Yb*	4·09	3·92	3·08	3·67	1·69	1·42	2·05	1·94
Lu*	0·60	0·58	0·44	0·53	0·24	0·20	0·30	0·28
Hf*	7·37	6·62	1·17	4·51	4·44	2·31	3·13	4·03
Ta*	4·36	4·43	4·33	6·10	4·02	1·95	1·59	3·10
W*								
Tl*			0·18	0·25	0·03		0·03	0·04
Pb*†	13·1	15·5	12·9	9·57	3·18	1·27	2·05	3·11
Th*†	13·2	19·9	14·8	18·1	6·11	2·43	2·42	4·75
U*	3·19	4·59	2·39	4·70	1·57	0·65	0·53	1·26

	Guilliz volcanic field—Si-poor group			Oujda volcanic field—Si–K-rich group and Si-poor group				
Locality:	M. el Rhassoul	J. Tassatfacht	Ez Zerga	Ahfir due SE	Oujda Oued Isli	Oujda Oued Isli	Oujda Oued Isli	Oujda Koudiat Toulia
Latitude N:	34°36·42′	34°38·69′	34°30·25′	34°56·75′	34°31·76′	34°31·49′	34°33·84′	34°39·84′
Longitude W:	03°02·60′	03°23·09′	03°03·25′	02°05·30′	02°03·72′	02°03·55′	02°03·78′	02°06·69′
Sample:	GZ 180699-4 lava flow	GZ 150699-1 lava flow	GZ180699-5 lava flow	AF 1 cobble from creek bed	OD260599-10 lava flow above tuff ring	OD 260599-12 lava flow above ash layer	OD260599-1 lava flow	OD 300599-4 huge boulder on lava flow
Rock type:	alkali basalt	alkali basalt	alkali basalt	trachyandesite	basanite	basanite	basalt	basanite
Major elements (wt %)								
SiO_2	47·8	46·8	46·8	59·4	43·5	43·5	43·8	43·4
TiO_2	2·23	2·41	2·38	0·56	3·17	3·21	3·05	3·65
Al_2O_3	16·8	17·3	17·1	16·9	12·7	13·2	15·2	15·7
FeO^T	9·82	9·74	10·1	5·18	9·51	9·67	11·1	10·9
MnO	0·17	0·16	0·17	0·07	0·17	0·18	0·21	0·19
MgO	6·74	6·31	5·39	0·98	9·51	8·88	6·59	6·28
CaO	9·33	10·3	10·4	5·63	12·1	12·0	10·9	10·6
Na_2O	3·88	3·00	2·64	2·40	3·16	2·56	3·67	3·05
K_2O	0·83	1·66	1·58	3·98	2·97	2·63	0·96	2·99
P_2O_5	0·44	0·52	0·42	0·36	0·68	0·70	0·80	0·68
H_2O	1·24	1·28	0·99	2·03	0·75	2·58	2·86	1·43
CO_2	0·02	0·03	0·42	1·17	0·33	0·08	0·12	0·08
Total	99·3	99·5	98·5	98·6	98·6	99·2	99·2	98·9
Trace elements (ppm)								
Li*				9·96				
V	284	307	314	75·0	313	314	368	387
Cr	169	91·0	84·0	18·0	532	419	97·0	62·0
Co	41·0	39·0	40·0	12·0	35·0	37·0	45·0	34·0
Ni	72·0	57·0	53·0	<2	115	108	68·0	44·0
Zn	90·0	86·0	91·0	58·0	84·0	93·0	112	103
Ga	15·0	17·0	18·0	21·0	19·0	16·0	15·0	18·0
Rb	8·00	26·0	48·0	135	104·0	93·0	19·0	94·0
Sr	587	740	676	713	1070	1148	1113	1055
Y*†	25·5*	21·3*	24·9*	21·9	24·0*	24·9*	38·9*	29·4*
Zr	172	162	171	301	324	350	356	369
Nb*†	53·0	49·0	44·0	23·4	117	127	117	112
Mo*				0·65				
Sn*				0·74				
Sb*								
Cs*	0·48	2·13	0·74	1·95	0·88	0·93	0·91	1·24
Ba	413	652	468	1459	924	989	799	943
La*†	33·3	36·1	30·5	68·4	75·0	78·8	80·1	67·5
Ce*†	64·4	70·2	60·9	147	150	154	158	136
Pr*	7·82	8·51	7·51	16·63	18·0	18·7	19·3	16·6
Nd*	30·4	32·9	30·0	60·9	67·4	69·4	71·5	63·6
Sm*	5·99	6·27	6·09	10·5	10·8	10·8	12·3	11·0
Eu*	1·88	1·81	1·84	2·19	2·90	2·97	3·35	3·06
Gd*	5·56	5·38	5·52	6·87	7·97	8·12	9·97	8·59
Tb*	0·83	0·76	0·81	0·88	1·02	1·03	1·38	1·14

Table 2: continued

	Guilliz volcanic field—Si-poor group			Oujda volcanic field—Si–K-rich group and Si-poor group				
Locality:	M. el Rhassoul	J. Tassatfacht	Ez Zerga	Ahfir due SE	Oujda Oued Isli	Oujda Oued Isli	Oujda Oued Isli	Oujda Koudiat Toulia
Latitude N:	34°36·42′	34°38·69′	34°30·25′	34°56·75′	34°31·76′	34°31·49′	34°33·84′	34°39·84′
Longitude W:	03°02·60′	03°23·09′	03°03·25′	02°05·30′	02°03·72′	02°03·55′	02°03·78′	02°06·69′
Sample:	GZ 180699-4 lava flow	GZ 150699-1 lava flow	GZ180699-5 lava flow	AF 1 cobble from creek bed	OD260599-10 lava flow above tuff ring	OD 260599-12 lava flow above ash layer	OD260599-1 lava flow	OD 300599-4 huge boulder on lava flow
Rock type:	alkali basalt	alkali basalt	alkali basalt	trachyandesite	basanite	basanite	basalt	basanite
Dy*	4·83	4·26	4·68	4·19	5·23	5·27	7·65	5·99
Ho*	0·94	0·80	0·92	0·74	0·92	0·93	1·46	1·09
Er*	2·60	2·14	2·49	1·97	2·35	2·43	3·96	2·87
Tm*	0·36	0·29	0·34	0·26	0·30	0·32	0·53	0·37
Yb*	2·32	1·83	2·28	1·71	1·84	1·96	3·39	2·34
Lu*	0·34	0·26	0·33	0·24	0·26	0·28	0·49	0·34
Hf*	4·18	3·68	3·92	2·76	7·67	7·81	8·59	7·98
Ta*	3·14	2·93	2·76	1·34	8·46	8·97	8·65	8·07
W*								
Tl*	0·03	0·19	0·07	0·20	0·04	0·05	0·06	0·05
Pb*†	2·51	3·65	2·62	9·57	4·24	4·54	4·70	4·15
Th*†	3·71	4·96	4·25	32·6	7·91	8·35	8·49	7·28
U*	1·12	1·71	1·50	5·99	2·41	2·58	2·69	2·24

	Oujda volcanic field—Si–K-rich group and Si-poor group						
Locality:	Oujda Semmara	Oujda Oujda	Oujda Oued Lakram	Oujda Jorf Lakhdar	Plateau du Rekkam near Tissaf	Plateau du Rekkam near Tissaf	Plateau du Rekkam near Tissaf
Latitude N:	34°38·85′	34°40·42′	34°42·32′	34°42·02′	33°26·11′	33°24·10′	33°24·05′
Longitude W:	01°57·83′	01°57·21′	02°03·03′	01°56·78′	03°35·18′	03°31·05′	03°28·00′
Sample:	OD 260599-13 huge lava flow	OD190699-1a lava flow	OD 020699-2b lava flow middle	OD020699-1b lava flow upper	PR020400-1b cobble from lava flow	PR020400-4a lava flow	PR020400-5 cobble from river bed
Rock type:	basanite	basanite	alkali basalt	trachyandesite	basanite	basanite	basanite
Major elements (wt %)							
SiO_2	43·6	42·7	44·2	52·3	38·7	39·3	42·1
TiO_2	3·47	3·47	3·44	1·84	2·78	2·85	3·09
Al_2O_3	16·0	15·7	15·8	18·5	10·9	11·6	12·4
FeO^T	10·8	11·3	10·7	7·40	12·6	12·3	11·9
MnO	0·20	0·20	0·19	0·24	0·22	0·21	0·17
MgO	6·11	6·02	5·65	2·24	12·0	11·1	10·6
CaO	9·85	10·4	10·5	6·09	12·5	12·6	10·5
Na_2O	3·24	3·35	2·31	4·01	3·43	3·46	3·49
K_2O	3·23	3·06	1·97	3·69	0·87	1·05	1·08
P_2O_5	0·75	0·78	0·71	0·80	1·66	1·42	0·90
H_2O	1·56	1·56	3·33	1·51	3·04	2·64	2·32
CO_2	0·10	0·45	0·04	0·07	0·08	0·12	0·11
Total	98·9	99·0	98·7	98·7	98·8	98·6	98·6

	Oujda volcanic field—Si–K-rich group and Si-poor group						
Locality:	Oujda Semmara	Oujda Oujda	Oujda Oued Lakram	Oujda Jorf Lakhdar	Plateau du Rekkam near Tissaf	Plateau du Rekkam near Tissaf	Plateau du Rekkam near Tissaf
Latitude N:	34°38·85′	34°40·42′	34°42·32′	34°42·02′	33°26·11′	33°24·10′	33°24·05′
Longitude W:	01°57·83′	01°57·21′	02°03·03′	01°56·78′	03°35·18′	03°31·05′	03°28·00′
Sample:	OD 260599-13 huge lava flow	OD190699-1a lava flow	OD 020699-2b lava flow middle	OD020699-1b lava flow upper	PR020400-1b cobble from lava flow	PR020400-4a lava flow	PR020400-5 cobble from river bed
Rock type:	basanite	basanite	alkali basalt	trachyandesite	basanite	basanite	basanite
Trace elements (ppm)							
Li*							
V	359	367	360	90·0	239	234	249
Cr	60·0	25·0	<18	<18	382	346	358
Co	34·0	37·0	37·0	17·0	68·0	64·0	57·0
Ni	47·0	37·0	35·0	7·00	324	255	281
Zn	107	107	98·0	114	139	131	117
Ga	18·0	19·0	16·0	20·0	17·0	14·0	15·0
Rb	111·0	116·0	21·0	110	35·0	36·0	36·0
Sr	1086	1159	1168	1256	1419	1459	1159
Y*†	30·8*	30·1*	29·0*	42·7*	21·2*	24·5*	19·7*
Zr	377	393	366	471	325	318	258
Nb*†	120	134	112	124	127	116	76·4
Mo*							
Sn*							
Sb*							
Cs*	1·31	1·27	1·69	2·00	0·23	0·38	0·26
Ba	1062	881	918	1240	917	827	675
La*†	77·1	78·8	71·6	92·7	94·5	92·3	71·0
Ce*†	151	153	140	180	180	177	135
Pr*	18·0	18·7	17·1	21·4	19·9	19·9	14·9
Nd*	67·3	70·8	64·2	78·9	74·5	74·9	56·5
Sm*	11·4	11·8	10·9	13·1	13·1	13·3	10·4
Eu*	3·17	3·25	3·06	3·62	3·90	3·99	3·14
Gd*	8·93	9·07	8·58	10·4	11·0	11·2	8·77
Tb*	1·19	1·20	1·13	1·46	1·32	1·36	1·09
Dy*	6·32	6·32	5·95	8·14	6·39	6·64	5·39
Ho*	1·16	1·14	1·10	1·57	1·04	1·10	0·88
Er*	3·03	2·98	2·84	4·39	2·47	2·63	2·11
Tm*	0·40	0·39	0·38	0·61	0·29	0·32	0·25
Yb*	2·54	2·41	2·39	4·06	1·72	1·84	1·43
Lu*	0·37	0·34	0·34	0·60	0·22	0·24	0·18
Hf*	8·21	8·03	8·13	10·3	6·54	6·25	5·60
Ta*	8·77	9·26	8·44	9·59	6·94	6·07	4·23
W*							
Tl*	0·05	0·07	0·01	0·12			
Pb*†	5·05	4·36	3·25	8·49	2·43	3·61	2·67
Th*†	8·74	8·04	8·11	10·9	5·61	6·87	4·58
U*	2·69	2·71	2·35	2·48	2·38	2·47	1·44

*Data obtained by ICP-MS.
†Data are obtained by XRF.
Rock classification on volatile-free basis.

range from 8·19 to 6·37 Ma (Table 1 and Figs 1 and 2) and are within the range of published K/Ar ages (8·6–6·2 Ma) (Nobel *et al.*, 1981; Bellon *et al.*, 1983). The 10·8 ± 1 Ma K/Ar age for a lamproite from the Vera basin (Bellon & Brousse, 1977) was not confirmed by laser $^{40}Ar/^{39}Ar$ age dating. The 6·76 ± 0·04 Ma matrix $^{40}Ar/^{39}Ar$ age from La Celia near Jumilla is identical within error to a published Ar/Ar whole-rock age of 6·8 ± 0·4 Ma (Turner *et al.*, 1999). A systematic relationship between the new Ar/Ar ages and older K/Ar age data was not detected. As inferred from geological maps, the laser $^{40}Ar/^{39}Ar$ age data are consistent with stratigraphic evidence showing that lamproitic rocks are generally associated with Upper Miocene marine sediments (mostly marls and sandstones) in the Murcia area. Field observations in the Vera basin show that lamproitic lava flows, showing pillow structures, were emplaced and chilled in soft, wet Messinian marine muds (peperites). Two lamproitic peperites were dated at 6·44 Ma and 6·37 Ma and are consistent with the Messinian ages of their host marine sediments. A newly discovered lamproitic dyke (VE290699-10A) yielded a phlogopite age of 7·45 ± 0·08 Ma. It intrudes rhyodacitic breccias cut by the Palomares fault and the dyke itself has been tectonically deformed. Thus the new age data also provide constraints for the minimum age of the breccia and the tectonic history of the Palomares fault zone.

Si-poor, Na-rich volcanic rocks from the Tallante volcanic field (two hawaiites and one trachybasalt), which are spatially associated with the Si–K-rich (lamproitic) rocks, yielded amphibole + biotite, glass and matrix mean apparent ages and step heating ages ranging from 2·93 to 2·29 Ma (Table 1 and Figs 1 and 2). For Tallante, the ages are consistent with field evidence showing that the volcanic units overlie Tortonian, Messinian and Pliocene sediments and are in good agreement with published K/Ar ages ranging from 2·8 to 2·7 Ma (Bellon *et al.*, 1983). The 10·5 Ma Ar/Ar phlogopite age for a Tallante lava reported by Turner *et al.* (1999) is not consistent with these Pliocene ages. Phlogopite is not a common phenocryst phase in basaltic magmas, as it is stable only at high pressures and becomes unstable upon extrusion (Deer *et al.*, 1996). Ultramafic mantle xenoliths frequently associated with the alkali basalts from Tallante contain phlogopite (Dupuy *et al.*, 1986; Capedri *et al.*, 1989) and, therefore, the phlogopites dated by Turner *et al.* (1999) may be xenocrysts from disaggregated mantle xenoliths. In conclusion, the transition from Si–K-rich to Si-poor, Na-rich volcanic rocks occurred between 6·4 to 2·9 Ma at the southern Iberian continental margin.

The northwestern African margin

Si–K-rich igneous rocks from the Gourougou volcanic field (basaltic trachyandesites, trachyandesites, andesite and one diorite) yielded matrix mean apparent and isochron ages on biotite and feldspar ranging from 7·58 to 4·8 Ma (Table 1 and Figs 1 and 2). These ages are largely consistent with the range of whole-rock and biotite-separate K/Ar age data (9·0 to 4·6 Ma) (Bellon & Brousse, 1977; Hernandez & Bellon, 1985; El Bakkali *et al.*, 1998) and $^{40}Ar/^{39}Ar$ age data (6·73 to 6·0 Ma) (Roger *et al.*, 2000) for volcanic tuffs interbedded with Messinian marine sediments, which were deposited on the slope of the Gourougou stratovolcanic complex. Si-poor, Na-rich alkali basalts and trachybasalts were erupted on the flanks of the Gourougou stratovolcano between 6·3 and 3·73 Ma (Table 1). Lava flows directly overlie Messinian marine sediments (e.g. Haidoun flow, dated at 3·73 Ma). Previously determined K/Ar ages generally tend to be younger (e.g. 2·5 Ma for Haidoun) (Bellon & Brousse, 1977) than the laser $^{40}Ar/^{39}Ar$ age data. In the Gourougou volcanic system, the transition from Si–K-rich to Si-poor, Na-rich igneous activity occurred between 6·3 and 4·8 Ma.

Si–K-rich igneous rocks (trachyandesite to trachyte) from the Jebel Guilliz stratovolcano located in the centre of the Guilliz volcanic field yielded mean apparent ages for feldspar and biotite + feldspar ranging from 6·90 to 6·82 Ma (Table 1 and Figs 1 and 2). Mean apparent ages for matrix and feldspar + matrix from Si-poor, Na-rich alkali basalts in the Guilliz volcanic field range from 6·3 to 0·65 Ma (Table 1 and Figs 1 and 2). Most published K/Ar ages (8·0 to 4·9 Ma) (Hernandez & Bellon, 1985) fall within this range but some K/Ar ages tend to be older. Major discrepancies between the new laser $^{40}Ar/^{39}Ar$ age data (0·65 Ma and 0·88 Ma) and the K/Ar (1·74 Ma and 2·5 Ma) (Hernandez & Bellon, 1985) data from the literature exist for the Si-poor lavas from the Ain Zora and Jebel El Kehal lava flows in the westernmost Guilliz area. The new age data suggest that volcanism in the westernmost Guilliz volcanic field was active contemperanously with the Quaternary alkali basaltic volcanism of the nearby Middle Atlas mountains (1·8 to 0·5 Ma, K/Ar ages) (Bellon & Brousse, 1977; Harmand & Cantagrel, 1984). In the Guilliz area, the transition from Si–K-rich to Si-poor, Na-rich igneous rocks occurred between 6·8 and 6·3 Ma.

The Oujda–Algeria area includes igneous rocks from northwestern Algeria, the Oujda volcanic field and the Plateau du Rekkam area situated south of the Oujda area. Based on K/Ar age data, Si–K-rich magmatism (high-K calc-alkaline and shoshonitic series) in northwestern Algeria occurred at the Middle–Upper Miocene boundary and ceased in the Upper Miocene (11·7 to 7·5 Ma) (Louni-Hacini *et al.*, 1995; Coulon *et al.*, 2002). Si-poor, Na-rich rocks (basanites, alkali basalts and trachyandesites) from the Oujda volcanic field yielded matrix and biotite mean apparent ages ranging from 3·78 to 3·10 Ma (Table 1). These ages show that the eruption history of the Oujda volcanic field has a much

narrower range than hitherto thought based on published whole-rock K/Ar age data (6·2 to 1·5 Ma) (Bellon & Letouzey, 1977; Tisserant *et al.*, 1985; Andries & Bellon, 1989). Two altered lava flows outcropping in the vicinity of the Oued Isly southwest of Oujda were K/Ar dated at 6·2 and 5·6 Ma (Andries & Bellon, 1989). These flows overlie Tortonian blue marls (Marnes bleues) and so may correlate with Messinian marine sediments (Marnes jaunes) in the Oujda area (Jadid *et al.*, 1999). However, redating of the flows in this area with the laser $^{40}Ar/^{39}Ar$ technique (3·78 to 3·10 Ma) was not able to confirm the Late Miocene K/Ar ages (Table 1). Based on K/Ar age data, Si-poor volcanic rocks from northwestern Algeria show a much wider age range (10·0–7·2 Ma and 4·3–0·8 Ma) (Fig. 2) (Louni-Hacini *et al.*, 1995; Coulon *et al.*, 2002) than Si-poor volcanic rocks from the Oujda volcanic field (3·78–3·10 Ma) (this study). However, additional laser $^{40}Ar/^{39}Ar$ age dating is necessary to confirm the older K/Ar ages from northwestern Algeria, in particular the onset and termination of Si–K-rich and Si-poor magmatism. Plateau du Rekkam volcanic rocks SE of the Oujda volcanic field probably erupted in the Plio-Quaternary (Saadi *et al.*, 1985). In the Oujda–Algeria area, the transition from Si–K-rich to Si-poor, Na-rich magmatism apparently took place between 10·0 and 7·5 Ma.

In summary, the transition from Si–K-rich to Si-poor volcanism occurred between 6·4 and 2·9 Ma in southern Spain, between 6·3 and 4·8 Ma in the Gourougou area, between 6·8 and 6·3 Ma in the Guilliz area, and possibly between 10·0 and 7·5 Ma in the Oujda–Algeria area.

Major and trace element data

Major and trace element data for 145 igneous rocks from the southern Iberian and northwestern African continental margins are presented in Table 2 and Electronic Appendix 2. The Electronic Appendix includes the full dataset and is available from the *Journal of Petrology* website at http://www.petrology.oupjournals.org, whereas Table 2 is a reduced version that includes major and trace element data only for samples that were selected for Sr–Nd–Pb-isotope analysis.

The comprehensive dataset allows division of the post-collisional igneous rocks from the westernmost Mediterranean into a Si-rich and a Si-poor group (Fig. 3a). Based on the K_2O content, the Si-rich samples can be further subdivided into a relatively K-poor group and a K-rich group (Fig. 3b). The Middle to Upper Miocene (12·1 to 6·1 Ma) K-poor group includes low-K (tholeiitic) and medium- to high-K (calc-alkaline) basalts through rhyolites outcropping in the Alboran Basin area (Hoernle *et al.*, 1999; Duggen *et al.*, 2004; Gill *et al.*, 2004). The occurrence of Upper Miocene to Lower Pliocene (8·2 Ma and 4·8 Ma) K-rich magmatism, including high-K to shoshonitic series basaltic andesites and basaltic trachyandesites to dacites and trachytes and lamproitic rocks is restricted to the southern Iberian and northwestern African continental margins. Upper Miocene to Pliocene (6·3 and 0·65 Ma) Si-poor volcanic rocks are spatially associated with the Si–K-rich group rocks, and range from alkali basalts and basanites to hawaiites and tephrites and tend to have higher Na_2O contents for a given K_2O concentration than the K-rich group. Below we describe the major and trace element composition of the Si–K-rich and Si-poor group rocks from the continental margins of southern Iberia and northwestern Africa.

The southern Iberian continental margin

Si–K-rich volcanic rocks from southeastern Spain (lamproites and their derivatives) show a large range in most major and trace element contents. MgO (1·5–12·9 wt %) correlates inversely with SiO_2 and Al_2O_3 and positively with TiO_2, Nb, Ta, Nd, Sm, Zr, Eu, Hf, Gd, Sn, Cr and Ni (with r^2 for the regression line >0·7, except for Ni, which shows a curved correlation with MgO) (Fig. 4). Most of these systematic geochemical variations can be explained by fractional crystallization of common phenocryst phases in the Spanish lamproites such as olivine (containing Cr-spinel), phlogopite, apatite and sanidine (Venturelli *et al.*, 1988; Toscani *et al.*, 1995). There is a compositional continuum between high-MgO lamproites, their low-MgO derivatives (some of which contain crustal xenocrysts such as garnet and cordierite) and cordierite–garnet-bearing volcanic rocks from southeastern Spain (e.g. Cerro Hoyazo) (Fig. 4a–d). The Si–K-rich, lamproitic rocks from southern Spain have enriched incompatible element contents and exhibit spiked patterns on primitive mantle normalized multi-element diagrams (Fig. 5a), resulting from an enrichment of fluid-mobile, incompatible elements such as Rb, Ba, (± Th), U, K, Pb (and Cs, Sn, Sb and Li) relative to incompatible elements that are less fluid-mobile or fluid-immobile [e.g. rare earth elements (REE), Nb, Ta]. Strong enrichments of the light and middle REE relative to heavy REE result in high (LREE, MREE)/HREE ratios (e.g. La/Yb = 34–71). A strong LREE enrichment is associated with depletion of Eu relative to Sm and Gd as reflected by negative Eu anomalies ($Eu/Eu^* = 0·52–0·67$). Enrichment of fluid-mobile relative to less fluid-mobile elements and pronounced troughs in Nb and Ta are typical features of subduction zone magmas (e.g. Aeolian Islands and Izu–Bonin arc lavas in Fig. 5c) (Ellam *et al.*, 1988, 1989; Taylor & Nesbitt, 1998).

Si-poor volcanic rocks from Tallante in southeastern Spain have MgO contents ranging from 3·6 to 8·5 wt %. MgO correlates negatively with Al_2O_3, Nb, Ta, Zr and Hf

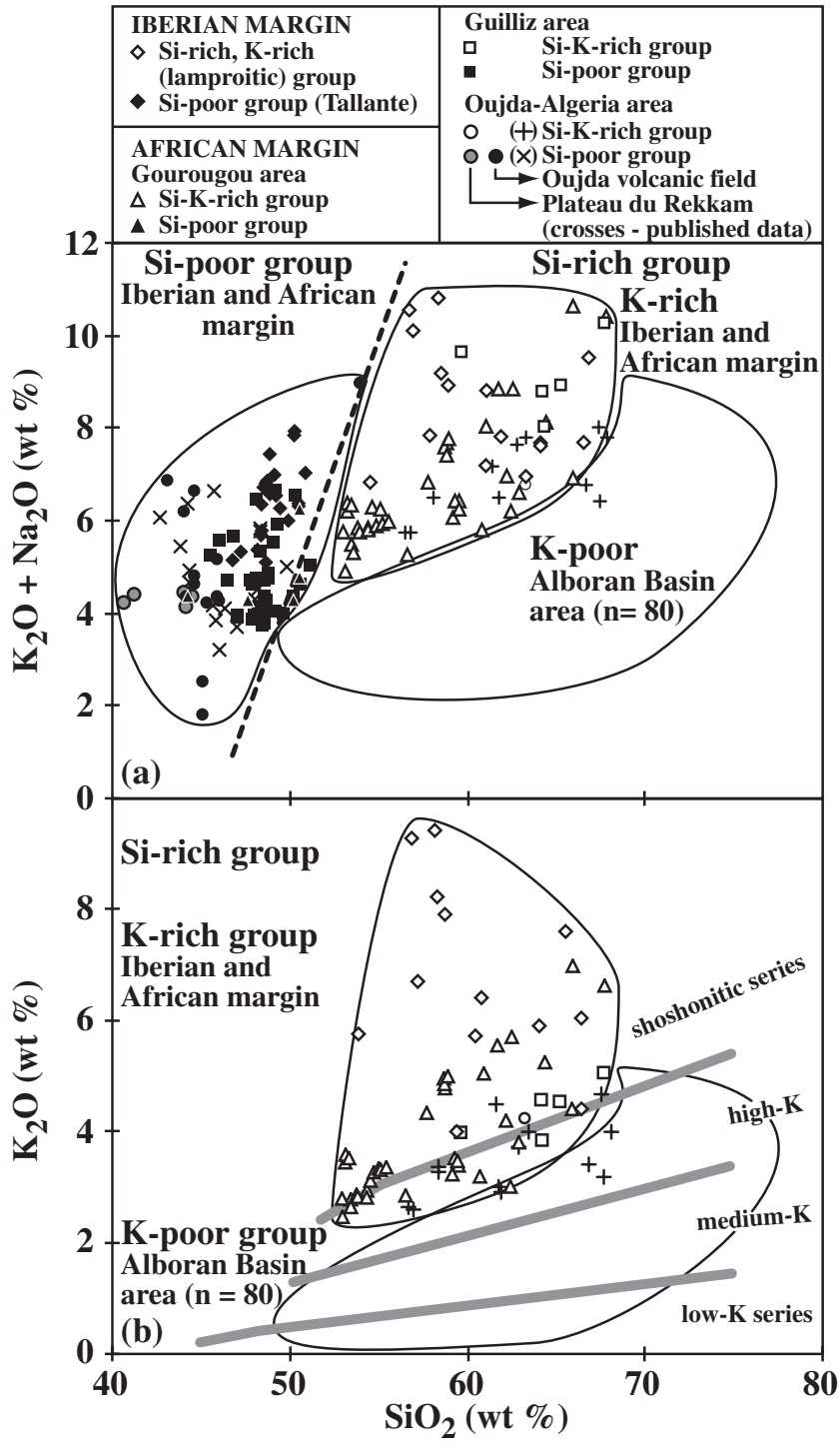

Fig. 3. SiO_2 vs total alkalis ($Na_2O + K_2O$ wt %) (a) and SiO_2 vs K_2O (b) diagrams illustrating the differences in major element geochemistry of the post-collisional Miocene to Quaternary westernmost Mediterranean igneous rocks. The Si-rich group can be subdivided into K-poor and K-rich groups based on their K content. The K-poor group includes low-K (tholeiitic) and medium-K to high-K (calc-alkaline) series from the Alboran Basin area (present Alboran Sea, the Alboran Island and several coastal areas such as Aguilas block and Cabo de Gata in Spain, Ras Tarf and Trois Furches in Morocco) (Fig. 1). The K-rich group includes high-K calc-alkaline and shoshonitic series and ultrapotassic rocks (Spanish lamproites) from southeastern Spain, northern Morocco and northeastern Algeria. The Si-poor group includes alkali basalts and basanites to hawaiites and tephrites from southeastern Spain, northern Morocco and northwestern Algeria. Data sources: subdivision lines in the SiO_2 vs K_2O diagram from Rickwood (1989); Alboran Sea volcanic rocks from Hoernle *et al.* (1999), Duggen *et al.* (2004) and Gill *et al.* (2004); Si–K-rich and Si-poor igneous rocks from Algeria are from Louni-Hacini *et al.* (1995) and Coulon *et al.* (2002).

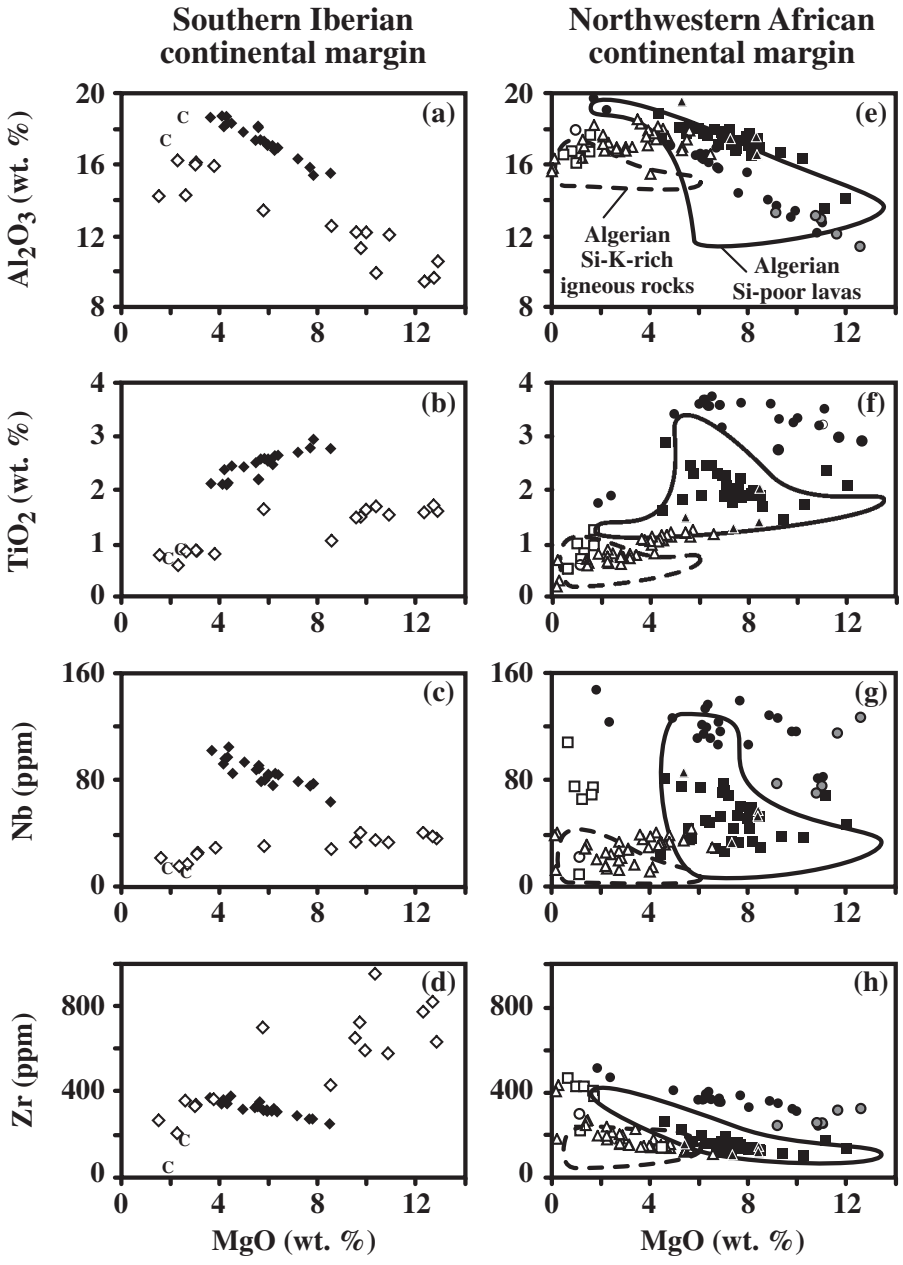

Fig. 4. Variations of Al_2O_3, TiO_2, Nb and Zr with vs MgO wt % for Si–K-rich and Si-poor igneous rocks from the southern Iberian (a–d) and northwestern African continental (e–h) margins. Data sources: cordierite–garnet-bearing Cerro Hoyazo lavas (denoted by C) from Turner *et al.* (1999) and Duggen *et al.* (2004); Si–K-rich and Si-poor igneous rocks from northwestern Algeria from Louni-Hacini *et al.* (1995) and Coulon *et al.* (2002). Symbols are as in Fig. 3.

and positively with TiO_2, Cr and Ni ($r^2 > 0{\cdot}7$) (Fig. 4a–d), generally consistent with the fractionation of the observed phenocryst assemblages (e.g. olivine, clinopyroxene and magnetite). The Si-poor group samples from the Iberian continental margin generally exhibit contrasting multi-element patterns to the Si–K-rich group showing relative enrichments of fluid-immobile Nb and Ta and relative depletion of fluid-mobile elements K, ± Pb, and have lower Rb, Ba, Th, U, K and Pb, but higher Sr and Ti concentrations than the Si–K-rich volcanic rocks. The Si-poor group lavas have geochemical signatures similar to those of ocean-island basalts (OIB) and lavas from continental intraplate volcanic settings (e.g. Massif Central, St. Helena and Canary Islands in Fig. 5d). The Tallante lavas, however, show deviations from typical intraplate-type, multi-element patterns with positive Th–U anomalies, highly variable K anomalies and Pb anomalies ranging from negative to positive.

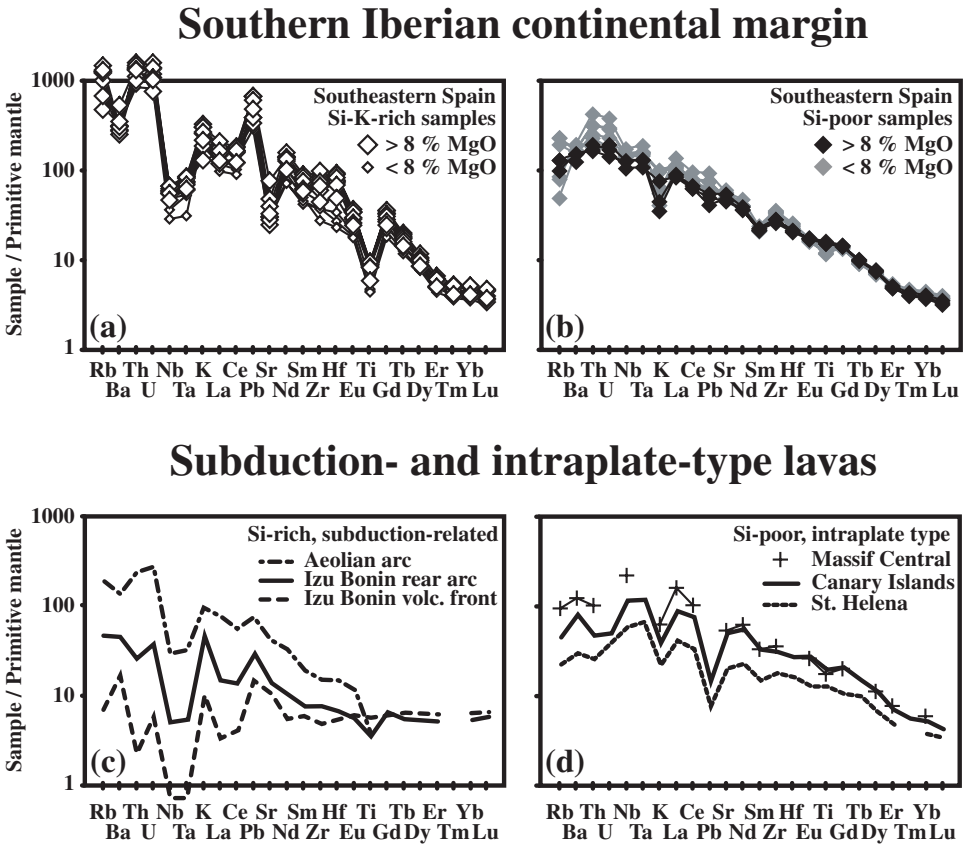

Fig. 5. Primitive mantle normalized multi-element patterns of Si–K-rich (a) and Si-poor (b) post-collisional igneous rocks from the southern Iberian continental margin compared with patterns for typical subduction-related (c) and intra-plate (d) lavas. Data sources: primitive mantle from Hofmann (1988); Massif Central from Wilson & Downes (1991); Canary Islands from Hoernle (unpublished data); St. Helena from Chaffey *et al.* (1989) and Thirlwall (1997); Aeolian arc from Ellam *et al.* (1988, 1989); Izu–Bonin arc from Taylor & Nesbitt (1998).

The northwestern African continental margin

The Si–K-rich igneous rocks from the northwestern African margin also show a large variation in major and trace element composition. MgO ranges from 0·1 to 6·6 wt % and correlates positively with CaO, TiO_2, FeO, CaO/Al_2O_3, Co (Gourougou) and MnO, Co, V (Guilliz) and negatively with SiO_2, K_2O, total alkalis, Rb (Gourougou) and K_2O and Li (Guilliz) ($r^2 > 0{\cdot}7$) (Fig. 4e–h). In multi-element diagrams, Si–K-rich group rocks from Gourougou at the northwestern African margin show spiked patterns as a result of enrichment of fluid-mobile elements Rb, U and K relative to less fluid-mobile or fluid-immobile elements (e.g. REE, Nb and Ta) (Fig. 6a). However, the behaviour of Pb is more complex, showing both positive and negative anomalies, and the troughs in Nb and Ta of some samples are only moderately pronounced. The more evolved Si–K-rich samples from Guilliz have smooth patterns and show neither positive nor negative anomalies for the fluid-mobile elements Rb, Th, U, K and Pb and fluid-immobile elements Nb and Ta. The only negative anomalies are for Ba, Sr and Ti, and there is a slight positive anomaly for Zr (Fig. 6c). The Si–K-rich sample from the Oujda–Algeria area (Ahfir sample; open circle, Fig. 6e) shows enrichment of fluid-mobile Rb, Ba, Th and U relative to fluid-immobile Nb and Ta but lacks peaks for fluid-mobile elements K and Pb. The multi-element pattern of the Ahfir sample is largely subparallel to that of both the mafic and evolved Si–K-rich samples from northwestern Algeria (Fig. 6e) (Louni-Hacini *et al.*, 1995; Coulon *et al.*, 2002). Volcanic rocks having distinct troughs in Nb and Ta but only slight positive peaks for fluid-mobile elements can be found in the active Aeolian subduction zone (Fig. 5c).

For the Si-poor, Na-rich lavas, MgO (1·8–12·6 wt %) correlates positively with Cr, Ni, Ga (Gourougou), Cr, Ni (Guilliz) and CaO, CaO/Al_2O_3, Cr, Ni (Oujda area) and inversely with Al_2O_3, K_2O, Th (Gourougou), Al_2O_3 (Guilliz) and Al_2O_3, MnO, Cs, Zr, Hf, Eu, Yb, Lu and Y (Oujda) ($r^2 \geq 0{\cdot}7$, except for Cr and Ni, which show curved correlations with MgO) (Fig. 4e–h). The Oujda samples also show a strong decrease in TiO_2, FeO, Co and V as MgO decreases below 3 wt %. These systematic correlations between major and trace elements point to

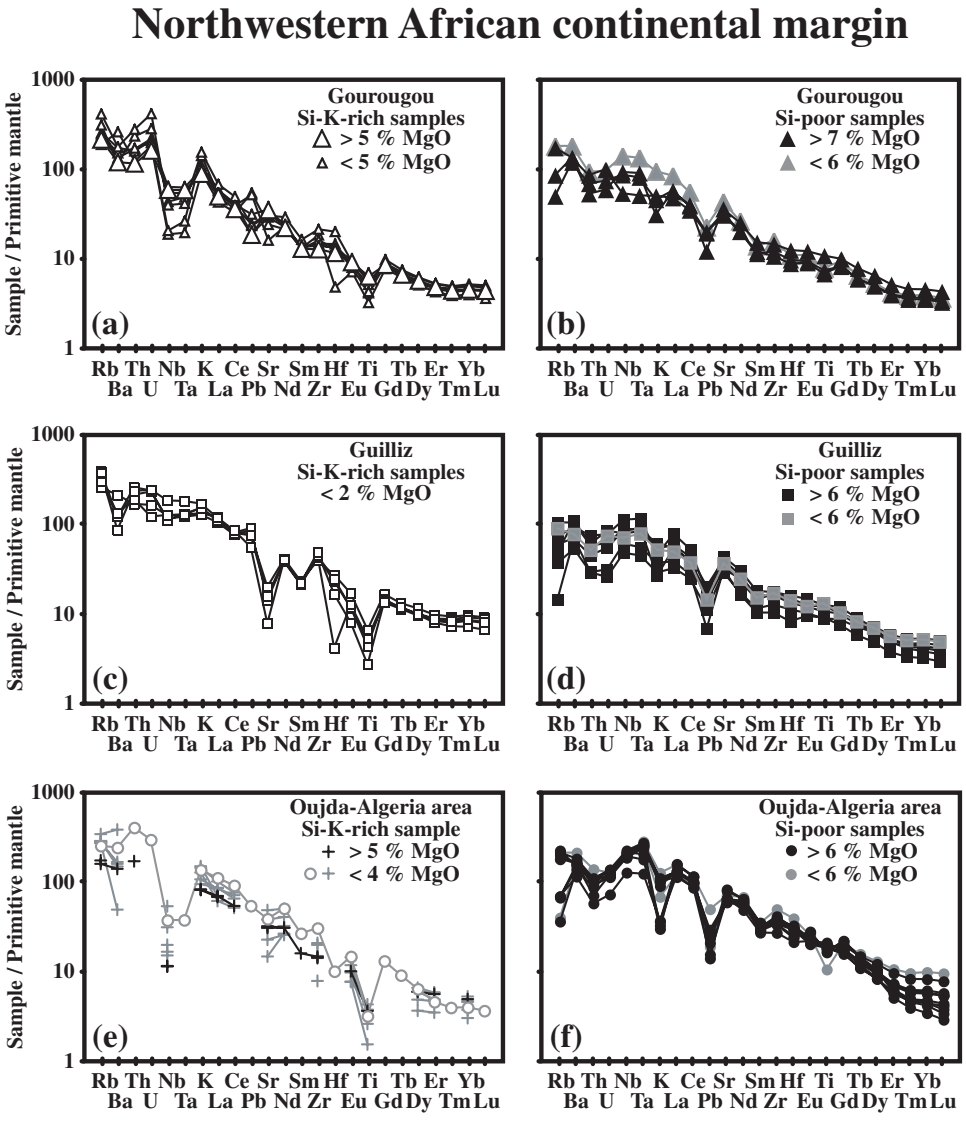

Fig. 6. Primitive mantle normalized multi-element patterns of Si–K-rich (a, c, e) and Si-poor (b, d, f) post-collisional igneous rocks from the northwestern African continental margin. Data sources: Gourougou, Guilliz and Oujda areas from this study; primitive mantle from Hofmann (1988); Si–K-rich igneous rocks from Algeria (+) from Louni-Hacini *et al.* (1995) and Coulon *et al.* (2002).

the fractional crystallization of the observed phenocryst assemblages (olivine, clinopyroxene and magnetite). In multi-element diagrams (Fig. 6b, d, f), the Si-poor lavas from northwestern Africa generally show contrasting patterns to the Si–K-rich group as a result of a relative depletion in fluid-mobile elements Rb, Th, U, K and Pb, compared with less fluid-mobile elements such as the REE, Nb and Ta. These patterns are similar to those of lavas from oceanic intraplate-type volcanic settings (e.g. St. Helena and Canary Islands in Fig. 5d) (Chaffey *et al.*, 1989; Thirlwall, 1997). Several Si-poor samples from Gourougou and Guilliz, however, show only weak Nb and Ta anomalies, and a distinct negative K anomaly is lacking.

It should be emphasized that several samples from both the Si–K-rich group and the Si-poor group show deviations from typical subduction-related or intraplate-type geochemical fingerprints and have hybrid compositions between the two end-member geochemical signatures (Figs 5 and 6). Some of the Si–K-rich samples lack relative enrichment and even show slight relative depletion in some fluid-mobile elements (in particular Th, U, K and Pb for Guilliz and Pb for Gourougou lavas). These samples also display large ranges in fluid-mobile to fluid-immobile element ratios, which have values between those found in OIB and subduction zone lavas. The Si–K-rich volcanic rocks from Gourougou, for example, have U/Nb = 0·09–0·33 and K/La = 732–1143,

whereas similar rocks from Guilliz have U/Nb = 0·03–0·07 and K/La = 461–582. Some mafic Si-poor samples exhibit less pronounced depletion or even slight enrichment in fluid-mobile elements (e.g. Th, U, K and Pb for Guilliz and Gourougou lavas and Th, U, K and Pb for Tallante lavas). Selective addition of strongly fluid-mobile elements relative to much less fluid-mobile elements, which have almost identical partition coefficients (such as Pb relative to Ce) cannot be significantly controlled by differences in the degree of partial melting or by fractional crystallization processes in mafic magmas but could reflect binary mixing of magmas from different sources, derivation from a subduction-modified mantle source or crustal assimilation.

Sr–Nd–Pb-isotope data

Sr–Nd–Pb-isotope data for 52 igneous rocks from the southern Iberian and northwestern African continental margins are reported in Table 3. Figures 7, 8, 10 and 11 display age-corrected Sr–Nd–Pb-isotope ratios.

The southern Iberian continental margin

Si–K-rich, lamproitic rocks have high initial $^{87}Sr/^{86}Sr$ ratios (0·7161–0·7230) and low initial $^{143}Nd/^{144}Nd$ ratios (0·51215–0·51223) (Fig. 7a, c, d). The Sr-isotope ratios reported here slightly extend the range of published data (0·7166–0·7207) (Nelson, 1992; Turner *et al.*, 1999) but the new Nd-isotope ratios are significantly higher and show much less scatter than published data ($^{143}Nd/^{144}Nd$ = 0·51197–0·51214, normalized to $^{146}Nd/^{144}Nd$ = 0·7219 and age corrected to 7 Ma) (Nelson, 1992; Turner *et al.*, 1999). The Si–K-rich, lamproitic rocks show a relatively narrow range in initial $^{206}Pb/^{204}Pb$ (18·71–18·85), $^{207}Pb/^{204}Pb$ (15·66–15·69) and $^{208}Pb/^{204}Pb$ ratios (38·90–39·13) and have high Δ7/4 (14·3–16·5) and Δ8/4 (61·4–76·8) (Fig. 7b) [Δ7/4 and Δ8/4 notations denote the vertical deviation from the Northern Hemisphere Reference Line (NHRL), in the $^{206}Pb/^{204}Pb$ vs $^{207}Pb/^{204}Pb$ and $^{208}Pb/^{204}Pb$ diagrams, respectively] (Hart, 1984). It should be noted that the Si–K-rich, lamproitic rocks, however, have Nd and Pb isotopic compositions very similar to those of cordierite-bearing rocks from southeastern Spain (Fig. 7a, b, d).

Si-poor, Na-rich lavas from southeastern Iberia have relatively low initial $^{87}Sr/^{86}Sr$ ratios (0·7037–0·7046) and relatively high initial $^{143}Nd/^{144}Nd$ ratios (0·51283–0·51298) (Fig. 7a, c, d). Despite higher initial $^{206}Pb/^{204}Pb$ (18·88–18·98) compared with the Si–K-rich, lamproitic rocks, the Si-poor lavas from Tallante have similar $^{207}Pb/^{204}Pb$ and $^{208}Pb/^{204}Pb$ ratios (15·65–15·67 and 38·9–39·0) to the Si–K-rich rocks from the same area and therefore plot well above the NHRL, also having relatively high Δ7/4 and Δ8/4 (10·2–13·3 and 38·6–54·7; Fig. 7b).

The northwestern African continental margin

Si–K-rich igneous rocks from the African continental margin show a wide range of initial $^{87}Sr/^{86}Sr$ ratios (0·7040–0·7100) and initial $^{143}Nd/^{144}Nd$ ratios (0·51236–0·51284), similar to the range reported for the Oujda–Algeria area ($^{87}Sr/^{86}Sr_{initial}$ = 0·7043–0·7096 and $^{143}Nd/^{144}Nd_{initial}$ = 0·51226–0·51254) (Coulon *et al.*, 2002) (Fig. 7a, c, d). On Pb-isotope diagrams, they show a limited range for initial $^{206}Pb/^{204}Pb$ (18·7–19·0) and $^{207}Pb/^{204}Pb$ (15·63–15·70) ratios and plot above the NHRL (Δ7/4 = 7·1–12·9, Δ8/4 = 30·7–56·9; Fig 7b).

Most Si-poor, Na-rich lavas from the northwestern African continental margin have lower initial $^{87}Sr/^{86}Sr$ (0·7029–0·7045) and higher $^{143}Nd/^{144}Nd$ (0·51274–0·51303) than the spatially associated Si–K-rich rocks and overlap with the range reported for Si-poor rocks from northern Algeria ($^{87}Sr/^{86}Sr_{initial}$ = 0·7032–0·7060 and $^{143}Nd/^{144}Nd_{initial}$ = 0·51255–0·51292) (Coulon *et al.*, 2002) (Fig. 7a, c, d). The African Si-poor rocks exhibit a large range in initial Pb-isotope ratios ($^{206}Pb/^{204}Pb$ = 18·85–20·75, $^{207}Pb/^{204}Pb$ = 15·65–15·67, $^{208}Pb/^{204}Pb$ = 38·9–39·0), although the range within the individual volcanic areas is much more limited, with the exception of lavas from the Plateau du Rekkam volcanic field in the Oujda–Algeria area (Fig. 7b). Si-poor samples from Gourougou and Guilliz plot well above the NHRL (except one sample) (Δ7/4 = −0·1–9·2, Δ8/4 = −2·2–43·8) and the data fields overlap those of the spatially associated Si–K-rich rocks but extend to more radiogenic Pb isotopic composition. Most Si-poor volcanic rocks from the Oujda–Algeria area plot below the NHRL (Δ7/4 = −7·7–5·8, Δ8/4 = −42·1–34·8) and fall within the field for Ahaggar volcanic rocks (southern Algeria) (Allègre *et al.*, 1981) and two samples have $^{206}Pb/^{204}Pb$ ratios as high as St. Helena OIB (Chaffey *et al.*, 1989). The variation in $^{206}Pb/^{204}Pb$ ratio for Si-poor lavas from the northwestern African margin almost covers the field for the modelled composition of young HIMU plotting below the NHRL, reflecting the composition of MORB with a $^{238}U/^{204}Pb$ of 10 and a 0·5–1·5 Gyr recycling time (Thirlwall, 1997) (Fig. 7b). In contrast to the young HIMU field, most Si-poor lavas plot closer to or lie above the NHRL; Si-poor Oujda lavas, however, overlap with the low-velocity component (LVC) (Hoernle *et al.*, 1995).

DISCUSSION

Temporal evolution of volcanism at the Iberian and African margins

Dating of the westernmost Mediterranean igneous rocks suggests that the transition from Si–K-rich to Si-poor, Na-rich compositions occurred between 6·4 and 2·9 Ma in Spain along the southern Iberian continental margin,

Table 3: Sr–Nd–Pb isotopic data for igneous rock samples from the southern Iberian and northwestern African continental margins

	Age	$^{87}Sr/^{86}Sr$	$^{87}Sr/^{86}Sr$	$^{143}Nd/^{144}Nd$	$^{143}Nd/^{144}Nd$	ε_{Nd}	$^{206}Pb/^{204}Pb$	$^{207}Pb/^{204}Pb$	$^{208}Pb/^{204}Pb$	$^{206}Pb/^{204}Pb$	$^{207}Pb/^{204}Pb$	$^{208}Pb/^{204}Pb$	Δ7/4	Δ8/4	$^{238}U/^{204}Pb$	$^{232}Th/^{238}U$	$^{232}Th/^{204}Pb$
	(Ma)	measured	initial	measured	initial	initial	measured	measured	measured	initial	initial	initial	init.	init.	μ	κ	ω
Southern Iberian continental margin																	
Southeastern Spanish volcanic field—Si–K-rich group																	
CAL090599-1	8	0·722489(8)	0·722018	0·512167(8)	0·512161	−9·2	18·805(8)	15·692(6)	39·033(2)	18·772	15·691	38·990	16·5	66·7	26·3	108·8	4·1
LC100599-4	**6·76**	0·717242(8)	0·717191	0·512180(7)	0·512175	−8·9	18·786(7)	15·682(6)	39·028(2)	18·777	15·682	39·007	15·5	67·8	8·5	65·6	7·7
CX110599-3	**7·04**	0·718273(8)	0·718046				18·817(7)	15·689(6)	39·041(2)	18·803	15·689	39·015	15·9	65·5	13·2	72·7	5·5
ZN130599-1	**8·08**	0·721532(7)	0·721285	0·512203(7)	0·512196	−8·5	18·733(7)	15·675(6)	38·976(1)	18·719	15·674	38·957	15·4	69·9	11·0	47·0	4·3
FT120599-5	**7·13**	0·718420(7)	0·718015	0·512190(8)	0·512184	−8·7	18·771(6)	15·680(5)	39·036(1)	18·757	15·680	39·018	15·5	71·4	13·4	51·3	3·8
FT120599-16A	**7·25**	0·719075(8)	0·718742	0·512190(7)	0·512184	−8·7	18·839(10)	15·682(8)	39·179(2)	18·802	15·680	39·127	15·1	76·8	32·7	144·6	4·4
BQ170599-9	**6·94**	0·721167(8)	0·720814	0·512196(7)	0·512191	−8·6	18·791(8)	15·679(7)	39·007(1)	18·762	15·678	38·970	15·3	65·9	26·8	106·6	4·0
AL140599-1	**8·02**	0·720800(7)	0·720599	0·512213(8)	0·512207	−8·3	18·727(7)	15·663(6)	38·935(1)	18·707	15·662	38·902	14·3	65·8	15·8	84·0	5·3
LM160300-1	**7·12**	0·720825(8)	0·720557	0·512179(8)	0·512174	−9·0	18·868(33)	15·693(27)	39·065(7)	18·848	15·692	39·041	15·8	62·7	17·8	68·7	3·9
VE290699-2	**6·44**	0·723278(8)	0·722958	0·512159(8)	0·512154	−9·3	18·800(7)	15·679(6)	38·976(2)	18·778	15·678	38·943	15·1	61·4	22·7	102·5	4·5
VE290699-10A	**7·45**	0·716228(8)	0·716082	0·512240(7)	0·512235	−7·8	18·790(6)	15·675(5)	38·985(1)	18·776	15·674	38·966	14·8	63·8	11·9	50·8	4·3
Southeastern Spanish volcanic field (Tallante)—Si-poor group																	
TA 200400-1	**2·29**	0·703985(9)	0·703981	0·512957(7)	0·512955	6·2	18·944(1)	15·652(1)	38·961(2)	18·936	15·652	38·950	10·8	42·9	23·0	4·3	99·4
LP140599-5	**2·38**	0·704363(7)	0·704349	0·512858(7)	0·512856	4·3	18·904(1)	15·665(1)	39·011(1)	18·894	15·665	38·996	12·5	52·7	28·7	4·4	125·7
LP140599-5	**2·38**						18·910(1)	15·673(1)	39·039(2)	18·900	15·673	39·024	13·3	54·7	28·7	4·5	129·2
dupl.																	
CT270300-1a	**2·93**	0·703979(8)	0·703966	0·512926(6)	0·512924	5·6	18·945(2)	15·668(2)	39·034(4)	18·932	15·667	39·017	12·4	50·1	27·3	4·5	121·9
TA 260300-7	2·3	0·703955(8)	0·703950	0·512927(7)	0·512925	5·6	18·914(1)	15·655(1)	38·962(1)	18·904	15·654	38·951	11·4	46·8	26·1	3·6	95·0
TA 260300-6a	2·3	0·704194(8)	0·704186	0·512902(9)	0·512900	5·1	18·924(1)	15·664(1)	39·018(2)	18·915	15·664	39·004	12·2	50·9	25·2	4·7	118·7
TA 260300-4	2·3	0·704565(8)	0·704561	0·512828(7)	0·512827	3·7	18·889(1)	15·658(1)	38·981(1)	18·878	15·657	38·966	12·0	51·5	30·0	4·6	137·6
LP170300-1	2·3	0·703755(9)	0·703748	0·512980(7)	0·512978	6·7	18·988(1)	15·651(1)	38·973(2)	18·979	15·650	38·959	10·2	38·6	25·6	4·8	122·0

Table 3: continued

	Age (Ma)	$^{87}Sr/^{86}Sr$ measured	$^{87}Sr/^{86}Sr$ initial	$^{143}Nd/^{144}Nd$ measured	$^{143}Nd/^{144}Nd$ initial	ε_{Nd} initial	$^{206}Pb/^{204}Pb$ measured	$^{207}Pb/^{204}Pb$ measured	$^{208}Pb/^{204}Pb$ measured	$^{206}Pb/^{204}Pb$ initial	$^{207}Pb/^{204}Pb$ initial	$^{208}Pb/^{204}Pb$ initial	$\Delta 7/4$ init.	$\Delta 8/4$ init.	$^{238}U/^{204}Pb$ μ	$^{232}Th/^{238}U$ κ	$^{232}Th/^{204}Pb$ ω
Northwestern African continental margin																	
Gourougou volcanic field—Si-rich, K-rich group																	
GG140699-12	**4·8**	0·704768(9)	0·704691	0·512722(8)	0·512718	1·6	18·922(1)	15·634(1)	38·801(2)	18·873	15·632	38·752	9·5	30·7	65·5	3·2	208·3
GG140699-6	**5·35**	0·704662(9)	0·704635	0·512714(7)	0·512710	1·5	18·976(1)	15·647(1)	38·896(3)	18·887	15·643	38·798	10·5	33·7	107·7	3·4	368·5
GG290599-1	**5·51**	0·704250(9)	0·704205	0·512786(8)	0·512782	2·9	18·885(2)	15·627(2)	38·754(4)	18·846	15·635	38·741	10·1	33·0	62·9	3·0	187·6
GG290599-1 dupl.	**5·51**						18·899(1)	15·638(1)	38·793(2)	18·831	15·625	38·703	9·2	30·9	62·9	3·0	187·5
GG140699-8	**5·57**	0·704663(9)	0·704612	0·512749(9)	0·512745	2·2	18·942(1)	15·638(1)	38·827(2)	18·900	15·636	38·785	9·6	30·9	48·9	3·1	153·2
GG280599-9	**6·12**	0·706233(9)	0·706189				18·901(1)	15·643(0)	38·853(1)	18·780	15·637	38·746	11·0	41·4	127·1	2·8	355·8
GG140699-4	**6·69**	0·708367(7)	0·708311	0·512495(8)	0·512490	−2·8	18·869(0)	15·647(0)	38·880(1)	18·843	15·645	38·857	11·2	44·9	24·5	2·8	69·2
GG030699-1a	**7·58**	0·709808(8)	0·709675	0·512374(7)	0·512368	−5·1	18·822(1)	15·651(1)	38·859(1)	18·789	15·650	38·822	12·2	47·8	27·9	3·6	100·1
Gourougou volcanic field—Si-poor group																	
GG070699-1c	**3·73**	0·703955(9)	0·703933	0·512948(8)	0·512945	6·0	19·112(1)	15·622(1)	38·881(2)	19·091	15·621	38·857	6·0	14·9	35·5	3·7	132·6
GG070699-1c dupl.	**3·73**						19·107(1)	15·615(1)	38·859(2)	19·087	15·614	38·835	5·4	13·2	35·5	3·7	132·5
GG290599-5	**4·4**	0·703405(8)	0·703356	0·513024(7)	0·513021	7·5	18·989(1)	15·603(0)	38·736(1)	18·971	15·602	38·713	5·4	15·1	27·2	3·9	104·8
GG090400-1b	**5·4**	0·703340(9)	0·703301	0·513022(7)	0·513018	7·5	19·169(1)	15·610(1)	38·894(2)	19·139	15·609	38·856	4·3	9·0	30·9	4·0	125·1
GG080400-3	**6·3**	0·704522(9)	0·704464	0·512779(7)	0·512774	2·8	18·922(1)	15·626(1)	38·787(2)	18·882	15·624	38·741	8·6	28·6	37·2	3·6	133·2
Guilliz volcanic field—Si-rich, K-rich group																	
GZ280300-4	**6·82**	0·704935(9)	0·704790	0·512768(6)	0·512763	2·5	18·829(1)	15·635(1)	38·971(2)	18·817	15·635	38·946	10·4	56·9	11·9	6·4	76·3
GZ280300-1	**6·83**	0·704749(7)	0·704386				18·995(1)	15·623(1)	38·991(1)	18·995	15·621	38·948	7·1	35·6	31·6	4·0	126·2
GZ280300-3B	**6·90**	0·704936(9)	0·704758	0·512756(8)	0·512751	2·3	18·842(1)	15·638(1)	38·992(3)	18·842	15·637	38·962	10·3	55·5	19·1	4·5	85·6
GZ040400-4	7	0·704140(9)	0·704038	0·512842(8)	0·512837	4·0	18·937(1)	15·638(1)	39·035(1)	18·937	15·637	39·012	9·3	48·9	15·7	4·3	67·1
Guilliz volcanic field—Si-poor group																	
GZ160699-1	**0·65**	0·703571(7)	0·703574	0·512841(4)	0·512967	6·4	19·112(1)	15·608(1)	38·935(2)	19·109	15·608	38·932	4·5	20·2	26·1	3·9	101·9
GZ160699-1 dupl.	**0·65**	0·703576(10)	0·703569	0·512968(8)	0·512840	4·0											

	Age (Ma)	$^{87}Sr/^{86}Sr$ measured	$^{87}Sr/^{86}Sr$ initial	$^{143}Nd/^{144}Nd$ measured	$^{143}Nd/^{144}Nd$ initial	ε_{Nd} initial	$^{206}Pb/^{204}Pb$ measured	$^{207}Pb/^{204}Pb$ measured	$^{208}Pb/^{204}Pb$ measured	$^{206}Pb/^{204}Pb$ initial	$^{207}Pb/^{204}Pb$ initial	$^{208}Pb/^{204}Pb$ initial	$\Delta 7/4$ init.	$\Delta 8/4$ init.	$^{238}U/^{204}Pb$ μ	$^{232}Th/^{238}U$ κ	$^{232}Th/^{204}Pb$ ω
GZ160699-5	**0·88**	0·703273(8)	0·703271	0·513026(9)	0·513025	7·6	19·359(1)	15·608(2)	39·110(2)	19·354	15·608	39·105	1·9	7·8	31·9	4·0	128·6
GZ170699-4	**4·06**	0·703163(9)	0·703157	0·512832(4)	0·512829	3·8	18·908(1)	15·604(1)	38·927(2)	18·897	15·603	38·912	6·4	43·8	16·7	4·7	78·5
GZ180699-4	**5·3**	0·703372(8)	0·703369	0·512965(7)	0·512961	6·4	19·319(1)	15·623(5)	39·111(2)	19·295	15·622	39·086	3·9	13·0	28·9	3·4	99·0
GZ150699-1	**5·8**	0·703859(8)	0·703851	0·512881(9)	0·512877	4·7	19·110(1)	15·630(1)	39·033(1)	19·083	15·628	39·006	6·9	30·8	30·3	3·0	90·5
GZ040400-8	6·3*	0·702931(10)	0·702917	0·513037(7)	0·513032	7·8	19·322(1)	15·583(1)	38·966(2)	19·289	15·581	38·926	−0·1	−2·2	33·2	3·9	128·2
GZ180699-5	5	0·703564(8)	0·703564	0·512803(4)	0·512800	3·2											
Oujda volcanic field—Si-K-rich group																	
AF 1	10	0·710196(9)	0·710118	0·512237(4)	0·512230	−7·7	18·774(1)	15·651(1)	38·907(2)	18·711	15·648	38·795	12·9	54·7	40·2	5·6	225·7
Oujda and Plateau du Rekkam volcanic field—Si-poor group																	
OD260599-12	**3·10**	0·703618(7)	0·703608	0·512880(7)	0·512878	4·7	20·297(1)	15·675(1)	40·064(2)	20·279	15·674	40·045	−1·5	−10·0	37·8	3·3	126·5
OD260599-1	**3·40**	0·703742(7)	0·703740	0·512739(5)	0·512736	2·0	19·938(2)	15·650(2)	39·728(4)	19·919	15·649	39·708	−0·1	−0·1	37·7	3·3	123·2
OD020699-2b	**3·44**			0·512880(7)	0·512878	4·7	20·111(1)	15·667(1)	39·930(2)	20·086	15·666	39·901	−0·3	−1·0	47·9	3·6	171·0
OD300599-4	**3·47**	0·703842(9)	0·703829	0·512905(7)	0·512903	5·2	20·021(1)	15·657(1)	39·800(2)	20·001	15·656	39·780	−0·3	−2·9	35·6	3·4	119·8
OD260599-13	**3·62**	0·703858(9)	0·703843	0·512901(9)	0·512899	5·1	19·983(1)	15·651(1)	39·785(2)	19·963	15·650	39·763	−0·5	0·1	35·1	3·4	118·0
OD260599-10	**3·72**	0·703593(9)	0·703578	0·512879(8)	0·512877	4·7	20·318(2)	15·673(1)	40·074(3)	20·296	15·672	40·051	−1·9	−11·5	37·9	3·4	128·4
OD020699-1b	**3·73**	0·704231(9)	0·704218	0·512880(7)	0·512878	4·7	19·344(1)	15·646(3)	39·365(1)	19·333	15·645	39·349	5·8	34·8	19·0	4·5	86·5
OD190699-1a	**3·78**	0·703890(8)	0·703874	0·512908(7)	0·512906	5·3	20·030(3)	15·656(2)	39·833(6)	20·002	15·652	39·801	−0·8	−0·9	41·1	3·1	125·9
OD190699-1a dupl.	**3·78**						20·026(1)	15·653(1)	39·824(2)								
PR020400-1b	4	0·703103(8)	0·703095	0·513000(7)	0·512997	7·1	19·342(2)	15·561(2)	39·077(4)	19·302	15·559	39·046	−2·4	8·3	63·5	2·4	154·4
PR020400-4a	4	0·703033(8)	0·703019	0·513007(5)	0·513004	7·2	20·784(4)	15·665(3)	40·326(9)	20·756	15·664	40·299	−7·7	−42·1	45·9	2·9	132·1
PR020400-5	4	0·703057(8)	0·703048	0·512974(7)	0·512971	6·6	20·630(5)	15·652(4)	40·456(9)	20·607	15·651	40·433	−7·4	−10·8	36·1	3·3	118·8

Locations are listed in Table 2. Residues of mafic samples were measured for Sr as well as Nd and Pb isotopic composition after acid wash by boiling the powder in 6 M HCl for 1 h. Age data are from Table 1 (bold) or estimated (plain).
*Sample GZ040400-8 is from the same stratigraphic height as sample GZ170699-3.

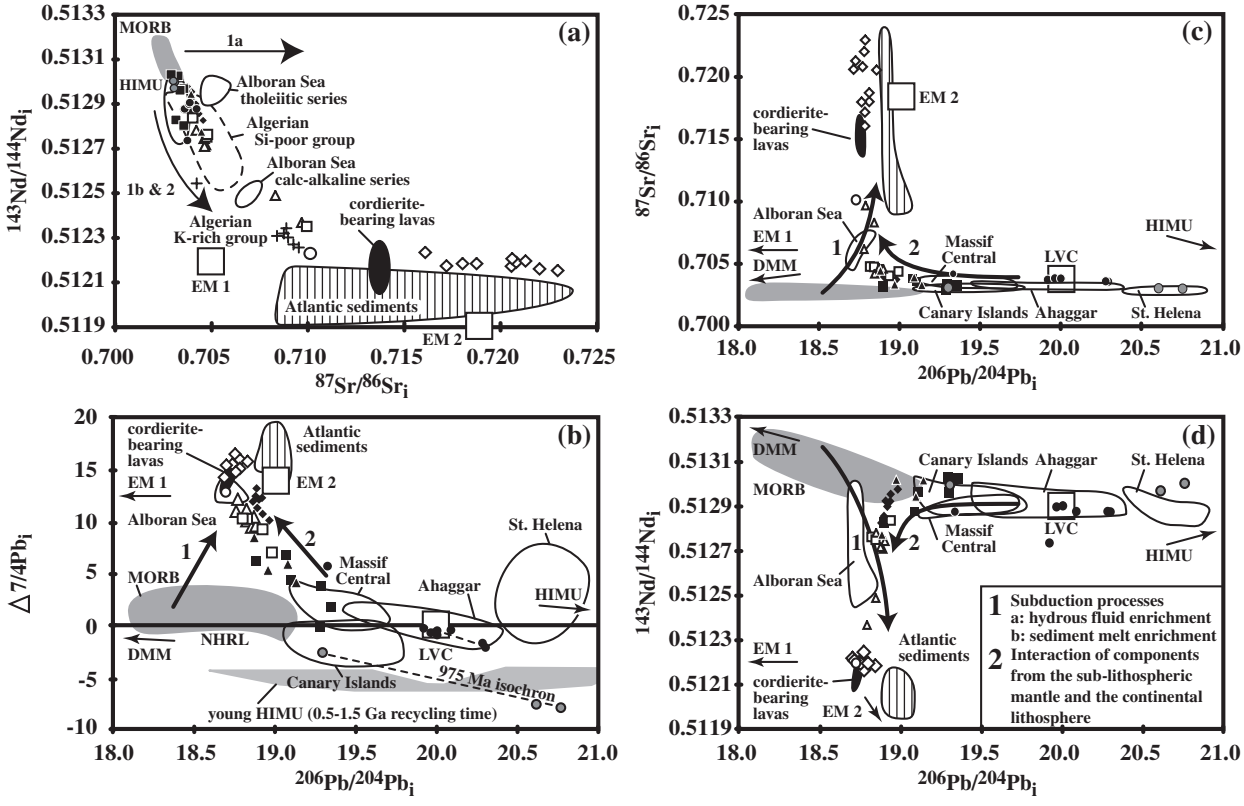

Fig. 7. Initial Sr–Nd–Pb-isotope data for western Mediterranean Miocene to Pleistocene igneous rocks. Symbols are as in Fig. 3. Arrow 1 reflects modification of a depleted MORB mantle through subduction processes. Arrows 1a and 1b indicate enrichment of the mantle beneath the Alboran Basin with hydrous fluids and partial melts from subducted marine sediment, respectively (Duggen *et al.*, 2004). Arrow 2 indicates interaction between sub-lithospheric melts and the continental lithosphere or melts derived therefrom. The polygonal field in the uranogenic Pb-isotope diagram (7) encircles geochemical modelling results for relatively young recycled oceanic crust (MORB) that developed a high time-integrated $^{238}U/^{204}Pb$ ratio (HIMU). Starting composition for the modelling is ancient, unaltered MORB with $^{206}Pb/^{204}Pb = 17{\cdot}8–18{\cdot}8$, $^{207}Pb/^{204}Pb = 15{\cdot}42–15{\cdot}53$ and $^{238}U/^{204}Pb = 10$. Data sources: mantle end-members DMM, HIMU, EM1 and EM2 from Zindler & Hart (1986) and Hofmann (1997); LVC from Hoernle *et al.* (1995); Ahaggar from Allègre *et al.* (1981); St. Helena from Chaffey *et al.* (1989); Holocene Canary Islands from Hoernle (unpublished data); Atlantic MORB between 10° and 70°N from Ito *et al.* (1987) and Dosso *et al.* (1991); Northern Hemisphere Reference Line (NHRL) from Hart (1984); Algerian Si-poor and Si–K-rich igneous rocks from Coulon *et al.* (2002); Atlantic sediments from the continental slope of northwestern Africa (age corrected to 15 Myr ago) from Hoernle *et al.* (1991), Hoernle (1998) and Duggen *et al.* (2004); cordierite-bearing volcanic rocks from southeastern Spain from Turner *et al.* (1999) and Duggen *et al.* (2004); Alboran Sea volcanic rocks with magma $\delta^{18}O = 5{\cdot}6–6{\cdot}5‰$ from Duggen *et al.* (2004).

between 6·8 and 4·8 Ma in Morocco and possibly between 10·0 and 7·5 Ma in Algeria within the northwestern continental African margin (Fig. 8a–h) (Louni-Hacini *et al.*, 1995; El Bakkali *et al.*, 1998; Coulon *et al.*, 2002).

The transition also occurred in individual volcanic systems such as the Gourougou and Guilliz stratovolcanic complexes over shorter timescales (Figs 1, 2 and 8a–h). At the Gourougou stratovolcanic complex, Si–K-rich igneous activity occurred from the Late Miocene to Early Pliocene (7·58 to 4·8 Ma) partially overlapping the Latest Miocene to Early Pliocene Si-poor volcanism (6·3 to 3·73 Ma), which erupted from localized vents on the flanks of the stratovolcano. In the Guilliz volcanic field, a short interval of *c.* 0·4 Myr separates Late Miocene Si-rich explosive and intrusive volcanism (6·90 to 6·69 Ma) from the eruption of lava flows from scoria cones with Si-poor compositions in the Latest Miocene to Pleistocene (6·3 to 0·65 Ma). The Si–K-rich Gourougou igneous rocks show a systematic change in their geochemical characteristics with decreasing age over a time span of about 3 Myr (7·58 to 4·8 Ma). This is observed in their major and trace element and Nd isotope ratios (e.g. K_2O/Na_2O, K_2O/Al_2O_3, Ba/Sr, Th/Nb, K/Nb, K/La, Pb/Ce, $^{87}Sr/^{86}Sr$, Δ7/4Pb decrease and Nb/La, Nb/Zr and $^{143}Nd/^{144}Nd$ increase) (Fig. 8a–c, f, h). A similar geochemical evolution is observed in the Si-poor Gourougou lavas, which show a systematic decrease of incompatible element ratios (e.g. Ba/Sr, K/La, K/Nb,

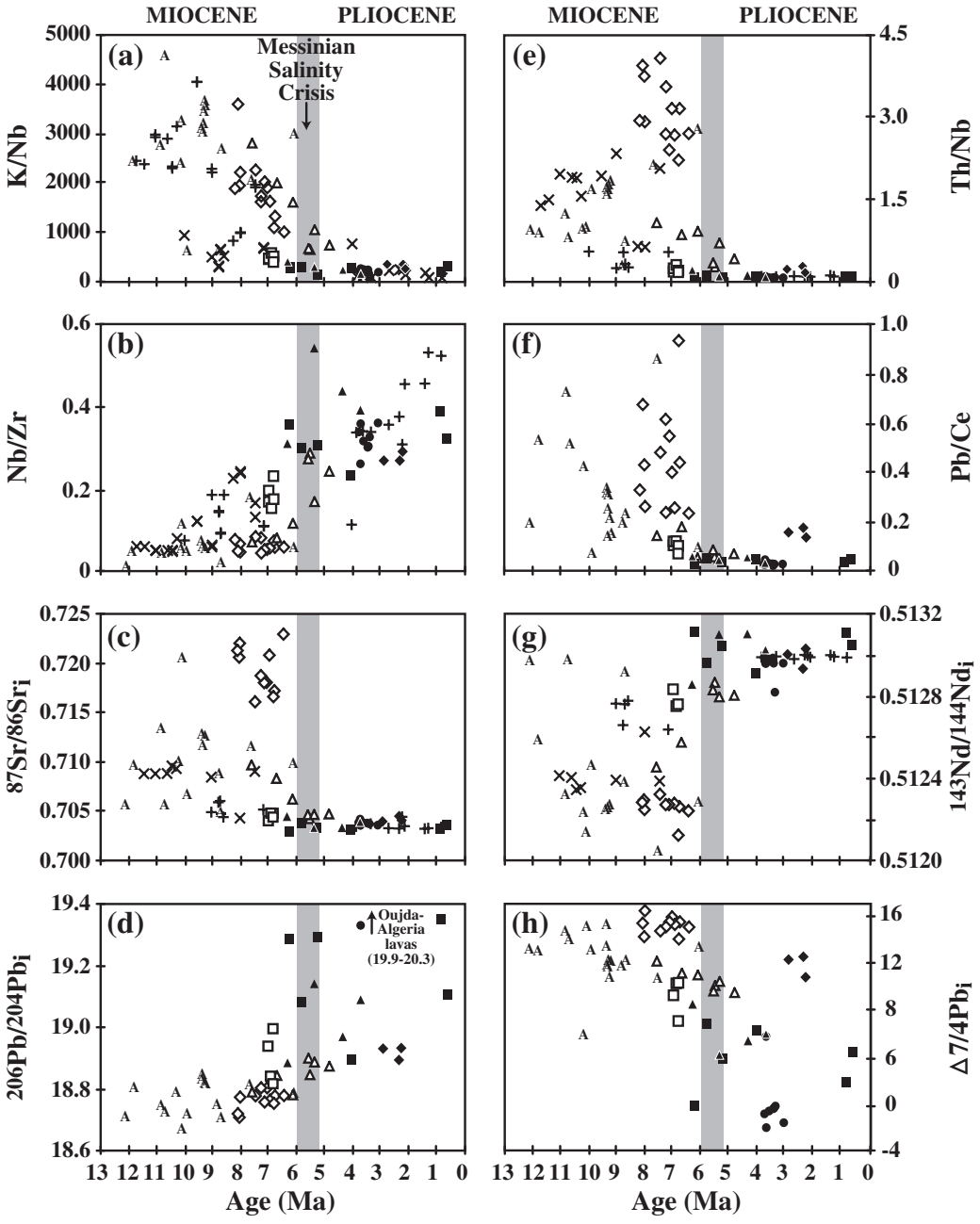

Fig. 8. $^{40}Ar/^{39}Ar$ age data (and Algerian K/Ar age data) vs element–element and initial Sr–Nd–Pb-isotope ratios showing the westernmost Mediterranean post-collisional transition from Si-rich, subduction-related to Si-poor, intraplate-type compositions at the Miocene–Pliocene boundary. Symbols are as in Fig. 3. 'A' denotes lavas from the Alboran Basin area as defined in the captions of Figs 2 and 3. It should be noted that the transition occurred both on a regional scale and in individual volcanic systems such as the Gourougou and Guilliz volcanic fields and overlaps with the Messinian Salinity Crisis. Additional data sources: Alboran Basin lavas from Hoernle *et al.* (1999), Turner *et al.* (1999) and Duggen *et al.* (2004); one Spanish lamproite sample from Turner *et al.* (1999); K/Ar age data for Algerian Si–K-rich and Si-poor igneous rocks from Louni-Hacini *et al.* (1995) and Coulon *et al.* (2002); the Messinian Salinity Crisis (5·96–5·33 Ma) from Krijgsman *et al.* (1999), which defines the Miocene–Pliocene boundary.

Pb/Ce) with decreasing age (Fig. 8a, f). The systematic temporal variations of both isotope and incompatible element ratios with very similar partition coefficients cannot be explained by differences in the degree of partial melting or by fractional crystallization, but instead must reflect crustal assimilation or binary mixing between different components from a heterogeneous mantle source.

Mantle source identification

As illustrated in the Sr–Nd–Pb-isotope diagrams (Fig. 7a–d), a number of distinct mantle and/or source components appear to play a role in the petrogenesis of the Si–K-rich and Si-poor groups: (1) lithospheric components such as the continental crust and subduction-modified lithospheric mantle (e.g. Enriched Mantle 2, EM2) having high $^{87}Sr/^{86}Sr$, $\Delta 7/4$ and $\Delta 8/4$, moderate $^{206}Pb/^{204}Pb$ ratios and generally low $^{143}Nd/^{144}Nd$ ratios, and (2) sub-lithospheric components such as young and old HIMU mantle with low $^{87}Sr/^{86}Sr$, high $^{143}Nd/^{144}Nd$ and moderate $^{206}Pb/^{204}Pb$ ratios combined with negative $\Delta 7/4$ (e.g. Canary Islands and Ahaggar) or high $^{206}Pb/^{204}Pb$ ratios combined with positive $\Delta 7/4$ (e.g. St. Helena) (Thirlwall, 1997). Below we explore the role of the continental crust, the subcontinental lithospheric mantle, sub-lithospheric mantle reservoirs and the possible depths of melting in the origin of Si–K-rich and Si-poor group magmas from the southeastern Iberian and northwestern African continental margins.

The Si–K-rich group from the southern Iberian margin (8·2–4·8 Ma)

The Si–K-rich volcanic rocks (lamproites) from the southeastern Iberian continental margin form a compositional continuum with cordierite–garnet-bearing lavas from southern Spain, which are thought to result from crustal anatexis of a metapelitic protolith (Fig. 4a–d) (Zeck, 1970; Munksgaard, 1984; Cesare *et al.*, 1997; Cesare & Maineri, 1999). The geochemical similarity of the Spanish low-MgO lamproites (some of which contain cordierite and garnet, e.g. the lamproitic rocks from Mazarron based on petrographic observations) and the cordierite–garnet-bearing lavas from Cerro Hoyazo suggests that the cordierite–garnet-bearing igneous rocks themselves may be highly crustally contaminated derivatives of mafic lamproitic melts rather than pure crustal anatexites. This is consistent with the results of geochemical modelling by Benito *et al.* (1999), who proposed a mantle-derived origin for the parental melts of the Cerro Hoyazo lavas. However, as inferred from the previously mentioned compositional continuum between high-MgO lamproites, low-MgO lamproites and cordierite–garnet-bearing lavas, the Si–K-rich, lamproitic lavas with MgO below 6–8 wt % appear to have apparently assimilated significant amounts of continental crust. Although the high-MgO lamproites (MgO >8 wt %) seem to be unaffected by crustal contamination, they have isotopic compositions very similar to crustal materials such as local continental crust and marine sediments (Figs 5a and 7a–d). High-MgO lamproites also show extreme enrichments of most incompatible elements (e.g. K_2O = 3·6–10·2 wt %) and have high Cr (740–1230 ppm) and Ni (100–340 ppm) contents (Fig. 5a and Table 2). These more mafic magmas appear, therefore, to represent primitive mantle melts, despite their crustal trace element and isotopic geochemical signatures. This suggests that they are derived from enriched subcontinental mantle lithosphere modified by fluids or melts probably released from subducted marine sediments, resulting in extremely high $^{87}Sr/^{86}Sr$ and low $^{143}Nd/^{144}Nd$ ratios as well as a large positive deviation from the NHRL (high positive $\Delta 7/4$ and $\Delta 8/4$) (Venturelli *et al.*, 1984, 1988; Nelson *et al.*, 1986; Benito *et al.*, 1999; Turner *et al.*, 1999).

Based on results from experimental studies, the primary Spanish lamproite melts are thought to originate from depths of about 30–50 km within the uppermost portion of the subcontinental mantle lithosphere (Foley, 1993), i.e. within the stability field of spinel lherzolite. Derivation of the southern Iberian primary Si–K-rich melts from a spinel lherzolite mantle source, even if it contains K-rich amphibole, is not, however, consistent with their high Dy/Yb ratios (Fig. 9a). High Dy/Yb ratios require residual garnet in the source of the magmas, which preferentially incorporates the HREE. Very low degrees of partial melting of a garnet– phlogopite lherzolite with K contents ranging from 3000 to 9000 ppm could explain the variation of K/Yb and Dy/Yb (Fig. 9a). According to Foley, however, petrogenetic models for lamproites based on partial melting of phlogopite- (and amphibole-) bearing lherzolitic or harzburgitic mantle sources belie a more complex melting history including phlogopite–amphibole-rich pyroxenitic veins and vein–melt–wall-rock interaction (Foley, 1992, 1993). Based on geochemical modelling, 1–30% partial melts from a vein having the composition $Orthopyroxene_{0.05}$–$Clinopyroxene_{0.20}$–$Garnet_{0.05}$–$Phlogopite_{0.40}$–$Amphibole_{0.25}$–$Apatite_{0.03}$–$Rutile_{0.02}$ [as estimated from the diagrams of Foley (1992)] ought to have relatively low Dy/Yb and high K/Yb ratios. The partial melting curve for such vein material plots far outside the diagram in Fig. 9a, as the modelled melts have extremely high K/Yb (130 000–140 000) combined with relatively low Dy/Yb ratios (1·30–1·35) (i.e. to the right of the legend box in Fig. 9a). The position of the modelled curve, however, is relatively robust to moderate changes in the orthopyroxene, clinopyroxene, phlogopite, amphibole and rutile contents in the vein but very sensitive to minor changes in the amount of garnet and apatite. For a wide range of 0–10% garnet and apatite contents, however, K/Yb and Dy/Yb ratios stay above 100 000 and below 2·5, respectively. Therefore vein melting alone seems to be inadequate to explain the high Dy/Yb ratios observed for the lamproites (2·8–3·8). Foley (1992) proposed an attractive model of interaction of vein melts with a garnet peridotite wall rock. Significant interaction of lamproitic vein melts with garnet lherzolite or melts therefrom could increase the Dy/Yb and lower the K/Yb ratios to the range observed in the lamproites. High Dy/Yb, however,

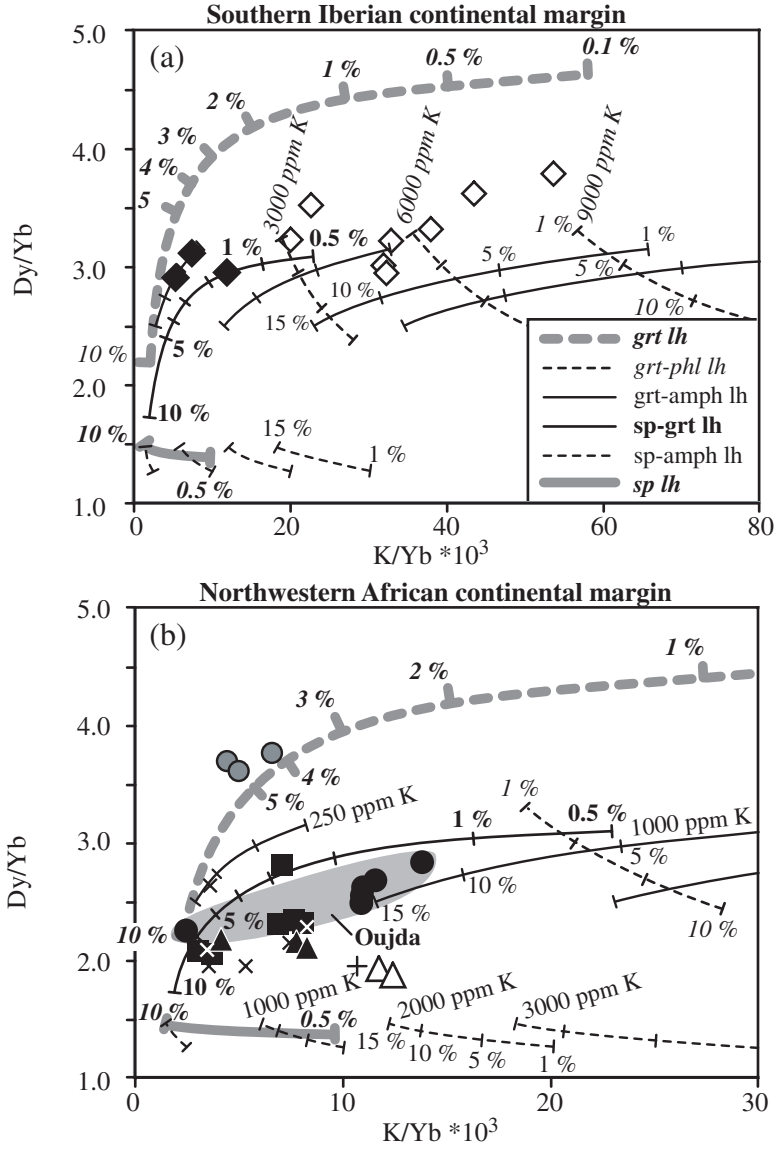

Fig. 9. K/Yb vs Dy/Yb diagrams illustrating geochemical modelling results and the geochemical composition of the more mafic post-collisional Si–K-rich and Si-poor igneous rocks from the southern Iberian and northwestern African continental margins (southern Iberian Si–K-rich lavas have >8 wt % MgO, Si-poor lavas >6 wt % MgO and northwestern African Si–K-rich igneous rocks have >4·5 wt % MgO and Si-poor lavas >6 wt % MgO). Symbols are as in Fig. 3. Non-modal, point-average fractional partial melting curves are presented for garnet lherzolite ($Olivine_{0·6}Orthopyroxene_{0·2}Clinopyroxene_{0·15}Garnet_{0·05}$), garnet-facies phlogopite lherzolite ($Ol_{0·564}Opx_{0·188}Cpx_{0·141}Grt_{0·047}Phl_{0·06}$), garnet-facies amphibole lherzolite ($Ol_{0·564}Opx_{0·188}Cpx_{0·141}Grt_{0·047}Amph_{0·06}$), spinel–garnet transition zone lherzolite ($Ol_{0·6}Opx_{0·27}Cpx_{0·08}Grt_{0·025}Sp_{0·025}$), spinel-facies amphibole lherzolite ($Ol_{0·56}Opx_{0·24}Cpx_{0·09}Sp_{0·05}Amph_{0·06}$) and spinel lherzolite ($Ol_{0·6}Opx_{0·25}Cpx_{0·1}Sp_{0·05}$). Percentages indicate degrees of partial melting. Normative weight fractions of minerals i in the partial melts are: $Ol_{0·05}Opx_{0·2}Cpx_{0·3}Grt_{0·45}$, $Ol_{0·17}Opx_{0·19}Cpx_{0·27}Grt_{0·02}Phl_{0·35}$, $Ol_{0·17}Opx_{0·19}Cpx_{0·27}Grt_{0·02}Amph_{0·35}$, $Ol_{0·05}Opx_{0·2}Cpx_{0·3}Grt_{0·25}Sp_{0·2}$, $Ol_{0·1}Opx_{0·27}Cpx_{0·5}Grt_{0·13}$ and $Ol_{0·17}Opx_{0·19}Cpx_{0·27}Sp_{0·02}Amph_{0·35}$. Mineral–melt distribution coefficients used for geochemical modelling are: $D^{K, Dy, Yb}_{olivine} = 0·00018, 0·007, 0·0015$; $D^{K, Dy, Yb}_{orthopyroxene} = 0·015, 0·022, 0·042$; $D^{K, Dy, Yb}_{clinopyroxene} = 0·02, 0·33, 0·28$; $D^{K, Dy, Yb}_{garnet} = 0·0007, 1·06, 4·01$; $D^{K, Dy, Yb}_{spinel} = 0·0045, 0·01, 0·01$; $D^{K, Dy, Yb}_{phlogopite} = 3·67, 0·029, 0·03$; $D^{K, Dy, Yb}_{amphibole} = 0·58, 0·78, 0·59$, respectively (these values were selected from the GERM website, at http://earthref.org/databases/). Source compositions: C1 chondritic REE composition (Dy 0·254 ppm and Yb 0·170 ppm) (Sun & McDonough, 1989) was chosen for all partial melting scenarios. For those excluding the K-bearing minerals amphibole and phlogopite, primitive mantle K contents of 250 ppm were assumed. The K content in the garnet-facies phlogopite lherzolite is controlled by the K content of the phlogopite, because of the high K concentrations in phlogopite (*c.* 94 000 ppm) as inferred from its chemical formula. Six per cent phlogopite in the source yields about 5600 ppm K. Three partial melting curves for garnet-facies phlogopite lherzolite have been modelled to show the influence of K variations in this source (for 3000, 6000 and 9000 ppm). K contents in amphibole-bearing (e.g. magnesio-richterite) lherzolite are highly variable (Deer *et al.*, 1996) and for modelling we considered K contents ranging from 250 ppm (corresponding to a K-free Na-magnesiorichterite), to 1000 ppm (corresponding to 6% $K_{0·175}$–$Na_{0·825}$magnesio-richterite in the source), 2000 ppm (6% of $K_{0·35}$–$Na_{0·65}$magnesiorichterite) and 3000 ppm (6% of $K_{0·53}$–$Na_{0·47}$ magnesiorichterite). Other data sources: Algerian Si–K-rich and Si-poor igneous rocks from Louni-Hacini *et al.* (1995) and Coulon *et al.* (2002).

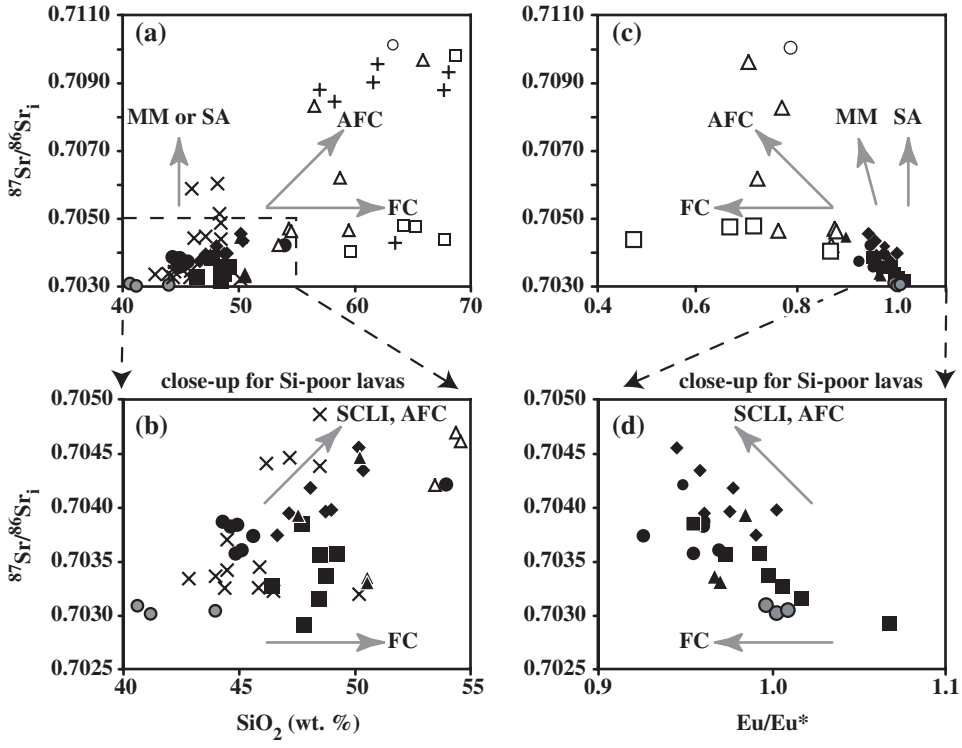

Fig. 10. $^{87}Sr/^{86}Sr_i$ vs SiO_2 wt % (a, b) and Eu/Eu* (c, d) diagrams illustrating the effects of combined assimilation and fractional crystallization (AFC), fractional crystallization (FC), interaction of sub-lithospheric melts with the subcontinental lithosphere (SCLI), mantle metasomatism (MM) and seawater alteration (SA) for post-collisional Si–K-rich and Si-poor igneous rocks from the southern Iberian and northwestern African continental margins. (b) and (d) are close-ups of (a) and (c), respectively, to highlight the compositional variations of the Si-poor group. Symbols are as in Fig. 3. Data sources: Algerian Si–K-rich and Si-poor igneous rocks from Louni-Hacini *et al.* (1995) and Coulon *et al.* (2002).

indicates interaction of lamproite melts with garnet lherzolite and thus an origin from within the garnet peridotite stability field at depths ≥70–80 km.

The Si-poor group from the southern Iberian margin (2·93–2·29 Ma)

Si-poor lavas from the Tallante volcanic field at the southeastern Iberian continental margin show correlations between Sr–Nd–Pb-isotope ratios and major and trace element concentrations and inter-element ratios. These correlations provide important information about the possible role of crustal and mantle components in their petrogenesis. $^{87}Sr/^{86}Sr$ correlates positively with SiO_2, Th, U, Pb, (Th, U)/Nb, Nb/La and Pb/Nd, and negatively with CaO, $^{143}Nd/^{144}Nd$ and $^{206}Pb/^{204}Pb$ (see examples in Figs 10 and 11). $^{143}Nd/^{144}Nd$ shows inverse correlations with U, Th, Pb, (U, Th)/Nb and Pb/Nb. $^{206}Pb/^{204}Pb$ displays inverse correlations with CaO, U/Nb and Pb/Nd (with $r^2 > 0{\cdot}7$). Whereas the most mafic samples are likely to reflect the composition of their mantle source, the more evolved samples are likely to provide information about the composition of assimilants during fractional crystallization (AFC). On this basis, it can be inferred that the contaminant has higher $^{87}Sr/^{86}Sr$, (Th, U)/Nb and Pb/Nd but lower $^{143}Nd/^{144}Nd$ and $^{206}Pb/^{204}Pb$ than the mafic Si-poor Tallante magmas and their mantle sources.

Such geochemical variations may result from interaction of primitive Si-poor Tallante magmas with the continental lithosphere, e.g. the continental crust or metasomatized subcontinental mantle. Volcanic rocks from the Tallante volcanic field frequently contain lower crustal xenoliths and mantle xenoliths (Vielzeuf, 1983; Dupuy *et al.*, 1986). Although the presence of crustal xenoliths indicates the possibility for assimilation of upper crustal material, the ubiquity of mantle xenoliths in the Tallante lavas argues for rapid magma ascent and against significant residence time in the continental crust, which would allow for AFC processes to occur. Therefore, the increase of $^{87}Sr/^{86}Sr$, (Th, U)/Nb and Pb/Nd coupled with a decrease of $^{143}Nd/^{144}Nd$ and $^{206}Pb/^{204}Pb$ in the Si-poor Tallante melts is most likely to reflect interaction with metasomatized sub-continental mantle lithosphere. Interaction with lamproitic melts derived from the lithospheric mantle serves as an alternative explanation. Interaction with metasomatized sub-continental mantle or melts therefrom is consistent with the

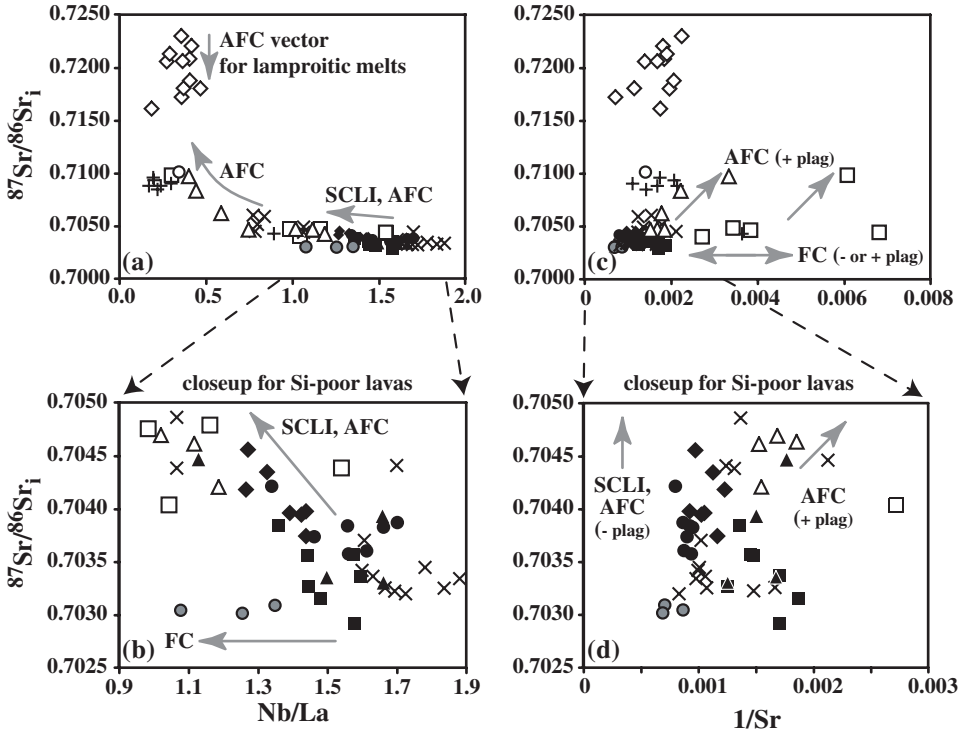

Fig. 11. Initial Sr-isotope ratios vs Nb/La (a, b) and 1/Sr (c, d) to illustrate the effects of combined assimilation and fractional crystallization (AFC), fractional crystallization (FC) and interaction of sub-lithospheric melts with the subcontinental lithosphere (SCLI) for post-collisional Si–K-rich and Si-poor igneous rocks from the southern Iberian and northwestern African continental margins. (b) and (d) are close-ups from (a) and (c), respectively, to highlight the compositional variations of the Si-poor group. Symbols are as in Fig. 3. Data sources: Algerian Si–K-rich and Si-poor igneous rocks from Louni-Hacini *et al.* (1995) and Coulon *et al.* (2002).

occurrence of phlogopite in the mantle xenoliths found in the Tallante lavas (Dupuy *et al.*, 1986; Capedri *et al.*, 1989). As Si–K-rich lamproitic melts both have higher $^{87}Sr/^{86}Sr$ and SiO_2, and lower CaO contents than the Si-poor Tallante magmas (Table 2) (Venturelli *et al.*, 1988; Benito *et al.*, 1999; Turner *et al.*, 1999), interaction with lamproitic melts could also partly explain: (1) the observed decrease in CaO and increase in SiO_2 coupled with increasing $^{87}Sr/^{86}Sr$; (2) their potentially high $\Delta 7/4$ and $\Delta 8/4$ well above the NHRL (Fig. 7b); (3) the hybrid geochemical characteristics between intraplate-type and subduction-related geochemical signatures in multi-element diagrams (e.g. positive Th–U anomalies, variable Nb, Ta, K and Pb anomalies) (Fig. 5b). However, the geochemical similarity to lavas from intraplate volcanic areas such as the Canary Islands in terms of major and most trace elements and Sr–Nd-isotope ratios points to derivation of the primary Si-poor melts from sub-lithospheric mantle sources and has already been pointed out in the literature (Wilson & Bianchini, 1999; López-Ruiz *et al.*, 2002; Duggen *et al.*, 2003).

The FeO and SiO_2 contents of mafic partial melts in intraplate volcanic settings can vary as a function of melting depths (Hirose & Kushiro, 1993). As illustrated in Fig. 12a, the FeO and SiO_2 contents of the more mafic Tallante lavas combined with experimental data for partial melting of dry peridotite at high pressures (Hirose & Kushiro, 1993) point to a derivation from a peridotitic source (Mg-number between 85 and 89) at depths between *c.* 40 and 80 km, i.e. presumably primarily within the spinel stability field. It should be emphasized that neither SiO_2 nor FeO in the mafic Si-poor, Na-rich Tallante lavas (MgO >6 wt %) correlates with MgO. Therefore the variations in SiO_2 and FeO observed for the mafic Tallante lavas are unlikely to result from fractional crystallization of magnesian phenocrysts and thus more probably reflect mantle processes such as partial melting and/or mixing with high-Si–K, low-Fe lamproitic melts. However, the moderately high Dy/Yb ratios at around three in the most mafic Si-poor Tallante lavas (>6 wt % MgO) require the presence of residual garnet in the source of the Tallante melts.

In the K/Yb vs Dy/Yb diagram (Fig. 9a), the Si-poor samples from Tallante plot close to partial melting curves modelled for three different scenarios: (1) partial melting of a garnet lherzolite source; (2) a spinel–garnet lherzolite source; (3) a garnet-facies amphibole lherzolite source with low K contents (250 ppm, i.e. a Na-rich rather than a K-rich amphibole). Garnet in peridotite is stable at depths >70–80 km, which is the approximate depth for

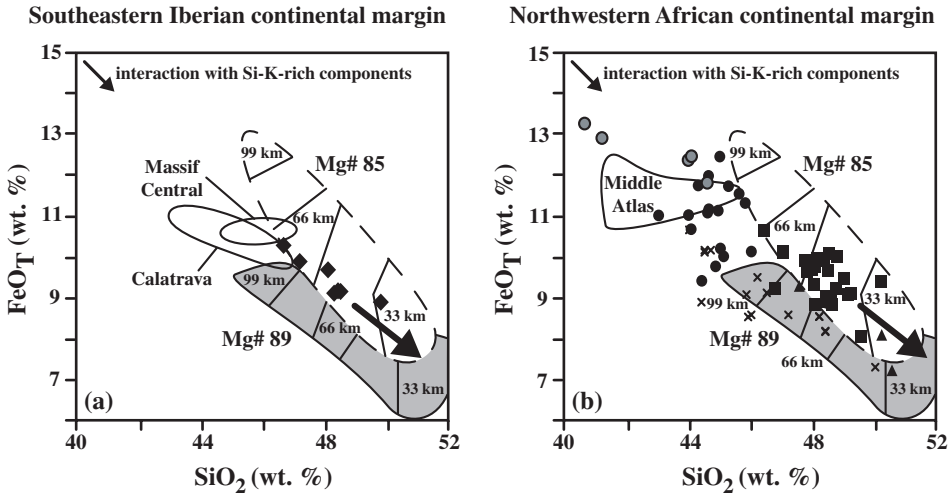

Fig. 12. SiO_2 wt % vs FeO_T wt % showing mafic, post-collisional Si-poor lavas (MgO >6 wt %) from the southern Iberian (a) and northwestern African (b) continental margins and experimental results for partial melting of dry peridotite with different fertility (Mg-number 85 and 89) at high pressures (Hirose & Kushiro, 1993). Symbols are as in Fig. 3. Data sources: mafic intraplate-type lavas from the Massif Central, France, from Wilson & Downes (1991); Calatrava, Central Spain, from Cebriá & López-Ruiz (1995); the Middle Atlas, Central Morocco, from Duggen *et al.* (unpublished data).

the spinel–garnet transition zone in the upper mantle. Amphibole is unstable at depths exceeding 70–100 km (Green, 1973; Wyllie & Wolf, 1993) and therefore garnet-facies amphibole peridotite can exist only in a narrow zone roughly between 70 and 100 km depth, probably within the mechanical boundary layer of the subcontinental lithosphere (Pearce *et al.*, 1990). Because the subcontinental lithosphere beneath southeastern Iberia at this depth appears to be highly metasomatized, providing the source for the Si–K-rich lamproitic melts, it seems unlikely that garnet-facies amphibole lherzolite constitutes the source of the Si-poor Tallante melts. This is consistent with their geochemical signature, pointing to derivation from a sub-lithospheric mantle source (Figs 5b and 7a–d). Alternatively, the Si-poor Tallante melts could have been formed through partial melting of an amphibole-free source: the mafic Tallante lavas plot close to the model curves for 6–8% partial melting of a garnet lherzolite and 1–2% partial melting of lherzolite containing both spinel and garnet. Melting in the spinel–garnet transition zone is able to explain slightly elevated K/Yb as observed for one Tallante sample without involving K-bearing phases in the mantle source. Melting of a garnet lherzolite, however, requires an additional process that is capable of enhancing K/Yb, such as, for example, interaction of Si-poor magmas with K-rich, metasomatized mantle lithosphere or lamproitic melts derived from such lithosphere. Interaction with MgO-rich lamproitic melt components may also explain why both SiO_2 and K/Yb correlate positively with MgO in the three most mafic lavas with MgO between 7·7 and 8·5 wt %, which is the opposite of what is expected for fractional crystallization combined with crustal assimilation; lamproitic melts have higher SiO_2, higher K/Yb (and lower FeO) than the Tallante lavas (Figs 3 and 9a, and Table 2).

In conclusion, the Si-poor Tallante lavas from the southeastern Iberian continental margin probably represent low-degree partial melts of garnet-bearing sub-lithospheric mantle material such as garnet lherzolite or lherzolite from the garnet–spinel transition zone at depths ≥70–80 km. Variable interaction of these Si-poor melts with Si–K-rich components or melts from the metasomatized subcontinental mantle lithosphere is interpreted to have partially modified the intraplate geochemical fingerprint of the sub-lithospheric melts towards subduction-related signatures. How sub-lithospheric mantle material may undergo partial melting at depths between *c.* 70 and 100 km to form the Si-poor Tallante lavas in an area in which the normal sub-continental lithosphere thickness is *c.* 150 km will be addressed subsequently in the discussion of the geodynamic evolution of this region.

The Si–K-rich group from the northwestern African margin (7·58–4·82 Ma)

Si–K-rich igneous rocks from Gourougou and Guilliz show linear correlations between radiogenic isotope ratios and major and trace elements. $^{87}Sr/^{86}Sr$ correlates positively with La and Nd (Gourougou) and negatively with Na_2O (Guilliz), $^{143}Nd/^{144}Nd$ increases with increasing Sr (Gourougou and Guilliz) and CaO (Guilliz) and $^{206}Pb/^{204}Pb$ correlates positively with Na_2O (Guilliz) (with $r^2 > 0·7$). Hyperbolic correlations exist between

Sr-isotope ratios and incompatible trace element ratios such as U/Nb and Nb/La (Fig. 11a). Such correlations, in which several samples achieve elevated $^{87}Sr/^{86}Sr$ up to 0·710, indicate that AFC processes affected the geochemical composition of some Si–K-rich magmas in the Gourougou and Guilliz stratovolcanic complexes. As illustrated in the SiO_2 and 1/Sr vs $^{87}Sr/^{86}Sr$ diagrams (Figs 10a and 11c), three Gourougou igneous rocks, one Guilliz sample and the most Si–K-rich igneous rocks from the Oujda–Algeria area have elevated $^{87}Sr/^{86}Sr$ coupled with high SiO_2 and 1/Sr (Coulon *et al.*, 2002). However, several Si–K-rich samples from Gourougou and Guilliz (and one Si–K-rich sample from the Oujda–Algeria area) have low Sr-isotope ratios despite a significant variation in SiO_2 and Sr contents, which argues against significant crustal contamination. The Sr and Nd isotopic composition of the Si–K-rich igneous rocks from Gourougou and Guilliz with low Sr-isotope ratios overlaps the field for the Si-poor lavas from the same area despite different Pb isotopic compositions. This is not consistent with a co-genetic derivation of the Si–K-rich lavas from the Si-poor ones by AFC (Fig. 11) and, therefore, we infer that the primary magmas of the Si–K-rich and Si-poor volcanic rocks at the northwestern African continental margin were derived from different mantle sources. Major and trace element and Sr–Nd–Pb radiogenic isotope ratios of the Si–K-rich igneous rocks, therefore, suggest derivation from a K-enriched, metasomatized mantle source with a subduction-related geochemical signature, possibly inherited from an older subduction zone. Because of its vicinity to the Alboran Basin (Fig. 1), the source of the Gourougou magmas may also have been affected by hydrous fluids and melts from the Miocene Alboran subduction zone (Hoernle *et al.*, 1999; Duggen *et al.*, 2004; Gill *et al.*, 2004).

The K/Yb vs Dy/Yb diagram in Fig. 9b provides constraints on the depths of melting for the Si–K-rich Gourougou magmas. Two of the more mafic Gourougou samples with MgO > 4 wt % and low $^{87}Sr/^{86}Sr$ are plotted. The Guilliz Si–K-rich trachyandesites are not included in Fig. 9b because of uncertainties arising from their evolved nature such as fractionation of REE through fractional crystallization of apatite, which is evident from a negative correlation of SiO_2 and P_2O_5 ($r^2 = 0·9$) for Si–K-rich samples with >57 wt % silica. The more mafic Si–K-rich Gourougou lavas (SiO_2 <55·5 wt %) (and one mafic Si–K-rich sample from Algeria) have Dy/Yb ratios slightly below two and elevated K/Yb ratios. Elevated Dy/Yb ratios require residual garnet in the source of the melts but they are too low to result from partial melting of garnet lherzolite alone (Fig. 9b). Different scenarios can be considered: (1) mixing between 1–10% partial melt of a garnet-facies phlogopite lherzolite with 0·5–10% partial melt of a spinel lherzolite *or* 1–15% melt from a spinel-facies amphibole lherzolite; (2) mixing of 1–15% garnet-facies amphibole lherzolite melts with spinel lherzolite melts *or* spinel-facies amphibole lherzolite melts; or (3) mixing of garnet lherzolite melts or spinel–garnet transition zone melts with spinel-facies amphibole lherzolite melts. Each scenario requires residual garnet in the source region and the presence of K-bearing phases. A plausible explanation would be a melting column with the lower end located in the upper garnet-stability field and the upper end situated in the spinel lherzolite field. In conclusion, Si–K-rich melts from the northwestern African continental margin were probably derived from a K-enriched, metasomatized mantle source from depths between 50 and 100 km, i.e within the mechanical boundary layer of the subcontinental lithosphere. K enrichment may have been associated either with fluids or hydrous melts introduced from the adjacent Miocene subduction zone in the Alboran Basin (e.g. Gourougou) or with an earlier subduction event (e.g. Guilliz) or both.

The Si-poor group from the northwestern African margin (6·25–0·65 Ma)

Several samples from the Si-poor group from the northwestern African continental margin plot significantly below the NHRL and therefore have negative Δ7/4 values up to −7·7 (e.g. igneous rocks from Plateau du Rekkam, the Oujda volcanic field except for one sample, and one sample from Guilliz) (Fig. 7b). On the African plate, basaltic lavas plotting on or below the NHRL can be found in the adjacent intraplate volcanic areas of the Canary Island Archipelago (eastern North Atlantic) and Ahaggar (southern Algeria); these have geochemical characteristics suggesting derivation from sub-lithospheric mantle sources (Allègre *et al.*, 1981; Hoernle & Schmincke, 1993*a*, 1993*b*). It is very unlikely that lavas with negative Δ7/4 values have been significantly affected by continental crustal contamination, as the continental crust plots well above the NHRL and has a high Pb content (Taylor & McLennan, 1985; Thirlwall, 1997). Therefore, such lavas provide direct geochemical information about their mantle sources, in terms of radiogenic isotope ratios and ratios of elements having very similar partition coefficients during partial melting and fractional crystallization in basaltic melts (e.g. the pairs U–Nb, K–La and Pb–Nd). It can, thus, be inferred that the source of the Si-poor melts with negative Δ7/4 had low $^{87}Sr/^{86}Sr$ <0·7039, high $^{143}Nd/^{144}Nd$ >0·5127, $^{206}Pb/^{204}Pb$ ranging from 19·3 to 20·8, and U/Nb = 0·0172–0·0230, K/La = 80·2–411·1 and Pb/Nd = 0·0326–0·0751. In terms of Sr–Nd-isotope and inter-element ratios this source is very similar to that of lavas from the Canary Islands derived from sub-lithospheric mantle sources but it tends to have higher $^{206}Pb/^{204}Pb$ ratios (e.g. Gran Canaria

$^{87}Sr/^{86}Sr$ <0·7034, $^{143}Nd/^{144}Nd$ >0·5128, $^{206}Pb/^{204}Pb$ = 19·5–20·0, U/Nb = 0·0146–0·0229, K/La = 98·8–418·7, Pb/Nd = 0·0369–0·0557) (Hoernle *et al.*, 1991; Thirlwall, 1997). Interestingly, both Oujda and Plateau du Rekkam volcanic rocks with negative Δ7/4 yield regression lines subparallel to the Ahaggar array in the uranogenic Pb-isotope diagram (Fig. 7b). If interpreted as Pb–Pb isochrons, these regression lines correspond to *c.* 840 Ma and 975 Ma ages, respectively. Similar Pb–Pb isochron ages were found for the neighbouring Madeira hot spot system in the eastern North Atlantic and were interpreted to reflect short-term recycling of oceanic lithosphere in the Earth's mantle (Geldmacher & Hoernle, 2000; Geldmacher *et al.*, 2000). Many Oujda lavas, however, also plot close to the low-velocity component (LVC) (Fig. 7b–d), which is observed in intraplate-type lavas from Central and Western Europe, the Central Mediterranean and the Eastern North Atlantic (Hoernle *et al.*, 1995). This suggests that most Si-poor igneous rocks from the Oujda–Algeria area were derived from a sub-lithospheric mantle source with plume-like characteristics.

The Si-poor igneous rocks from the Gourougou and Guilliz volcanic fields extend from the NHRL on Pb isotope diagrams to the field for Si–K-rich rocks with high Δ7/4 values (e.g. Fig. 7b). For Si-poor Gourougou lavas Δ7/4 correlates negatively with Nb/Zr ($r^2 = 0·92$) and Nb/Yb ($r^2 = 0·85$), whereas for the Si-poor Guilliz samples $^{87}Sr/^{86}Sr$ correlates negatively with Eu anomaly (Eu/Eu* ranging from 1·07–0·95, $r^2 = 0·92$) (Fig. 10d). These correlations provide information about the high Δ7/4 end-member or contaminant of the sublithospheric melts, which has $^{87}Sr/^{86}Sr$ >0·7045, $^{143}Nd/^{144}Nd$ <0·5127, Δ7/4 >8·6, Δ8/4 >44, which can also be inferred from the Sr–Nd–Pb isotope diagrams (Fig. 7a–d). Components with such a geochemical fingerprint can be found in the continental crust or metasomatized subcontinental mantle lithosphere or melts therefrom, for example, the Si–K-rich melts in the Gourougou and Guilliz volcanic centres (Figs 7, 10 and 11). As no clear correlations exist between MgO or SiO_2 with Nb/Zr, Nb/Yb, Eu anomaly or Sr–Nd–Pb-isotope ratios, it seems unlikely that fractional crystallization of magnesian phenocryst phases was associated with an increase of $^{87}Sr/^{86}Sr$, Δ7/4 and Δ8/4 and a decrease of $^{143}Nd/^{144}Nd$, Nb/Zr and Nb/Yb. These observations argue against significant crustal contamination of the Si-poor Gourougou and Guilliz magmas by AFC requiring significant fractional crystallization. Instead, the geochemical systematics point to an interaction of the Si-poor melts with the metasomatized subcontinental mantle lithosphere or melts therefrom. Unfortunately, AFC cannot conclusively be excluded for some of the samples having elevated Δ7/4 and Δ8/4. However, the aforementioned geochemical correlations and the composition of the more mafic samples (MgO >6–8 wt %) provide information about the composition of the mantle source of the primary Si-poor magmas. It can be inferred that the source of the Si-poor Gourougou lavas had $^{87}Sr/^{86}Sr$ <0·7033, $^{143}Nd/^{144}Nd$ <0·5130, Δ7/4 <4·3 and Δ8/4 <9·0, and that of the Guilliz melts had $^{87}Sr/^{86}Sr$ <0·7029, $^{143}Nd/^{144}Nd$ <0·5130, negative Δ7/4 and Δ8/4 < −2·2. This isotopic composition along with the intraplate-type multi-element patterns (Figs 6b, d, f, and 7a–d) is consistent with derivation of the primary Si-poor Gourougou and Guilliz lavas from a sub-lithospheric mantle source. As can be inferred from the uranogenic Pb-isotope diagram (Fig. 7b), this source was probably contaminated by plume material having a young-HIMU geochemical fingerprint similar to that of the Canary Islands (Hoernle & Tilton, 1991; Hoernle *et al.*, 1991; Thirlwall, 1997).

The major and trace element compositions of the mafic Si-poor igneous rocks from the northwestern African continental margin can provide information about the melting regime of their mantle source. As indicated by the SiO_2 vs FeO diagram in Fig. 12b, Si-poor melts from the Plateau du Rekkam volcanic field could have been generated by partial melting of a peridotite with decreased fertility at depths exceeding 100 km, i.e. outside the amphibole stability field. Many Oujda samples plot at the end of the experimental field for the melting of a peridotite with Mg-number of ∼89, consistent with derivation from depths exceeding 100 km. Several Oujda samples, however, lie close to the experimental field for partial melts of a more fertile peridotite with Mg-number = 85, pointing to derivation at depths exceeding 70–80 km depth from a more fertile source. In contrast, most of the Si-poor lavas from Algeria have SiO_2 and FeO contents pointing to magma generation at shallower depths (*c.* 40–100 km) than the Plateau du Rekkam and Oujda lavas. These estimates are consistent with geochemical modelling results in the K/Yb vs Dy/Yb diagram in Fig. 9b. Lavas from the Plateau du Rekkam area have very high Dy/Yb ratios (>3·5) combined with low K/Yb ratios and therefore plot very close to a garnet lherzolite partial melting curve (4–5% partial melting). Very high Dy/Yb and relatively low K/Yb argue for the absence of spinel, phlogopite and K-bearing amphibole in the source of Plateau du Rekkam lavas. The situation is slightly different for the remaining samples from the Oujda–Algeria area. They have high Dy/Yb but show a large variation in K/Yb ratios. The Oujda–Algeria lavas therefore plot close to the garnet lherzolite, the garnet-facies amphibole lherzolite and the spinel–garnet transition zone model partial melting curves. Several Oujda samples with elevated K/Yb, shown in Fig. 9b, plot close to the high-pressure tip of the experimental field for partial melting of a peridotite with Mg-number = 89 indicating derivation from >100 km,

i.e. outside the stability fields for amphibole and spinel. Those Oujda lavas plotting close to the Mg-number = 85 field could have been derived from 70–100 km depths where spinel and amphibole may have been stable. However, the mafic samples from Oujda do not plot along one of the partial melting curves. Instead, they define an array with a positive correlation of K/Yb with Dy/Yb, which suggests binary mixing of two melt end-members (Fig. 9b). Therefore, a more plausible model to explain the composition of the Si-poor lavas from the Oujda volcanic field is mixing of low-degree (<1%) partial melts from a garnet lherzolite source with moderate-degree (5–10%) partial melts from the spinel–garnet transition zone.

The Si-poor Gourougou and Guilliz magmas were apparently generated from a more fertile peridotite source than the Si-poor lavas from the Oujda–Algeria area. As neither SiO_2 nor FeO correlates with MgO for the mafic Si-poor Gourougou and Guilliz samples, elevated SiO_2 and lowered FeO are unlikely to result from fractional crystallization. Therefore, SiO_2 and FeO contents indicate shallower depths of melting on the order of 40–80 km. The Dy/Yb ratios of mafic Gourougou and Guilliz lavas are relatively high (>2·0) and, therefore, require the involvement of melts from the garnet stability field. One mafic Guilliz sample (GZ160699-5, MgO 11·2 wt %) has higher Dy/Yb ratios than the other samples in Fig. 9b and also has the lowest SiO_2 (46·4 wt %) and the highest FeO content (10·7 wt %) of the mafic samples shown in Fig. 12b, which is consistent with a derivation from the spinel–garnet transition zone at 70–80 km depth. The other Guilliz samples plot below the spinel–garnet transition zone partial melting curve in Fig. 9b. Their higher SiO_2 and lower FeO contents are not consistent with a significant melt component from a garnet lherzolite source (≥80 km) and point to involvement of a spinel lherzolite source (Fig. 12b). Therefore we propose derivation by mixing of low- to moderate-degree partial melts from the spinel–garnet transition zone with low- to moderate-degree partial melts from a spinel lherzolite (Fig. 9b). Interaction of Si-poor Guilliz melts with Si–K-rich material in the metasomatized subcontinental mantle lithosphere may also be involved, and could result in a decrease of Dy/Yb, FeO and increase of K/Yb and SiO_2. Such a process is more clearly indicated for the mafic Si-poor melts from Gourougou as they form an array with their mafic Si–K-rich associates in Fig. 9b. Relatively low FeO contents and elevated SiO_2 and K/Yb in the mafic Si-poor Gourougou melts may result from interaction with Si–K-rich melts in the subcontinental lithosphere (Figs 9b and 12); lavas with the lowest K/Yb would be derived from the deepest sources in this scenario. Taking into account both K/Yb and Dy/Yb ratios and SiO_2 and FeO contents, we infer that the Si-poor Gourougou melts were derived by low to moderate degrees of partial melting in the garnet–spinel transition zone at *c.* 70–80 km depth, and mixed with partial melts (Si–K-rich) from the (amphibole-bearing) spinel lherzolite field in the subcontinental lithosphere.

Summary of the inferred mantle sources and the partial melting regime

Based on major and trace element and Sr–Nd–Pb-isotope ratios, the mantle sources of Upper Miocene to Lower Pliocene Si–K-rich igneous rocks from the Iberian and African continental margins appear to have been modified by Miocene or more ancient subduction events. The mafic Si–K-rich igneous rocks require garnet and K-bearing phases such as phlogopite and/or amphibole in their mantle source, which are different for the Iberian and African Si–K-rich rocks. The Spanish lamproites are inferred to have been generated by interaction of melts from phlogopite–amphibole–pyroxene–garnet veins with garnet peridotite wall-rock (Foley, 1993) and were generated deeper than 70 km based on the geochemical modelling results in this study. For the Si–K-rich rocks from the northwestern African margin, partial melting probably involved a melting column ranging from uppermost garnet lherzolite to well within the spinel lherzolite stability field, i.e. from depths between 50 and 100 km. K-bearing phases such as phlogopite or amphibole could have been stable within the full range of the melting column. The mantle sources of the Si–K-rich igneous rocks from the Iberian and African continental margins, however, were probably located in the mechanical boundary layer of the subcontinental lithosphere.

Based on intraplate-like geochemical signatures, the Late Miocene to Pleistocene mafic Si-poor igneous rocks were probably derived from sub-lithospheric mantle sources contaminated with mantle plume material such as young HIMU mantle (Thirlwall, 1997) or the low-velocity component (LVC; Hoernle *et al.*, 1995). Mafic Si-poor melts with negative Δ7/4 (e.g. lavas from the Oujda–Algeria area and Guilliz) have probably not interacted with the continental lithosphere. Si-poor melts with positive Δ7/4 (e.g. lavas from southeastern Spain, Gourougou and Guilliz) show interaction with components in, or melts from, the metasomatized subcontinental lithospheric mantle. Depths of partial melting range from >100 km (garnet lherzolite stability-field) to about 40 km (spinel lherzolite stability-field). Partial melting and generation of Si-poor melts in several volcanic areas obviously involved melting columns ranging from garnet- to spinel-facies depths.

In summary, the depths of partial melting of the younger Si-poor melts (*c.* 40 to >100 km) overlap with the depths inferred for the spatially associated but generally older Si–K-rich igneous rocks (*c.* 50–100 km) despite fundamental differences in their major and trace element and Sr–Nd–Pb-isotope compositions. A discussion of the

westernmost Mediterranean geodynamic evolution may help to solve the puzzle of why two fundamentally different mantle sources existed at the same depths but at different times.

GEODYNAMIC EVOLUTION

The geochemical transition from subduction-related to intraplate-type geochemical signatures in mantle-derived rocks strongly points to major changes in mantle geometry beneath the westernmost Mediterranean close to the Miocene–Pliocene boundary (El Bakkali *et al.*, 1998; Hoernle *et al.*, 1999; Coulon *et al.*, 2002; Duggen *et al.*, 2003). These large-scale mantle processes were associated with large-scale uplift and closure of marine gateways connecting the Mediterranean Sea with the Atlantic Ocean, which resulted in the isolation and desiccation of the Mediterranean Sea and major faunal changes that define the Miocene–Pliocene boundary (Hsü *et al.*, 1973; Duggen *et al.*, 2003). Several mantle sources with fundamentally distinct geochemical compositions were partially melted in the course of the large-scale reorganization of the western Mediterranean upper mantle: (1) a shallow mantle wedge (consisting of depleted asthenosphere and attenuated continental lithospheric mantle) enriched by fluids or melts from subducted oceanic lithosphere beneath the Alboran Basin in the Middle to Late Miocene (Hoernle *et al.*, 1999; Duggen *et al.*, 2004; Gill *et al.*, 2004); (2) metasomatically enriched subcontinental mantle lithosphere beneath the southeastern Iberian and northwestern African continental margins modified by fluids or melts from the adjacent Miocene Alboran Basin subduction zone or an older subduction event; (3) plume-contaminated, ambient sub-lithospheric mantle upwelling beneath the continental margins of southeastern Iberia and northwestern Africa. Below we explore the possible role of these mantle reservoirs in the Miocene to Quaternary geodynamic evolution of the westernmost Mediterranean by integrating geochronological, geochemical, geological and geophysical data.

The Alboran Basin

Several models have been proposed for the formation of the Alboran Basin that invoke (1) subduction of oceanic lithosphere (Royden, 1993; Lonergan & White, 1997; Hoernle *et al.*, 1999; Gutscher *et al.*, 2002; Duggen *et al.*, 2003, 2004; Gill *et al.*, 2004); (2) detachment of near-vertical subducted oceanic lithosphere (Blanco & Spakman, 1993; Zeck, 1996, 1999; Hoernle *et al.*, 1999); (3) detachment or delamination of subcontinental mantle lithosphere (Docherty & Banda, 1995; Comas *et al.*, 1999; Turner *et al.*, 1999; Calvert *et al.*, 2000; López-Ruiz *et al.*, 2002; Platt *et al.*, 2003). Subduction of oceanic lithosphere and detachment or delamination of subcontinental lithosphere should produce volcanism with characteristic geochemical compositions. Therefore, we can use the geochemistry of the Alboran Basin volcanism to distinguish between these fundamentally different tectonic processes for the formation of the Alboran 'Mediterranean-style back-arc basin' (Horvath & Berckhemer, 1982).

Volcanic rocks from the Alboran Basin (Fig. 1) belong to the low-K (tholeiitic) and medium- to high-K (calc-alkaline) series with major and trace element and O–Sr–Nd–Pb-isotopic compositions very similar to those of volcanic front and rear-arc lavas found in active subduction zones (e.g. Izu–Bonin) (Hoernle *et al.*, 1999; Duggen *et al.*, 2004; Gill *et al.*, 2004). Their geochemical characteristics provide evidence for magma generation involving high degrees of partial melting of depleted (harzburgitic) upper mantle material triggered by hydrous fluids and melts released from subducted oceanic lithosphere in the Middle to Late Miocene (*c.* 12–6 Ma) (Hoernle *et al.*, 1999; Duggen *et al.*, 2004). This is consistent with the boninitic affinity of mafic lavas from Alboran Island and the Alboran sea floor (Hoernle *et al.*, 1999; Gill *et al.*, 2004). The geochemical characteristics of the Alboran Basin lavas such as mantle-like $\delta^{18}O$ as low as 5·3‰ (Duggen *et al.*, 2003, 2004; Duggen *et al.* unpublished data) undoubtedly rule out an origin exclusively by anatexis of continental crust as proposed in the literature (Zeck *et al.*, 1998, 1999).

Detachment or delamination models advanced for the formation of the Alboran Basin are difficult to envisage for several reasons. Detachment of a near-vertical slab beneath the centre of the Alboran Basin in the Early Miocene following northward subduction of Tethys oceanic lithosphere under Iberia (Zeck, 1996) requires subduction prior to detachment and should involve typical subduction-zone volcanic activity before the slab detached. There is, however, no evidence for large-volume Late Oligocene–Early Miocene continental subduction-zone volcanism on the southern Iberian margin. Additionally, slab detachment should cause a rapid cessation of tholeiitic and calc-alkaline arc volcanism (Hoernle *et al.*, 1999). As volcanism with a clear subduction-related geochemical fingerprint was active between 12·1 and 6·1 Ma in the Alboran Basin (Hoernle *et al.*, 1999; Duggen *et al.*, 2004), slab detachment in the Early Miocene seems to be very unlikely.

Models involving detachment or delamination of subcontinental lithosphere beneath the Alboran Basin at the Oligocene–Miocene boundary are unable to explain a number of key geological, geochemical and geophysical observations in the westernmost Mediterranean. These are: (1) the oceanic subduction zone geochemical characteristics of Middle to Late Miocene Alboran Sea lavas (Hoernle *et al.*, 1999; Duggen *et al.*, 2004; Gill *et al.*, 2004); (2) the transition from thinned continental to Neogene oceanic crust in the easternmost Alboran Basin

(Dewey *et al.*, 1989; Comas *et al.*, 1999) (Fig. 1); (3) directed rather than radial Miocene crustal nappe emplacement onto the southern Iberian and northwestern African continental margins associated with vertical axis-rotations of crustal nappes anti-clockwise in the Betics and clockwise in the Rif mountains (Lonergan & White, 1997); (4) an east-dipping positive seismic anomaly beneath the Alboran Basin that shows westward continuity with the Atlantic oceanic lithosphere (Gutscher *et al.*, 2002; Gutscher *et al.*, 2003); (5) a concentration of seismicity along a north–south-directed line at 60–120 km depth (as is commonly observed within subducting slabs where the slab curvature rapidly increases) beneath the westernmost Alboran Basin (Gutscher *et al.*, 2002); (6) geophysical evidence for an active accretionary wedge due west of Gibraltar (Gutscher *et al.*, 2002). These important observations can convincingly be explained with westward slab roll-back and steepening of subducted, east-dipping oceanic Tethys lithosphere since the Oligocene (Lonergan & White, 1997; Wilson & Bianchini, 1999; Gutscher *et al.*, 2002; Duggen *et al.*, 2004). A slab roll-back model for the Alboran Basin fits well into the widely accepted view that the western and central Mediterranean geodynamic evolution was dominated by slab roll-back of old subducting Tethys oceanic lithosphere (Dewey *et al.*, 1989; Lonergan & White, 1997; Carminati *et al.*, 1998; Wilson & Bianchini, 1999; Jolivet & Faccenna, 2000; Wortel & Spakman, 2000; Gutscher *et al.*, 2002; Duggen *et al.*, 2004). However, below we argue that the situation for the continental margins of southern Iberia and northwestern Africa is different.

The southern Iberian and northwestern African continental margins

During the Late Miocene to Pleistocene, igneous activity along the southern Iberian and the Moroccan part of the northwestern African continental margin was marked by the occurrence of Si–K-rich igneous rocks (8·2–4·8 Ma) with subduction-like geochemical signatures and Si-poor lavas (6·3–0·65 Ma) with intraplate-type signatures (Figs 1 and 2). Available K/Ar age data indicate that the onset of both Si–K-rich and Si-poor igneous activity was earlier in Algeria than in Spain and Morocco (Louni-Hacini *et al.*, 1995; Coulon *et al.*, 2002) (Fig. 2). As inferred from the major and trace element data, geochemical modelling and interpretation of experimental partial melting of spinel and garnet peridotites presented above (e.g. Figs 9 and 12), the parental Si–K-rich and Si-poor magmas are considered to be derived by partial melting of geochemically different mantle sources that existed largely at similar depths in a given area—metasomatized, subcontinental lithosphere and plume-contaminated sublithospheric mantle. New Ar/Ar age data suggest that the transition from Si–K-rich to Si-poor magmatism at the continental margins of Iberia and Africa (Fig. 8) reflects the progressive replacement of subcontinental lithosphere by sub-lithospheric mantle.

We propose that delamination of subcontinental lithosphere occurred beneath the continental margins of southern Iberia and northwestern Africa. It could be argued that slab detachment was responsible for the transition from Si–K-rich, subduction-related to Si-poor, intraplate-type igneous activity. Any geodynamic model, however, has to explain why the transition from Si–K-rich to Si-poor magmatism occurred both along the southern Iberian and northwestern African continental margins. If slab detachment occurred in the Alboran region, then double slab detachment, following north- and south-directed subduction beneath the Iberian and African margins, is required. There is no evidence in the available geophysical data that indicates such a process. Finally, as mentioned above, slab detachment is not consistent with recent results from seismic tomography and the observed temporal and spatial geochemical variation of the westernmost Mediterranean volcanism.

Detachment of subcontinental lithosphere has been proposed before based on geochemical and geochronological data for igneous rocks from southern Spain, by Turner *et al.* (1999). Those workers extended their detachment model to the entire Alboran region including the Alboran Basin area. As discussed above, this model is not supported by geophysical evidence or by the geochemical composition of Miocene volcanic rocks from the Alboran Basin area. Instead, we propose that the removal of the sub-continental lithosphere beneath the continental margins of southern Iberia and northwestern Africa was progressive (delamination) rather than convective (detachment).

Both delamination and detachment of subcontinental lithosphere could be associated with the generation of Si–K-rich, subduction-related igneous rocks and Si-poor, intraplate-type lavas. Delamination of subcontinental lithosphere in conjunction with subduction of oceanic lithosphere has been proposed for the petrogenesis of the Neogene to Quaternary K-rich magmatism of central Italy (Serri *et al.*, 1993) and the association of Si–K-rich and Si-poor magmatism of the Andean Puna Altiplano Plateau (Kay & Mahlburg Kay, 1993). Detachment of subcontinental lithosphere following continental thickening is thought to be responsible for the generation of K-rich melts in the Tibetan Plateau (Turner *et al.*, 1996) and the calc-alkaline to K-rich igneous rocks of Eastern Anatolia (Turkey) (Pearce *et al.*, 1990). Based on mantle mineral stabilities, mantle solidi and geothermal gradients, Pearce *et al.* (1990) showed that continental thickening can also bring metasomatized subcontinental lithosphere to greater depths, causing partial melting.

Delamination of subcontinental mantle lithosphere beneath the continental margins of southern Iberia and

northwestern Africa is also consistent with geophysical data such as the location of earthquake hypocentres and seismic-wave velocities pointing to the presence of a thin wedge-shaped layer (*c.* 20–40 km) of (possibly hotter) asthenospheric material between the Moho and a slab of lithospheric mantle down-bending beneath southern Spain and northern Morocco near Gibraltar in the western part of the Alboran Basin (Seber *et al.*, 1996*b*). This process can explain why Si-poor, intraplate-type magmas were formed at largely similar depths in the same areas where Si–K-rich magmatism had ceased, as the upwelling sub-lithospheric mantle that replaced the delaminating subcontinental lithosphere at a given depth was probably the source for the primary Si-poor magmas. Such sub-lithospheric mantle could either be depleted convecting asthenosphere capable of producing MORB melts at sufficiently high degrees of melting or enriched mantle plume material. The major and trace element and Sr–Nd–Pb-isotope composition of most of the Si-poor lavas is consistent with derivation from a HIMU-type mantle source rather than depleted MORB-source mantle (Fig. 7b–d). The HIMU-type mantle could be plume material or could reflect concentrations of pyroxenitic and eclogitic material within the upper mantle. A few Si-poor samples, however, have $^{87}Sr/^{86}Sr$, $^{143}Nd/^{144}Nd$ and $^{206}Pb/^{204}Pb$ similar to enriched MORB that might indicate a marginal involvement of a depleted MORB mantle (DMM) component (Fig. 7c and d), which, however, does not seem to be supported by the Pb isotope data (Fig. 7b). An overlap with enriched MORB composition in the $^{206}Pb/^{204}Pb$ vs $^{87}Sr/^{86}Sr$ and $^{143}Nd/^{144}Nd$ diagrams is more likely to result from interaction of sub-lithospheric melts with the subcontinental mantle or melts derived therefrom (indicated by arrow 2 in Fig. 7c and d). Involvement of a MORB source therefore appears to be unnecessary.

Low magma volumes and the absence of an age progression in the western Mediterranean Si-poor rocks (Fig. 1) and lack of evidence from seismic tomography for low-velocity cylindrical structures beneath the Alboran region (Seber *et al.*, 1996*b*; Calvert *et al.*, 2000; Gutscher *et al.*, 2002) makes derivation of the Si-poor lavas directly from mantle plumes such as found below the Canary Islands unlikely. The similarity in geochemistry of the western Mediterranean Si-poor group lavas with intraplate-type volcanic rocks from Central Europe, the eastern North Atlantic and NW Africa provides evidence for derivation from a common source beneath these regions (Allègre *et al.*, 1981; Hoernle *et al.*, 1991, 1995; Wilson & Downes, 1991; Hoernle & Schmincke, 1993*a*, 1993*b*; Granet *et al.*, 1995; Thirlwall, 1997; Geldmacher & Hoernle, 2000). Global seismic tomography data suggest that a large low-velocity structure extends from >2000 km depth to the base of the upper mantle (*c.* 660 km) and spreads out in the upper mantle beneath Europe and the Mediterranean (Hoernle *et al.*, 1995; Goes *et al.*, 1999) thereby probably contaminating the convecting asthenosphere with plume material. Subduction of oceanic lithosphere may trigger sub-lithospheric mantle material to well up around slab 'graveyards' localized at the base of the upper mantle or slab structures present in the upper mantle (Goes *et al.*, 1999). We propose that further upwelling of such plume-contaminated, sub-lithospheric mantle material may be triggered by delaminating or detaching subcontinental mantle lithosphere. Melting of upwelling plume-contaminated asthenosphere replacing delaminated subcontinental lithosphere can explain the occurrence of Si-poor lavas on the continental margins of southern Iberia and northwestern Africa.

Reconciling the Miocene to Pliocene geodynamic evolution of the Alboran Basin with that of the continental margins of southern Iberia and northwestern Africa

In Figure 13, we present a three-dimensional geodynamic model that illustrates the connection between the changes in mantle geometry beneath the westernmost Mediterranean area and the transition from subduction-related to intraplate-type magmatism occurring at the Miocene–Pliocene boundary. As the Alboran Block was forced to move to the SW in the Miocene it overrode subducting east-dipping Tethys oceanic lithosphere (Gutscher *et al.*, 2002; Duggen *et al.*, 2004). Hydrous fluids and melts were released from the subducted oceanic lithosphere into the mantle wedge beneath the Alboran Basin, which consisted of asthenospheric mantle and attenuated continental lithosphere. These hydrous fluids–melts caused high degrees of partial melting in the mantle wedge, resulting in the eruption of low-K (tholeiitic) and medium-K (calc-alkaline) series lavas in Alboran Basin area. These Middle to Late Miocene lavas have typical subduction-related geochemical signatures similar to those from modern subduction zones (e.g. Izu–Bonin arc) (Hoernle *et al.*, 1999; Duggen *et al.*, 2004; Gill *et al.*, 2004). Roll-back and steepening of the subducted Tethys oceanic lithosphere could have had several effects, as follows.

(1) It could cause peeling off (delamination) of bands of subcontinental mantle lithosphere beneath the southern Iberian and northwestern African continental margins (continental-edge delamination). We propose that the lithospheric bands were attached to the cold and dense subducting oceanic lithosphere through mechanical coupling, which would be an effective mechanism for the removal of even buoyant subcontinental lithosphere.

(2) It could cause asthenosphere contaminated with plume material to well up from depth around the margins of the delaminating subcontinental lithosphere.

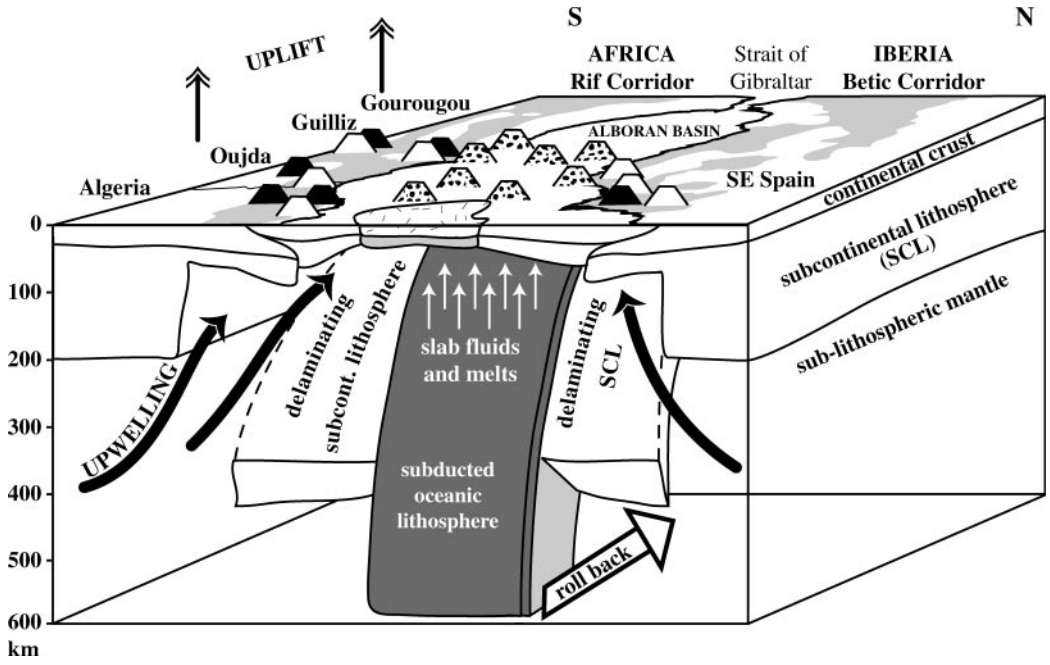

Fig. 13. Three-dimensional, geodynamic model of the westernmost Mediterranean at the Miocene–Pliocene boundary based on new and published geochronological and geochemical data for the westernmost Mediterranean post-collisional magmatism combined with published geophysical and geological observations (see main text for details). *Alboran Basin area*: east-dipping subduction of Tethyan oceanic lithosphere beneath the Alboran Basin released fluids and melts from the subducting oceanic plate causing high degrees of partial melting of the overlying mantle wedge. The subduction process led to the generation of Middle to Upper Miocene low-K (tholeiitic) and medium-K (calc-alkaline) series volcanic rocks with geochemical characteristics similar to those found in active subduction zones (Hoernle *et al.*, 1999; Duggen *et al.*, 2004; Gill *et al.*, 2004). The attenuated continental crust in the Alboran Basin area is the remnant of the Alboran block that collided with the southern Iberian and northwestern African continental margins in the Early Miocene (Gutscher *et al.*, 2002; Duggen *et al.*, 2004). *Southern Iberian and northern African plate margins*: westward slab roll-back of the subducted oceanic lithosphere triggered (1) delamination of bands of subcontinental lithosphere (continental-edge delamination) and (2) upwelling of plume-contaminated sub-lithospheric mantle around the edges of the delaminating lithosphere and beneath the southern Iberian and northwestern African continental margins. Si–K-rich magmatism with a subduction-like geochemical signature resulted from low-degree partial melting of metasomatically enriched subcontinental lithosphere. Si-poor, intraplate-type magmas were generated by low-degree decompressional partial melting of the upwelling sub-lithospheric mantle contaminated with plume components. Continental-edge delamination combined with sub-lithospheric mantle upwelling resulted in the uplift and closure of marine gateways connecting the Atlantic Ocean with the Mediterranean Sea (Betic and Rif Corridors) in the Late Miocene, which ultimately led to the isolation and desiccation of the Mediterranean Sea in the Messinian (Duggen *et al.*, 2003).

Perturbation of the metasomatically enriched subcontinental lithosphere resulted in the generation of Si–K-rich, subduction-type melts in the Late Miocene to Early Pliocene. Decompressional partial melting of the upwelling asthenosphere contaminated with plume material led to the formation of Si-poor, intraplate-type alkali basalts in the Late Miocene to Pleistocene. Interaction of Si-poor melts with the metasomatized subcontinental mantle or Si–K-rich melts derived from it could have generated magmas with hybrid geochemical characteristics between subduction- and intraplate-type. Westward slab roll-back and steepening coupled with delamination of subcontinental lithospheric mantle is consistent with the earlier onset of the subduction- to intraplate-type magmatic transition in Algeria (10·0 to 7·5 Ma) (Louni-Hacini *et al.*, 1995; Coulon *et al.*, 2002) than in southeastern Iberia (6·4 to 2·9 Ma) and northern Morocco (6·8 to 4·8 Ma) (El Bakkali *et al.*, 1998). Thermomechanical modelling shows that the delamination of bands of subcontinental lithosphere could also have caused large-scale uplift of the order of 1 km (continental-edge effect) sufficient to close the Late Miocene marine gateways at the southern Iberian and northwestern African continental margins, causing the Mediterranean to dry up in the Messinian (Duggen *et al.*, 2003).

CONCLUSIONS

The transition from subduction-related, Si–K-rich to intraplate-type, Si-poor magmatism in the westernmost Mediterranean at the Miocene–Pliocene boundary can be observed both on a regional scale in the entire Alboran region and on a local scale in individual volcanic centres. Whereas the Alboran Basin area is marked by the eruption of low-K (tholeiitic) series and medium- to high-K calc-alkaline series volcanic rocks related to Middle to Late Miocene subduction (Duggen *et al.*, 2004), the southern Iberian and northwestern African continental

margins are characterized by Upper Miocene to Lower Pliocene Si–K-rich, subduction-type and Upper Miocene to Pleistocene Si-poor, intraplate-type magmatism.

The mafic Si–K-rich group magmas at the Iberian and African continental margins resulted from low degrees of partial melting of subcontinental mantle lithosphere metasomatically enriched by fluids or melts from earlier subduction processes. Mafic intraplate-type, Si-poor magmas were generated by low-degree decompressional melting of upwelling asthenospheric mantle contaminated with enriched plume material. The hybrid geochemical characteristics of the mafic magmas generated close to the Miocene–Pliocene boundary reflect interaction between subduction-type, Si–K-rich magmas or their source regions and intraplate-type, Si-poor magmas of sub-lithospheric origin.

At the Miocene–Pliocene boundary, the primary source of the magmatism shifted from subduction-modified subcontinental lithosphere to plume-contaminated sub-lithospheric sources not previously affected by subduction processes. The evolution of the Gourougou stratovolcanic complex in Morocco exhibits the progressively decreasing influence of the subduction-type component and increase of the intraplate-type component through time.

The transition from subduction-related to intraplate-type magmatism points to major changes in the geometry of the westernmost Mediterranean mantle. Roll-back and steepening of an east-dipping, subducting slab of old Tethys oceanic lithosphere in the Miocene triggered (1) the peeling off (delamination) of bands of the subcontinental lithosphere at the southern Iberian and northwestern African continental margins and (2) the upwelling of plume-contaminated sub-lithospheric material beneath southern Iberia and northwestern Africa, replacing the delaminating subcontinental lithospheric mantle. Continental-edge delamination associated with slab roll-back and steepening provides a plausible explanation for the complex spatial and temporal geochemical evolution of magmatism in the westernmost Mediterranean since the Oligocene, and is consistent with the Late Miocene uplift and closure of marine gateways connecting the Mediterranean Sea to the Atlantic Ocean, causing the desiccation of the Mediterranean and the Messinian Salinity Crisis.

Wider implications are that subcontinental lithosphere can effectively be delaminated when attached to dense subducting oceanic lithosphere. This process may be responsible for continental uplift and the generation of post-collisional magmatism in the Mediterranean area and elsewhere in the world.

ACKNOWLEDGEMENTS

We express our gratitude to K. Abdelmalki, M. Bouabdellah, Y. Bouabdellah, M. Chaieb, M. Jadid, A. Milhi and A. Moukadiri (from the Universities of Oujda and Fez and the Centre Régional Géologique d'Oujda) for their valuable help with our fieldwork in Morocco. We thank T. Arpe, D. Garbe-Schönberg, F. Hauff, L. Hoffmann, S. Krolikowska, S. Laukat, S. Plagmann, D. Rau, J. Sticklus, S. Vetter, K. Wolff and E. Zuleger for their help with the analytical work in Kiel. Martin Menzies and Matthew Thirlwall are gratefully acknowledged for comments on the manuscript prior to submission. We are grateful to José-Maria Cebriá, Szabolcs Harangi, Julian Pearce and Marjorie Wilson for their thorough reviews and valuable comments on the manuscript. The project was supported by the Deutsche Forschungsgemeinschaft (German Research Council) (HO1833/5).

SUPPLEMENTARY DATA

Supplementary data for this paper are available on *Journal of Petrology* online.

REFERENCES

Ait-Brahim, L. & Chotin, P. (1990). Oriental Moroccan Neogene volcanism and strike-slip faulting. *Journal of African Earth Sciences* **11**, 273–280.

Allègre, C.-J., Dupre, B., Lambret, B. & Richard, P. (1981). The subcontinental vs suboceanic debate; I, Lead–neodymium–strontium isotopes in primary alkali basalts from a shield area; the Ahaggar volcanic suite. *Earth and Planetary Science Letters* **52**, 85–92.

Andries, D. & Bellon, H. (1989). Ages isotopiques ^{40}K–^{40}Ar du volcanisme alcalin néogène d'Oujda (Maroc oriental) et implications tectoniques. *Sciences Géologiques, Mémoire* **84**, 107–116.

Arculus, R. J. & Gust, D. A. (1995). Regional petrology of the San Francisco Volcanic Field, Arizona, USA. *Journal of Petrology* **36**, 827–861.

Bellon, H. & Brousse, R. (1977). Le magmatisme périméditerranén occidental. Essai de synthèse. *Bulletin de la Société Géologique de France* **7**, 469–480.

Bellon, H. & Letouzey, J. (1977). Volcanism related to plate-tectonics in the western and eastern Mediterranean. In: Biju-Duval, B. & Montadert, L. (eds) *Structural History of the Mediterranean Basins*. Paris: Technip, pp. 165–184.

Bellon, H., Bordet, P. & Montenat, C. (1983). Chronologie du magmatisme néogène des Cordillères bètiques (Espagne méridionale). *Bulletin de la Société Géologique de France* **7**, 205–217.

Benito, R., López-Ruiz, J., Cebriá, J. M., Hertogen, J., Doblas, M., Oyarzun, R. & Demaiffe, D. (1999). Sr and O isotope constraints on source and crustal contamination in the high-K calc-alkaline and shoshonitic Neogene volcanic rocks of SE Spain. *Lithos* **46**, 733–802.

Bird, P. (1979). Continental delamination and the Colorado plateau. *Journal of Geophysical Research* **84**, 7561–7571.

Blanco, M. J. & Spakman, W. (1993). The P-wave velocity structure of the mantle below the Iberian Peninsula: evidence for subducted lithosphere below southern Spain. *Tectonophysics* **221**, 13–34.

Calvert, A., Sanvol, E., Seber, D., Barazangi, M., Roecker, S., Mourabit, T., Vidal, F., Alguacil, G. & Jabour, N. (2000). Geodynamic evolution of the lithosphere and upper mantle beneath the Alboran region of the western Mediterranean: constraints from travel time tomography. *Journal of Geophysical Research* **105**, 10871–10898.

Capedri, S., Venturelli, G., Salvioli-Mariani, E., Crawford, A. J. & Barbieri, M. (1989). Upper-mantle xenoliths and megacrysts in an alkali basalt from Tallante, south-eastern Spain. *European Journal of Mineralogy* **1**, 685–699.

Carminati, E., Wortel, M. J. R., Spakman, W. & Sabadini, R. (1998). The role of slab detachment processes in the opening of the western–central Mediterranean basins: some geological and geophysical evidence. *Earth and Planetary Science Letters* **160**, 651–665.

Cebriá, J.-M. & López-Ruiz, J. (1995). Alkali basalts and leucitites in an extensional intracontinental plate setting: the late Cenozoic Calatrava Volcanic Province (central Spain). *Lithos* **35**, 27–46.

Cesare, B. & Maineri, C. (1999). Fluid-present anatexis of metapelites at El Joyazo (SE Spain): constraints from Raman spectroscopy of graphite. *Contributions to Mineralogy and Petrology* **135**, 41–52.

Cesare, B., Salvioli Mariani, E. & Venturelli, G. (1997). Crustal anatexis and melt extraction during deformation in the restitic xenoliths at El Joyazo (SE Spain). *Mineralogical Magazine* **61**, 15–27.

Chaffey, D. J., Cliff, R. A. & Wilson, B. M. (1989). Characterization of the St Helena magma source. In: Saunders, A. D. & Norry, M. J. (eds) *Magmatism in the Ocean Basins. Geological Society, London, Publications* **42**, 257–276.

Comas, M. C., Platt, J. P., Soto, J. I. & Watts, A. B. (1999). The origin and tectonic history of the Alboran Basin: insights from Leg 161 results. In: Zahn, R., Comas, M. C. & Klaus, A. (eds) *Proceedings of the Ocean Drilling Program, Scientific Results, 161*. College Station, TX: Ocean Drilling Program, pp. 555–580.

Coppier, G., Griveaud, P., de Larouziere, F. D., Montenat, C. & d'Estevou, O. (1989). Example of Neogene tectonic indentation in the Eastern Betic Cordilleras: the Arc of Aguilas (Southeastern Spain). *Geodinamica Acta* **3**, 37–51.

Coulon, C., Megartsi, M., Fourcade, S., Maury, R. C., Bellon, H., Louni-Hacini, A., Cotten, J., Coutelle, A. & Hermitte, D. (2002). Post-collisional transition from calc-alkaline to alkaline volcanism during the Neogene in Oranie (Algeria): magmatic expression of a slab breakoff. *Lithos* **62**, 87–110.

Dalrymple, G. B. & Duffield, W. A. (1988). High precision $^{40}Ar/^{39}Ar$ dating of Oligocene tephra from the Mogollon–Datil volcanic field using a continuous laser system. *Geophysical Research Letters* **15**, 463–466.

Davies, J. H. & Blanckenburg, F. v. (1995). Slab breakoff: a model of lithosphere detachment and its test in the magmatism and deformation of collisional orogens. *Earth and Planetary Science Letters* **129**, 85–102.

Deer, W. A., Howie, R. A. & Zussman, J. (1996). *An Introduction to the Rock-forming Minerals*. Harlow: Addison Wesley Longman, 549 pp.

Dewey, J. F., Helman, M. L., Hutton, D. H. W. & Knott, S. D. (1989). Kinematics of the western Mediterranean. In: Coward, M. P. & Park, R. G. (eds) *Alpine Tectonics. Geological Society, London, Special Publications* **45**, 265–283.

Docherty, C. & Banda, E. (1995). Evidence for the eastward migration of the Alboran Sea based on regional subsidence analysis: a case for basin formation by delamination of the subcrustal lithosphere? *Tectonics* **14**, 804–818.

Dosso, L., Hanan, B. B., Bougault, H., Schilling, J. G. & Joron, J. L. (1991). Sr–Nd–Pb geochemical morphology between 10 degrees and 17 degrees N on the Mid-Atlantic Ridge: a new MORB isotope signature. *Earth and Planetary Science Letters* **106**, 29–43.

Duffield, W. A. & Dalrymple, G. B. (1990). The Taylor Creek Rhyolite of New Mexico: a rapidly emplaced field of lava domes and flows. *Bulletin of Volcanology* **52**, 475–487.

Duggen, S. (2002). Spatial and temporal geochemical evolution of igneous rocks in the Alborán Region (westernmost Mediterreanean): implications for the origin of Mediterranean-style back-arc basins and the Messinian Salinity Crisis. Ph.D. thesis, University of Kiel.

Duggen, S., Hoernle, K., van den Bogaard, P., Rüpke, L. & Phipps Morgan, J. (2003). Deep roots of the Messinian salinity crisis. *Nature* **422**, 602–606.

Duggen, S., Hoernle, K., van den Bogaard, P. & Harris, C. (2004). Magmatic evolution of the Alboran Region: the role of subduction in forming the western Mediterranean and causing the Messinian Salinity Crisis. *Earth and Planetary Science Letters* **218**, 91–108.

Dupuy, C., Dostal, J. & Boivin, P. A. (1986). Geochemistry of ultramafic xenoliths and their host alkali basalts from Tallante, southern Spain. *Mineralogical Magazine* **50**, 231–239.

Ellam, R. M., Menzies, M. A., Hawkesworth, C. J., Leeman, W. P., Rosi, M. & Serri, G. (1988). The transition from calc-alkaline to potassic orogenic magmatism in the Aeolian Islands, Southern Italy. *Bulletin of Volcanology* **50**, 386–398.

Ellam, R. M., Hawkesworth, C. J., Menzies, M. A. & Rogers, N. W. (1989). The volcanism of Southern Italy: role of subduction and the relationship between potassic and sodic alkaline magmatism. *Journal of Geophysical Research* **94**, 4589–4601.

El Bakkali, S., Gourgaud, A., Bourdier, J.-L., Bellon, H. & Gundogdu, N. (1998). Post-collision Neogene volcanism of the Eastern Rif (Morocco): magmatic evolution through time. *Lithos* **45**, 523–543.

Esteban, M., Braga, J. C., Martín, J. & de Santisteban, C. (1996). Western Mediterranean Reef Complexes. In: Franseen, E. K., Esteban, M., Ward, W. C. & Rouchy, J.-M. (eds) *Models for Carbonate Stratigraphy. From Miocene Reef Complexes of Mediterranean Regions*. Tulsa, OK: SEPM (Society for Sedimentary Geology), pp. 55–72.

Foley, S. (1992). Vein-plus-wall-rock melting mechanisms in the lithosphere and the origin of potassic alkaline magmas. *Lithos* **28**, 435–453.

Foley, S. F. (1993). An experimental study of olivine lamproite: first results from the diamond stability field. *Geochimica et Cosmochimica Acta* **57**, 483–489.

Garbe-Schönberg, C. D. (1993). Simultaneous determination of thirty-seven trace elements in twenty-eight international rock standards by ICP-MS. *Geostandards Newsletter* **17**, 81–97.

Geldmacher, J. & Hoernle, K. (2000). The 72 Ma geochemical evolution of the Madeira hotspot (eastern North Atlantic): recycling of Paleozoic (≤500 Ma) oceanic lithosphere. *Earth and Planetary Science Letters* **183**, 73–92.

Geldmacher, J., van den Bogaard, P., Hoernle, K. & Schmincke, H.-U. (2000). The $^{40}Ar/^{39}Ar$ age dating of the Madeira Archipelago and hotspot track (eastern North Atlantic). *Geochemistry, Geophysics, Geosystems* **1**, paper number 1999GC000018.

Gill, R. C. O., El Aparicio, A., El Azzouzi, M., Hernandez, J., Thirlwall, M. F., Bourgois, J. & Marriner, G. F. (2004). Depleted arc volcanism in the Alboran Sea and shoshonitic volcanism in Morocco: geochemical and isotopic constraints on Neogene tectonic processes. *Lithos* **78**, 363–388.

Gîrbacea, R. & Frisch, W. (1998). Slab in the wrong place: lower lithospheric mantle delamination in the last stage of the Eastern Carpathian subduction retreat. *Geology* **26**, 611–614.

Goes, S., Spakman, W. & Bijward, H. (1999). A lower mantle source for Central European volcanism. *Science* **286**, 1928–1931.

Granet, M., Wilson, M. & Achauer, U. (1995). Imaging a mantle plume beneath the French Massif Central. *Earth and Planetary Science Letters* **136**, 281–296.

Green, D. H. (1973). Experimental melting studies on a model upper mantle composition at high pressure under water-saturated and water-undersaturated conditions. *Earth and Planetary Science Letters* **19**, 37–53.

Gutscher, M.-A., Malod, J., Rehault, J.-P., Contrucci, I., Klingelhoefer, F., Mendes-Victor, L. & Spakman, W. (2002). Evidence for active subduction beneath Gibraltar. *Geology* **30**, 1071–1074.

Gutscher, M.-A., Malod, J., Raehault, J.-P., Construcci, I., Klinelhoefer, F., Mendes-Victor, L. & Spakman, W. (2003). Evidence for active subduction beneath Gibraltar: Reply. *Geology: Online Forum*, e23.

Harmand, C. & Cantagrel, J. M. (1984). Le volcanisme alcalin tertiaire et quaternaire du Moyen Atlas (Maroc): chronologie K/Ar et cadre géodynamique. *Journal of African Earth Sciences* **2**, 51–55.

Hart, S. R. (1984). A large-scale isotope anomaly in the Southern Hemisphere mantle. *Nature* **309**, 753–757.

Hawkesworth, C. J., Gallagher, K., Hergt, J. M. & McDermott, F. (1993). Mantle and slab contributions in arc magmas. *Annual Review of Earth and Planetary Sciences* **21**, 175–204.

Hernandez, J. (1986). Pétrologie du massif volcanique du Guilliz (Maroc oriental). Cristallisation fractionée, mélanges de magmas et transferts de fluides dans une série shoshonitique. *Journal of African Earth Sciences* **5**, 381–399.

Hernandez, J. & Bellon, H. (1985). Chronologie K–Ar du volcanisme miocéne du Rif oriental (Maroc): implications tectoniques et magmatique. *Revue de Géologie et de Géographie Physique* **26**, 85–94.

Hirose, K. & Kushiro, I. (1993). Partial melting of dry peridotites at high pressures: determination of compositions of melts segregated from peridotite using aggregates of diamond. *Earth and Planetary Science Letters* **114**, 477–489.

Hoernle, K. (1998). Geochemistry of Jurassic oceanic crust beneath Gran Canaria (Canary): implications for crustal recycling and assimilation. *Journal of Petrology* **39**, 859–880.

Hoernle, K. & Schmincke, H. U. (1993*a*). The petrology of the tholeiites through melilite nephelinites on Gran Canaria, Canary Islands: crystal fractionation, accumulation, and depths of melting. *Journal of Petrology* **34**, 573–597.

Hoernle, K. & Schmincke, H. U. (1993*b*). The role of partial melting in the 15-Ma geochemical evolution of Gran Canaria: a blob model for the Canary hotspot. *Journal of Petrology* **34**, 599–626.

Hoernle, K. A. & Tilton, G. R. (1991). Sr–Nd–Pb isotope data for Fuerteventura (Canary Islands) basal complex and subaerial volcanics: applications to magma genesis and evolution. *Schweizerische Mineralogische und Petrographische Mitteilungen* **71**, 3–18.

Hoernle, K., Tilton, G. & Schmincke, H. U. (1991). Sr–Nd–Pb isotopic evolution of Gran Canaria: evidence for shallow enriched mantle beneath the Canary Islands. *Earth and Planetary Science Letters* **106**, 44–63.

Hoernle, K., Zhang, Y. S. & Graham, D. (1995). Seismic and geochemical evidence for large-scale mantle upwelling beneath the eastern Atlantic and western central Europe. *Nature* **374**, 34–39.

Hoernle, K., van den Bogaard, P., Duggen, S., Mocek, B. & Garbe-Schönberg, D. (1999). Evidence for Miocene subduction beneath the Alboran Sea: $^{40}Ar/^{39}Ar$ dating and geochemistry of volcanic rocks from Holes 977A and 978A. In: Zahn, R., Comas, M. C. & Klaus, A. (eds) *Proceedings of the Ocean Drilling Program, Scientific Results, 161*. College Station, TX: Ocean Drilling Program, pp. 357–373.

Hoernle, K., Duggen, S., Geldmacher, J., Klügel, A., *et al.* (2003). *METEOR Cruise No. 51, Leg 1, Vulkosa: Vulkanismus Ostatlantik–Alboran in Meteor Berichte 03-1 Ostatlantik–Mittelmeer–Schwarzes Meer, Cruise No. 51, 12 September to 28 December 2001*. Kiel: GEOMAR Research Centre.

Hofmann, A. W. (1988). Chemical differentiation of the Earth. The relationship between mantle, continental crust, and oceanic crust. *Earth and Planetary Science Letters* **90**, 297–314.

Hofmann, A. W. (1997). Mantle geochemistry: the message from oceanic volcanism. *Nature* **385**, 219–229.

Horvath, F. & Berckhemer, H. (1982). Mediterranean backarc basins. In: Berckhemer, H. & Hsü, K. (eds) *Alpine–Mediterranean Geodynamics*. Washington, DC: American Geophysical Union; Boulder, CO: Geological Society of America, pp. 141–173.

Houseman, G. (1996). From mountains to basins. *Nature* **379**, 771–772.

Hsü, K. J., Ryan, W. B. F. & Cita, M. B. (1973). Late Miocene desiccation of the Mediterranean. *Nature* **242**, 240–244.

Innocenti, F., Mazzuoli, R., Pasquare, G., Radicati di Brozolo, F. & Villari, L. (1982). Tertiary and Quaternary volcanism of the Erzurum–Kars area (Eastern Turkey): geochronological data and geodynamic evolution. *Journal of Volcanology and Geothermal Research* **13**, 223–240.

Ito, E., White, W. M. & Gopel, C. (1987). The O, Sr, Nd and Pb isotope geochemistry of MORB. *Chemical Geology* **62**, 157–176.

Jadid, M., Wernli, R. & Rezqi, H. (1999). Biostratigraphie et paléogéographie du Mio-Pliocène de la region d'Oujda (Maroc nord-oriental). *Revue de Paléobiologie, Genève* **18**, 253–258.

Jolivet, L. & Faccenna, C. (2000). Mediterranean extension and the African–Eurasia collision. *Tectonics* **19**, 1095–1106.

Kay, R. W. & Mahlburg Kay, S. (1993). Delamination and delamination magmatism. *Tectonophysics* **219**, 177–189.

Keller, J. (1982). Mediterranean island arcs. In: Thorpe, R. S. (ed.) *Andesites: Orogenic Andesites and Related Rocks*. Chichester: John Wiley, pp. 307–325.

Krijgsman, W., Hilgen, F. J., Raffi, I., Sierro, F. J. & Wilson, D. S. (1999). Chronology, causes and progression of the Messinian salinity crisis. *Nature* **400**, 652–655.

Lonergan, L. & White, N. (1997). Origin of the Betic–Rif mountain belt. *Tectonics* **16**, 504–522.

López Ruiz, J. & Rodríguez Badiola, E. (1980). La region volcanica neogena del sureste de España. *Estudios Geologicos* **36**, 5–63.

López-Ruiz, J., Cebria, J. M. & Doblas, M. (2002). Cenozoic magmatism I: The Iberian peninsula. In: Gibbons, W. & Moreno, M. T. (eds) *The Geology of Spain*. London: Geological Society, pp. 417–438.

Louni-Hacini, A., Bellon, H., Maury, R. C., Megartsi, M., Coulon, C., Semroud, B., Cotten, J. & Coutelle, A. (1995). Datation 40K–40Ar de la transition du volcanisme calco-alcalin au volcanisme alcalin en Oranie au Miocène supérieur. *Comptes Rendus de l'Académie des Sciences* **321**, 975–982.

Montenat, C. & Ott d'Estevou, P. (1995). Late Neogene basins evolving in the Eastern Betic transcurrent fault zone: an illustrated review. In: Friend, P. F. & Dabrio, C. J. (eds) *Tertiary Basins of Spain*. Cambridge: Cambridge University Press, pp. 372–386.

Munksgaard, N. C. (1984). High $\delta^{18}O$ and possible pre-eruptional Rb–Sr isochrons in cordierite-bearing Neogene volcanics from SE Spain. *Contributions to Mineralogy and Petrology* **87**, 351–358.

Nelson, D. R. (1992). Isotopic characteristics of potassic rocks: evidence for the involvement of subducted sediments in magma genesis. *Lithos* **28**, 403–420.

Nelson, D. R., McCulloch, M. T. & Sun, S. S. (1986). The origins of ultrapotassic rocks as inferred from Sr, Nd and Pb isotopes. *Geochimica et Cosmochimica Acta* **50**, 231–245.

Nobel, F. A., Andriessen, P. A. M., Hebeda, E. H., Priem, H. N. A. & Rondeel, H. E. (1981). Isotopic dating of the post-alpine Neogene volcanism in the Betic Cordilleras, Southern Spain. *Geologie en Mijnbouw* **60**, 209–214.

Pearce, J. A. & Peate, D. W. (1995). Tectonic implications of the composition of volcanic arc magmas. *Annual Review of Earth and Planetary Sciences* **23**, 251–285.

Pearce, J. A., Bender, J. F., De Long, S. E., Kidd, W. S. F., Low, P. J., Güner, Y., Saroglu, F., Yilmaz, Y., Moorbath, S. & Mitchell, J. G. (1990). Genesis of collision volcanism in Eastern Anatolia, Turkey. *Journal of Volcanology and Geothermal Research* **44**, 189–229.

Platt, J. P. & England, P. C. (1993). Convective removal of lithosphere beneath mountain belts: thermal and mechanical consequences. *American Journal of Science* **293**, 307–336.

Platt, J. P. & Vissers, R. L. M. (1989). Extensional collapse of thickened continental lithosphere: a working hypothesis for the Alboran Sea and Gibraltar Arc. *Geology* **17**, 540–543.

Platt, J. P., Whitehouse, M. J., Kelley, S. P., Carter, A. & Hollick, L. (2003). Simultaneous extensional exhumation across the Alboran Basin: implications for the causes of late orogenic extension. *Geology* **31**, 251–254.

Rickwood, P. C. (1989). Boundary lines within petrological diagrams which use oxides of major and minor elements. *Lithos* **22**, 247–263.

Roger, S., Münch, P., Cornee, J. J., Saint Martin, J. P., Feraud, G., Pestrea, S., Conesa, G. & Ben Moussa, A. (2000). $^{40}Ar/^{39}Ar$ dating of the pre-evaporitic Messinian marine sequences of the Melilla basin (Morocco): a proposal for some biosedimentary events as isochrons around the Alboran Sea. *Earth and Planetary Science Letters* **179**, 101–113.

Royden, L. H. (1993). Evolution of retreating subduction boundaries formed during continental collision. *Tectonics* **12**, 629–638.

Saadi, M., Hilali, E. A., Bensaid, M., Boudda, A. & Dahmani, M. (1985). Carte géologique du Maroc. Paris: Ministère de l'énergie et des mines, direction de la géologie.

Seber, D., Barazangi, M., Ibenbrahim, A. & Demnati, A. (1996*a*). Geophysical evidence for lithospheric delamination beneath the Alboran Sea and Rif–Betic mountains. *Nature* **379**, 785–790.

Seber, D., Barazangi, M., Tadili, B. A., Ramdani, M., Ibenbrahim, A. & Sari, D. B. (1996*b*). Three-dimensional upper mantle structure beneath the intraplate Atlas and interplate Rif mountains of Morocco. *Journal of Geophysical Research* **101**, 3125–3138.

Serri, G., Innocenti, F. & Manetti, P. (1993). Geochemical and petrological evidence of the subduction of delaminated Adriatic continental lithosphere in the genesis of the Neogene–Quaternary magmatism of central Italy. *Tectonophysics* **223**, 117–147.

Sun, S.-s. & McDonough, W. F. (1989). Chemical and isotopic systematics of oceanic basalts: implications for mantle composition and processes. In: Saunders, A. D. & Norry, M. J. (eds) *Magmatism in the Ocean Basins. Geological Society, London, Special Publications* **42**, 313–345.

Taylor, R. N. & Nesbitt, R. W. (1998). Isotopic characteristics of subduction fluids in an intra-oceanic setting, Izu–Bonin Arc, Japan. *Earth and Planetary Science Letters* **164**, 79–98.

Taylor, S. R. & McLennan, S. M. (1985). *The Continental Crust: its Composition and Evolution*. Oxford: Blackwell Scientific, 312 pp.

Thirlwall, M. F. (1997). Pb isotopic and elemental evidence for OIB derivation from young HIMU mantle. *Chemical Geology* **139**, 51–74.

Tisserant, D., Laouina, A. & Clauer, N. (1985). Datation K–Ar des basaltes de la plaine des Angad au sud d'Oujda (Maroc-oriental). *Bulletin de la Société Géologique de France* **38**, 141–145.

Toscani, L., Contini, S. & Ferrarini, M. (1995). Lamproitic rocks from Cabezo Negro de Zeneta: brown micas as a record of magma mixing. *Mineralogy and Petrology* **55**, 281–292.

Turner, S., Hawkesworth, C., Liu, J., Rogers, N., Kelley, S. & van Calsteren, P. (1993). Timing of Tibetan uplift constrained by analysis of volcanic rocks. *Nature* **364**, 50–54.

Turner, S., Arnaud, N., Liu, J., Rogers, N., Hawkesworth, C., Harris, N., Kelley, S., van Calsteren, P. & Deng, W. (1996). Post-collision, shoshonitic volcanism on the Tibetan Plateau: implications for convective thinning of the lithosphere and the source of ocean island basalts. *Journal of Petrology* **37**, 45–71.

Turner, S. P., Platt, J. P., George, R. M. M., Kelley, S. P., Pearson, D. G. & Nowell, G. M. (1999). Magmatism associated with orogenic collapse of the Betic–Alboran Domain, SE Spain. *Journal of Petrology* **40**, 1011–1036.

Van den Bogaard, P. (1995). 40Ar/39Ar ages of sanidine phenocrysts from Laacher See tephra (12,900 yr BP): chronostratigraphic and petrological significance. *Earth and Planetary Science Letters* **133**, 163–174.

Venturelli, G., Capedri, S., Di Battistini, G., Crawford, A., Kogarko, L. N. & Celestini, S. (1984). The ultrapotassic rocks from southeastern Spain. *Lithos* **17**, 37–54.

Venturelli, G., Salvioli-Mariani, E., Foley, S. F., Capedri, S. & Crawford, A. J. (1988). Petrogenesis and conditions of crystallization of Spanish lamproitic rocks. *Canadian Mineralogist* **26**, 67–79.

Vielzeuf, D. (1983). The spinel and quartz associations in high grade xenoliths from Tallante (S.E. Spain) an their potential use in geothrmometry and barometry. *Contributions to Mineralogy and Petrology* **82**, 301–311.

Weijermars, R. (1985). Uplift and subsidence history of the Alboran Basin and a profile of the Alboran diapir (W-Mediterranean). *Geologie en Mijnbouw* **64**, 349–356.

Wilson, M. & Bianchini, G. (1999). Tertiary–Quaternary magmatism within the Mediterranean and surrounding regions. In: Durand, B., Jolivet, L., Horváth, F. & Sérrane, M. (eds) *The Mediterranean Basins: Tertiary Extension within the Alpine Orogen. Geological Society, London, Special Publications* **156**, 141–168.

Wilson, M. & Downes, H. (1991). Tertiary–Quaternary extension-related alkaline magmatism in Western and Central Europe. *Journal of Petrology* **32**, 811–849.

Wortel, M. J. R. & Spakman, W. (2000). Subduction and slab detachment in the Mediterranean–Carpathian region. *Science* **290**, 1910–1917.

Wyllie, P. J. & Wolf, M. B. (1993). Amphibolite dehydration-melting: sorting out the solidus. In: Alabaster, P. H. M., Harris, N. B. W. & Neary, C. R. (eds) *Magmatic Processes and Plate Tectonics. Geological Society, London, Special Publications* **76**, 405–416.

Zeck, H. P. (1970). An erupted migmatite from Cerro del Hoyazo, SE Spain. *Contributions to Mineralogy and Petrology* **26**, 225–246.

Zeck, H. P. (1996). Betic–Rif orogeny: subduction of Mesozoic Tethys lithosphere under eastward drifting Iberia, slab detachment shortly before 22 Ma, and subsequent uplift and extensional tectonics. *Tectonophysics* **254**, 1–16.

Zeck, H. P. (1999). Alpine plate kinematics in the western Mediterranean: a westward-directed subduction regime followed by slab roll-back and slab detachment. In: Durand, B., Jolivet, L., Horváth, F. & Sérrane, M. (eds) *The Mediterranean Basins: Tertiary Extension within the Alpine Orogen. Geological Society, London, Special Publications* **156**, 109–120.

Zeck, H. P., Kristensen, A. B. & Williams, I. S. (1998). Post-collisional volcanism in a sinking slab setting—crustal anatectic origin of pyroxene-andesite magma, Caldear volcanic province, southeastern Spain. *Lithos* **45**, 499–522.

Zeck, H. P., Kristensen, A. B. & Nakamura, E. (1999). Inherited Palaeozoic and Mesozoic Rb–Sr isotopic signatures in Neogene calc-alkaline volcanics, Alboran Volcanic Province, SE Spain. *Journal of Petrology* **40**, 511–524.

Zindler, A. & Hart, S. (1986). Chemical geodynamics. *Annual Review of Earth and Planetary Sciences* **14**, 493–571.